MASTER THESIS

Analysis of the Arctic humidity and cloud evolution based on homogenized radiosonde and radiation data obtained at Ny-Ålesund

Analyse der arktischen Feuchte- und Wolkenentwicklung anhand homogenisierter Radiosonden- und Strahlungsdaten am Beispiel Ny-Ålesunds

UNIVERSITÄT POSTDAM
Mathematisch-Naturwissenschaftlich Fakultät
Department of Physics

ALFRED-WEGENER-INSTITUT
Helmholtz-Zentrum für Polar- und Meeresforschung
Department of Atmospheric Circulation

BY MARKUS KAYSER
September 2014 – alpha

Supervisor: Dr. Christoph Ritter

1st **corrector:** Prof. Dr. Klaus Dethloff

2nd **corrector:** Prof. Dr. Norbert Seehafer

ABSTRACT

Since 1991, the Alfred Wegener Institute continuously monitors the Arctic climate at Ny-Ålesund, Svalbard. Over the period of more than twenty years an increase in surface temperatures, especially during the winter months has been observed. During the same period the difference in incoming and outgoing long-wave radiation has increased by $3.9\,\mathrm{W\,m^{-2}}$ per decade. This thesis focuses on the question to what extend an increases in moisture content and in cloud cover has occurred alongside the temperature observations and to identify possible connections between them.

The analysis is based on data of the Baseline Surface Radiation Network (BSRN) measurement field and of daily radiosondes from 1991 to present. In a first step the humidity-profiles obtained by radiosondes are corrected applying empirical corrections in order to provide a homogeneous data set of water vapor and other humidity parameters over the entire measurement period. A climatology of the vertical distribution of water vapor above Ny-Ålesund is given, providing the basis to detect an increase in humidity over time. Additionally the vertical and temporal cloud distribution is investigated for the given period. The humidity profile data are further combined with surface radiation and meteorological measurements to infer the influence of water vapor content under clear sky conditions on the net long-wave radiation flux during winter.

The results show an increase in total column water vapor during the last two decades and indicate that the long-wave radiation flux is sensitive to small changes in water content. The observed increase in net long-wave radiation flux during winter can be attributed to the combined influence of the increase in water vapor content and in surface temperature.

CONTENTS

LIST OF FIGURES

LIST OF TABLES

ACRONYMS, SYMBOLS AND CONSTANTS

ACRONYMS

AWI   Alfred-Wegener-Institut

BSRN   Baseline Surface Radiation Network

IPCC   Intergovernmental Panel on Climate Change

OLR   Outgoing Long-wave Radiation

ISR   Incoming Short-wave Radiation

ILR   Incoming Long-wave Radiation

OSR   Outgoing Short-wave Radiation

TOA   Top Of Atmosphere

TOGA   Tropical Ocean and Global Atmosphere

COARE   Coupled Ocean-Atmoshere Response Experiment

CL   Cloud Lidar

GC   Ground Check

TD   Temperature dependence error

TL   Time-lag error

MC   Material contamination error

RB   Radiation dry bias

SN   Serial Number

LT   Launch Time

CBH   cloud base height

IWV   integrated water vapor

SYMBOLS AND CONSTANTS

T	–	temperature in K
t	–	temperature in °C
RH	–	relative humidity in % RH
AH	–	absolute humidity in $g\,m^{-3}$
ρ_w	–	density of water vapor, see AH
SH	–	specific humidity in $g\,kg^{-1}$
p	–	pressure in hPa
$L_\downarrow$	–	incoming long-wave radiation in $W\,m^{-2}$
$L_\uparrow$	–	outgoing long-wave radiation in $W\,m^{-2}$
F_{net}	–	net long-wave radiation flux in $W\,m^{-2}$
IWV	–	integrated water vapor in $kg\,m^{-2}$
e	–	partial vapor pressure hPa
E_s	–	saturation vapor pressure hPa
$P(A)$	–	probability that A occurs
ϵ_i	–	molecular binding energy of substance i
h	–	height above ground in m
U_i	–	individual RH profile
C_{rad}	–	radiation correction factor for RS90/92
C_T	–	TD correction factor
C_H	–	humidity dependent part of TD correction
$y(p)$	–	empirical correction function for RS90/92
RH_{water}	–	relative humidity above liquid water
RH_{ice}	–	relative humidity above ice
RH_{merged}	–	relative humidity above liquid water and ice merged at $-35\,°C$
$RH_{sat,water}/RH_{sat,ice}$	–	ratio defining the maximum humidity over water under ice saturation.
WD	–	wind direction in °
R	–	ideal deal gas constant, $8.31\,J\,mol^{-1}\,K^{-1}$
R_w	–	specific gas constant for water with $461\,J\,K^{-1}\,kg^{-1}$
M_w	–	molar mass of water $18.0153\,g\,mol^{-1}$
σ	–	Stefan-Boltzmann constant with $5.670\,373 \times 10^{-8}\,Wm^{-2}K^{-4}$
k	–	Boltzmann constant with $1.380\,648\,8 \times 10^{-23}\,J\,K^{-1}$
T_{2m}	–	2 m-temperature in K
T_s	–	surface temperature in K
T_a	–	ambient air temperature in K
u_∞^m	–	total amount of substance in an atmospheric column

INTRODUCTION

The cryosphere has become an emblem of climate change. The majority of people associates global warming with retreating glaciers, pictures of huge melt water lakes on top of the Greenland ice sheet and the constantly declining sea ice extent, which is often depicted as a polar bear standing on a lonely floe. All this is part of the phenomenon of Arctic Amplification, i. e. this region response much more sensitive to climate change. The latest IPCC report [Stocker u. a., 2013] offers a detailed description of the changes currently taking place in the cryosphere.

Recent analysis of temperature records for the period 1981–2012 show a warming of 0.60 °C per decade in contrast to 0.17 °C per decade globally [Hansen u. a., 2010]. One of the main contributors to this rapid increase is the ice-albedo feedback; sea ice and glacier retreat effectively reduce the albedo and enable the now open water and land surfaces to absorb larger portions of the incoming solar radiation during polar day. Therefore adding to the initial temperature increase and revealing this feedback to be strongly positives. Other phenomena act on polar climate as well. Some of the most important atmospheric feedbacks are briefly mentioned below:

water vapor feedback – is also referred to as clear sky water vapor feedback is a positive feedback describing the response of atmospheric water content due to a temperature perturbation. Its magnitude depends on the radiative properties of water vapor, the vertical distribution of vapor and the atmospheric temperature profile.

lapse rate feedback – is strongly coupled to the water vapor feedback. The outgoing long-wave radiation (OLR) at the top of the atmosphere (TOA) depends on the temperature and therefore on the rate of temperature decrease with height. Hence a steepening lapse rate due to warming in the higher troposphere would result in more effective cooling and a negative feedback. This is the case for the tropics. Regarding the Arctic this feedback contributes to warming of the lower parts of the atmosphere, thereby reducing the the OLR. In order to compensate this additional radiative forcing the surface temperatures has to increase. Thus this feedback is positive in polar regions.

cloud feedback – is difficult to estimate via climate models. Cloud cover and cloud vertical distribution is expected to change due to global warming. On the one hand clouds reduce the OLR, amplifying temperature trends. On the other hand they reflect large amounts of incoming short wave radiation back to space, preventing radiation uptake by the surface. Hence the net result can be both positive or negative. During polar night an increase in cloud fraction would result in a positive feedback.

Hence understanding the causes and effects of Arctic Amplification means investigation the contributions of individual feedbacks to the Arctic warming.
On the one hand research on feedback loops is challenging due to the interdependence of feedbacks. On the other studying feedback properties is challenging, especially in polar regions, where measurements are sparse. Climate models use reanalysis data, in order to make up for the low coverage of the area. They often use parameterizations resulting from studies conducted in the tropics or mid-latitudes, [Kondo und Matsushima, 1992]. But parameterizations intended for the tropics are not necessarily transferable to the Arctic. Improving them relies on continuous, long-term meteorological observations in the area of interest. Data records fulfilling this requirements are long-term data from stations like Barrow, Alaska, or Ny-Ålesund, Svalbard. Here the AWI records meteorological data continuously since 1991.

1.1   MEASUREMENTS BY AWI

Daily monitoring of atmospheric quantities is done at the AWIPEV research station in Ny-Ålesund since 1991. The most important measurements are briefly mentioned. The BSRN field (Baseline Surface Radiation Network) measures a variety of surface meteorological quantities, such as surface air temperature, wind speed and direction, humidity and pressure, as well as various radiation parameters such as incoming and outgoing shortwave and longwave surface radiation. A detailed description of the BSRN instruments can be found in [Kupfer u. a., 2006]. The meteorological field also includes a lidar based ceilometer which measures cloud base height (CBH) and thickness. Among the most important measurements of the vertical structure of the atmosphere is the daily 12UTC radiosonde launch. The radiosonde measures temperature and humidity of the ambient atmosphere reaching altitudes up to 30 km. It also measures pressure, wind speed and wind direction. Thus making the radiosondes an important instrument for monitoring the atmospheric structure. The soundings that have been conducted continuously since 1992 are the basis of this study.

1.2   CLIMATE OF NY-ÅLESUND FROM 1991 TO PRESENT

The AWIPEV station is located in Ny-rAlesund, Svalbard, one of the most northern settlements on this planet that is occupied throughout the year. The research village is located at 78°55′ North and 11°55′ East. This places the measurement site geographically at the boarder between sub-polar and high-polar zone. Looking at the seasonal temperature and humidity cycle in figure 1 determined from radiosonde data. The temperature and humidity displayed is taken from the lowest measurement bin of the soundings. One can see a strong seasonal cycle with maximum temperature of approximately 5.7 °C in July and minimum in February with −10.5 °C. The humidity record shows that the ground average relative humidity varies over a span of roughly 15 % RH with the minimum of 63.1 % RH in April and the maximum of 77.7 % RH in July corresponding to the temperature maximum. The temperature maximum classifies Ny-Ålesund the

tundra climate according to [Geiger, 1954]. Note that even though the surface humidity levels seem high, there is only little precipitation over the year.
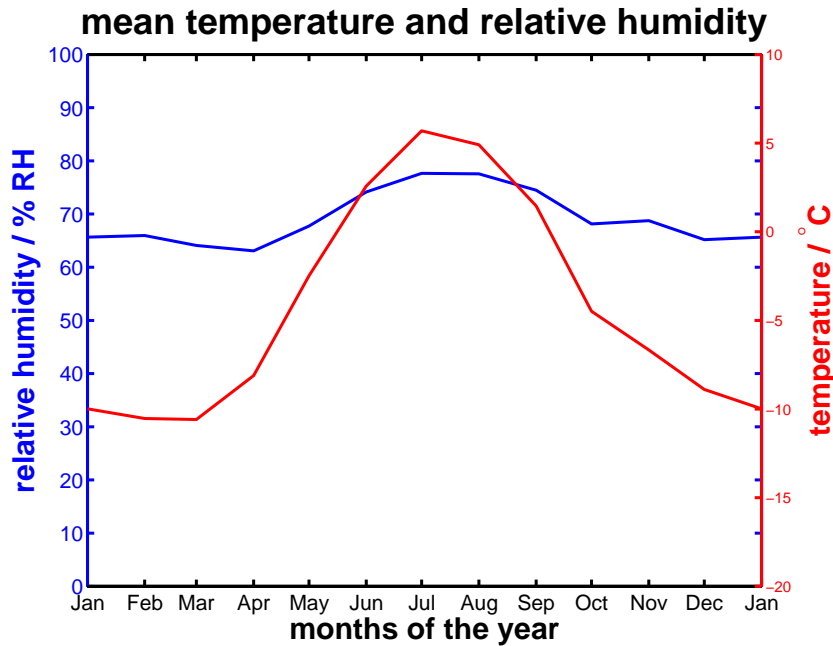
Figure 1: Monthly mean temperature and relative humidity from radiosonde record (1991 to present).

1.3 KEY QUESTIONS

Over the last 20 years the observed BSRN 2 m-temperature shows an increase in annual mean temperature of $(1.3 \pm 0.7)\,°C$ per decade presented by Maturilli u. a. [2014]. The increase is even greater during the winter, $(3.1 \pm 0.6)\,°C$ per decade. This temperature rise is proof of Arctic Amplification. At the same time the net long-wave radiation during winter has increased by $3.9\,W\,m^{-2}$. If both radiation and temperature show an increase, meteorological quantities such as water vapor content and cloud cover could increase as well. Regarding the polar winter, an increase in occurrence of low clouds could already explain the increase in long-wave radiation flux at the surface. An increase in atmospheric water content could also increase the backradiation through the water vapor feedback and therefore enhancing the temperature rise. But literature differs about the role of water vapor under polar conditions. For example does Pierrehumbert [2010] state that the role of water vapor can be neglected for temperatures below 250 K which applies to the Arctic. [Curry u. a., 1995] and also [Staley und Jurica, 1970] in return find the water vapor feedback experimentally and theoretically positive in the Arctic. The change in water vapor content therefore has to be quantified first. Then should the influence of water vapor on Arctic long-wave radiation flux be investigated in order to make an estimate of how sensitive the winter radiation budget reacts to changes in water content. Hence, the aim of this study is to investigate the development in Arctic humidity related quantities over a period from 1991 to present and relating the observed changes to radiation and temperature changes over the

same period, therefor using data recorded from radiosondes, the BSRN field and the ceilometer.

RADIOSONDE HUMIDITY DATA (1991–PRESENT)

Long-term meteorological records are very helpful for identifying climatic changes. But what if these record are in-homogeneous due to a bias introduced by new equipment or a change in measurement location? Imagine an increasing trend in relative humidity of the middle troposphere and a radiosonde, whose humidity sensor experiences a small wet bias in these layers. The bias might be big enough to cover up the trend. After introducing the new instrument the records now show a significant increase. But the trend estimate is biased downward due to the former wet bias. The analyst, just looking at the archived record, might not be aware of the former wet bias. For him the jump in humidity record can be interpreted as climate variability. If he were to account for the instruments disability, the trend could be estimated correctly. Hence, identifying possible sources of error while acquiring data is a key aspect in the study of the climate. This section attempts accounting for known inhomogeneities in the radiosonde data record of Ny-Ålesund where measurements from 1991 to present have been archived conducted with varying radiosonde types, namely Vaisala's RS80-A, RS90 and RS92. The quantity of interest is atmospheric water vapor given in percent relative humidity.

Former studies (Wang u. a. [2009]; Miloshevich u. a. [2004]; Kivi u. a. [2009]),
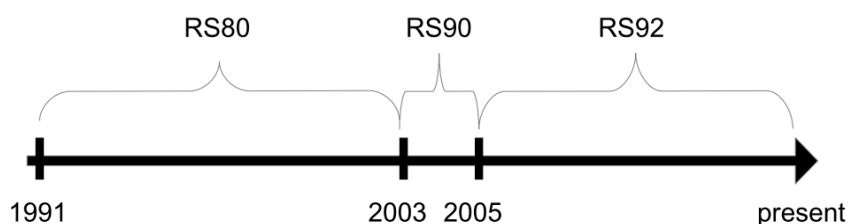
Figure 2: Time-line of radiosondes in use.

point out sources of errors and give empirical corrections for the humidity data. This chapter focuses on combining the various corrections into one algorithm. Vaisala also offers corrections of various biases in the latest DigiCora version. Yet, these procedures are only valid for the RS92 series. As during the period from 1991 to 2003 only RS80-A have been launched at the AWIPEV-station in Ny-Ålesund, an individual correction procedure is needed. This idea was already put to work by Treffeisen u. a. [2007] for an earlier study. The algorithm developed in this work uses for RS80-A data the same corrections as in the former study with slight changes in profile smoothing. For the RS90/92 data the corrections are based on [Kivi u. a., 2009]. The resulting correction algorithm may easily be applied to other stations as long as Vaisala radiosondes have been used.

2.1   MEASUREMENT PRINCIPLE OF HUMICAP-SENSOR

Measuring humidity is more challenging than temperature, because of the non-linear behavior of water and the complicated interactions between water vapor and other atmospheric constituents. Therefore, understanding the working principle of a sensor should always be the first step in characterizing instrumental errors. The HUMICAP-sensor measures relative humidity, usually given as % RH. This quantity is determined by the rate of condensation relative to the rate of evaporation. In other words, it is a measure of how far a liquid or solid and its vapor are from reaching dynamical equilibrium. It can be calculated from the ratio of partial pressure to saturation vapor pressure.

$$RH = 100 \cdot \frac{e}{E_s} \tag{1}$$

here e is the partial pressure and E_s the saturation vapor pressure. The Vaisala HUMICAP-sensor is a type of sorption sensor, i. e. besides measuring the amount of sorbed water a temperature measurement has to be done simultaneously. The HUMICAP-sensor estimates the amount of adsorbed water via capacitance on a miniature capacitor consisting of two plates, one of which allowing the passage of water vapor (figure 3). The medium between the plates has to be non-ionic, in order to be hydrophobic. In addition it is hydroscopic enough to adsorb a small amount of water vapor. Fitting polymers are polyimides, e. g. Kapton, Chen und Lu [2005]. They are hydrophobic with polar functional groups. Vaisala names the polymers used on radiosondes A-type and H-type.

Even though capacitive thin-film sensors are in use for a long time, their work-
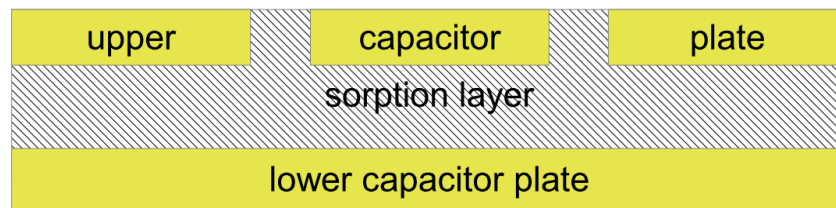
Figure 3: Schematic build-up of a capacitive humidity sensor

ing principle is poorly understood. The change in capacitance is due to the uptake of water, suggesting that the water molecules occupy empty pores in the polymer. Most literature states that the sensor is basically a scale for very small quantities of water [Chen und Lu, 2005] and therefore proportional to specific humidity. This sponge-like behavior implies that the capacitance should vary with temperature as the moisture content changes. But Anderson [1995] showed that the response to a temperature change is weak compared to a change in relative humidity. He suggests a model for the film's absorbtivity. The model implies that temperature and relative humidity inside the polymer film equal those outside. Figure 4 illustrates the basic assumptions. The polar material attracts water molecules forming a thin film of some tens of molecules on the inside surface. The film stays liquid even for temperatures below $-60\,°C$, because a phase a change would alter the capacitance significantly creating a jump in the measurements. But no sudden jumps are observed. The molecules inside the pores can occupy two energy states. The first is inside the liquid, where
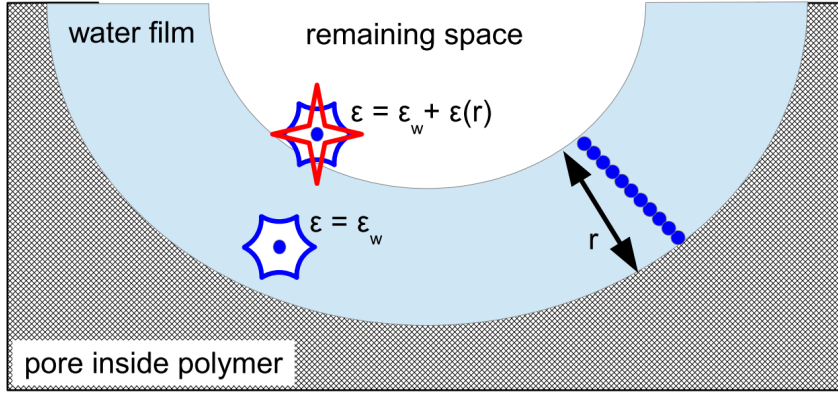
Figure 4: Illustration of absorbtivity model

only the short range forces between the molecules are active with binding energy ϵ_w. In the remaining free space the molecules are in gas phase. Those gas phased molecules closest to the water surface experience the sum of the polymer attraction potential and water binding energy, $\epsilon_{water} + \epsilon(r)$. The magnitude of polymer attraction depends on the film thickness r. The probability of finding a molecule in either state is proportional to the Boltzmann factor $exp(-\epsilon/kT)$. For the given energy states:

$$P(water) \propto exp\left(\frac{-\epsilon_{water}}{k \cdot T}\right), P(gas) \propto exp\left(\frac{-(\epsilon_{water} + \epsilon(r))}{k \cdot T}\right), \qquad (2)$$

where k is the Boltzmann constant and T the ambient temperature. Assuming that the energy states are uniformly distributed, i.e. their number densities are approximately equal.

$$\frac{P(gas)}{exp\left(\frac{-(\epsilon_{water} + \epsilon(r))}{k \cdot T}\right)} \approx \frac{P(water)}{exp\left(\frac{-\epsilon_{water}}{k \cdot T}\right)} \qquad (3)$$

Recalling the definition of relative humidity, RH can be calculated using the ratio of $P(gas)$ to $P(water)$.

$$RH = 100 \cdot \frac{P(gas)}{P(water)} = 100 \cdot exp\left(\frac{-\epsilon(r)}{k \cdot T}\right). \qquad (4)$$

The work by [Anderson, 1995] showed that RH is only weakly dependent on temperature and is a function of the film's thickness r, which depends on the amount of adsorbed water. Thus, the model shows the direct relation between capacitance and RH. This explains slow sensor response under cold conditions, because the rates of condensation and evaporation decrease with temperature. However this ideal model does not include the temperature dependence of r. Theoretical including $r(T)$ the model answers the question why capacitive sensors have problems measuring small RH in the upper atmosphere. Under such conditions r is too little to fulfill the assumption that a molecule inside the film experiences only ϵ_{water}, i.e. assumption 3 is violated. For small RH a resistance based measurement would be more suitable.

Even though the model shows only a weak dependence of RH on temperature, one should keep in mind that RH is only measured indirectly via capacitance.

The dielectric properties of the water are a non-linear function of temperature, making the response to a change in RH non-linear especially for low temperatures. Besides changing the dielectric properties of the polymer its structure can be deformed at low temperature, changing the pore structure and therefore the film thickness. Literally every change in very part of the electronic due to temperature has be accounted for in order to make the measurement accurate. For this purpose Vaisala includes a calibration routine, which is patented under [Stormbom und Lyyra, 1995]. The calibration equations are based on the saturation vapor estimates given by Hyland und Wexler [1983]. In the following corrections and in the subsequent analysis these equations are used even though the WMO recommends the equations stated in WMO [2000].

2.2 VAISALA TYPE RS80-A

The RS80-A radiosonde (figure 5) was used at the AWIPEV-station from 1991 until 2003 for daily soundings. After September 2003 RS80-A radiosondes continued to be used for the weekly ozone soundings for half a year. The sonde is equipped with a BAROCAP-sensor measuring pressure over a range of 1060 hPa to 3 hPa with 0.1 hPa and 0.5 hPa accuracy. A THERMOCAP-sensor measures temperatures from 60 °C down to -90 °C with 0.1 °C resolution and 0.4 °C at 15 hPa. The humidity is measured by the already described HUMICAP-sensor build with the A-type polymer. It can sens RH ranging from 0 % RH to 100 % RH with a best resolution of 1 % RH. The resolution increases non-linearly with decreasing temperatures. At surface pressure and 20 °C the accuracy is < 3 % RH. Therefore a radiosonde should not be launched if the ground-check bias is greater than this accuracy. The default sampling rate is 10 s. Additional information can be found in Technical information: RS80 radiosonde.

2.2.1 *Errors and Corrections*

During the TOGA COARE campaign conducted in 1992 and 1993 a total of 11540 radiosondes from various producers was used [Wang u. a., 2009]. Among them were the type RS80-A and VIZ radiosondes. The Vaisala device showed a substantial dry bias compared to the VIZ sonde, with apparently systematic error. Therefore laboratory work was conducted to identify errors and develop corrections. The errors are related to the measurement principle. They can be categorized in temperature dependence (TD), material contamination (MC) and a time-lag (TL) introduced by the long response time under cold conditions. The corrections follow the approach of Wang u. a. [2009] and Miloshevich u. a. [2004]. There are other biases such as a heating of the sensor due to solar radiation, but they can be neglected compared to the TD, MC and TL error and therefore not corrected in this study.

It is important to know that each sensor is calibrated by a 2 point measurement upon production at -30 °C at 45 °C. Right before launch a ground-check (GC) is performed to account for any drifts in the sensor. The easiest method for correcting the biases mentioned above is therefore by first removing the GC correction ΔU_{GC} and the basic calibration model.

Figure 5: Picture of RS80 radiosonde taken from Technical information: RS80 radiosonde

If ΔU_{GC} is listed in the meta-data it is recommended to subtract it from the measured profile U_m. If this it not the case, an estimate using the sonde age d is found in [Wang u. a., 2009]:

$$\Delta U_{GC} = 0.0666 + 0.8 \cdot d - 0.104 \cdot d^2. \tag{5}$$

The basic calibration can then be removed using, according to [Wang u. a., 2009]:

$$U = -2.22168 + 0.999634 \cdot (U_m - \Delta U_{GC}) + \\ + (0.11108 + (1.831\,05 \times 10^{-5}) \cdot (U_m - \Delta U_{GC})) \cdot t, \tag{6}$$

where t is the ambient air temperature in degrees Celsius and U_m the measured humidity profile.

Contamination error – refers to a contamination of the polymer due to the plastic packaging. The plastic molecules occupy the binding sights of the polymer effectively lowering the materials ability to adsorb water molecules. Since the polymer's structure is hydrophobic and only hydroscopic due to functional groups a non-water molecule reduces the polarizability of the material. This reduces $P(gas)$ creating a dry bias and making the error a function of exposure time to the plastic, i. e. knowing the radiosonde age is crucial. The average contamination bias is therefore determined as

a function of d and U by fitting a polynomial. The equation presented in [Wang u. a., 2009] is used for this purpose.

$$C_C = (k_0 + k_1 \cdot d + k_2 \cdot d^2) \times$$
$$\times ((p_0 + p_1 \cdot U + p_2 \cdot U^2 + p_3 \cdot U^3). \quad (7)$$

The values of constants k_i and p_i are listed in 3 found in the Appendix. The producer being aware of the contamination tried to reduce the bias first by changing the packaging. This lead to a bias reduction of 30 % to 50 % in radiosondes produced after September 1998. The CM was finally removed in June 2000 by shielding the sensor with a cap of non-contaminating material.

Temperature dependence error – is the result of an in-accurate temperature calibration. The non-linear behavior of the sensor material requires a correction. However the applied model has proven in-sufficient under cold conditions and high humidity levels. Note that the routine used for the RS80-A is based on the Hyland und Wexler [1983] equation for equilibrium vapor pressure. Thus additional research was conducted at Vaisala's laboratories, essentially developing a better temperature dependence calibration. Note that this correction is a function of t and U and needs to split into two corrections. The first, C_H, accounts for the response of the polymer to different RH.

$$C_H = H_0 + H_1 \cdot U + H_2 \cdot U^2 + H_3 \cdot U^3 + H_4 \cdot U^4. \quad (8)$$

The temperature dependent part of the correction is based on measurement of RH at saturation, [Wang u. a., 2009]. The difference between ambient RH and sensor output is according to [Wang u. a., 2009] approximated by a 5th order polynomial.

$$C_T' = T_0 + T_1 \cdot t + T_2 \cdot t^2 + T_3 \cdot t^3 + T_4 \cdot t^4 + T_5 \cdot t^5. \quad (9)$$

The H_i and T_i are listed in tables 4 and 5 in the Appendix. In order to quantify the full TD correction it is convenient to first define a corrected humidity due to corrections regarding the dependence on RH alone, i. e. the MC and C_H correction.

$$U_c = U + C_C + C_H. \quad (10)$$

Applying the inverse of 23 gives the RH corrected profile in terms of the basic TD-model, U_c'. The temperature dependent part must be proportional to U_c'. Because C_T' is a measure of dry biased saturation vapor pressure, the proportionality is determined by C_T' relative to its difference to the maximum RH over liquid water U_{max}. For values of $t < 0\,^{\circ}\text{C}$ this is given $U_{max} = 99.8526 + 0.9442t + 0.0034t^2$ and $U_{max} = 100\,\%\text{RH}$ for values of $t > 0\,^{\circ}\text{C}$. Therefore the total (TD) corrections, [Wang u. a., 2009], is given by

$$C_T = \left(\frac{U_c'}{U_{max} - C_T'} \right) \cdot C_T'. \quad (11)$$

Because C_T' is dry biased it will always be smaller than U_{max} and the correction C_T always positive. Note the TD-correction can be very large, especially at low temperatures, e. g. is the corrected RH approximately 75% greater than the measured, [Miloshevich u. a., 2004]. Now the bias corrected humidity profile can be given as the sum of the corrections, also including the ΔU_{GC}.

$$U_{corr,bias} = U_c' + \Delta U_{GC}. \tag{12}$$

Time-lag correction – due to the long response at low temperatures the recorded profiles a change in ambient RH is seen a couple of hundred meters away, thus erasing the profile's structure. According to [Miloshevich u. a., 2004] the time-lag becomes significant for temperature below $-40\,°C$. For tropospheric records the time-lag can almost neglected. Recalling the measurement principle, one might ask, if stratospheric readings conducted by a capacitive sensor can be trusted at all, because the water content is to small to keep the number densities of $P(gas)$ and $P(water)$ constant under changing RH. Despite this a time-lag correction can easily be established as described in Miloshevich u. a. [2004]. Assuming that the sensor response exponentially to a change in RH and implying that bias corrections have been already applied:

$$\frac{dU_{corr,bias}}{dt} = \frac{1}{\tau(T)} \cdot (U_a - U_{corr,bias}), \tag{13}$$

where T denotes the temperature in degree Celsius and t the time in seconds. Note that other monotonically increasing quantities can also be used for the differentiation. All that must be known is their proportionality to τ. The solution to the differential equation is

$$U_{corr,bias}(t) = U_a - (U_a - U_{corr,bias}(t_0)) \cdot exp(\frac{-\Delta t}{\tau}). \tag{14}$$

Here $\Delta t = t - t_0$ and t_0 being the time when the sensor was exposed to U_a. Inverting this expression and discretizing, the ambient profile at time t_i can be determined through

$$U_a(t_i) = \frac{U_{corr,bias}(t_f) - U_{corr,bias}(t_i) \cdot exp(-(t_f - t_i)/\tau)}{1 - exp(-(t_f - t_i)/\tau)}. \tag{15}$$

This is the correction given in [Miloshevich u. a., 2004]. Because this procedure is sensitive to spikes, i. e. large RH-gradients, some sort of smoothing has to be applied to the calculated profile. The cited work proposes a smoothing based on minimum jerk trajectories which implies setting up a skeleton profile with higher resolution. The GRUAN processing uses a low-pass filter. But for this study the MATLab-routine *supsmu.m* based on [Friedman, 1984] was used mainly out of convenience and because no skeleton profile is needed. The magnitude of this correction depends on the time constant τ. The constants were determined through exponential fits using data given in [Miloshevich u. a., 2004]. Now the profile U_a shall be referred to as the fully corrected profile U_{corr}.

sensor icing – The correction offers also a need way of identifying cases of
sensor icing, one of the major disabilities of the RS80-series. Sensor ic-
ing occurs when the ice condenses on the outside of the HUMICAP. The
air reaching the polymer film is therefore filtered through this ice cod-
ing and the readings do not resemble the ambient air anymore. Hence,
data of an iced sensor shall be excluded from the analysis. Because the
air inside is now ice saturated and because the sensor always measures
the RH with respect to liquid water, the recorded data is resembles the
ratio of $RH_{sat,water}$ relative to $RH_{sat,ice}$. This can be used, because it
also means that the corrected profile should be very close to this ratio. To
calculate this ratio the recorded temperature profile and the knowledge
that Vaisala uses [Hyland und Wexler, 1983] equation for saturation va-
por pressure is needed. Setting a suitable threshold for the mean relative
difference between the ratio and the profile would be a criterion of iden-
tifying sensor icing. Even better would be polynomial fit, whose running
standard deviation is not allowed to leave certain limit in order to be clas-
sified as sensor icing. Figure 6 gives an example of sensor icing. The blue
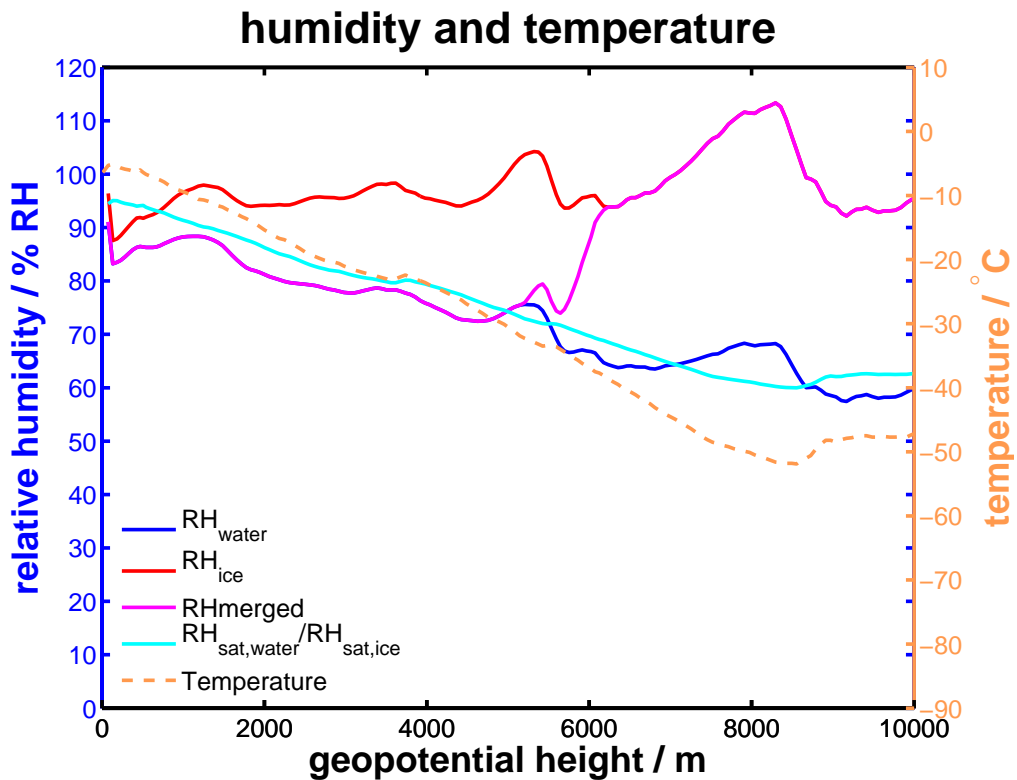
Figure 6: Demonstrative example of sensor icing (1993/04/26)

line describes the corrected profile. The humidity readings are unusually
high across the entire column, plus its deviation from the ratio (cyan line)
is small across the entire troposphere. One can assume that this was not a
realistic measurement. Using this criterion 230 cases of sensor icing have
been identified of 8716 radiosoundings with a higher frequency during
the the winter month.

2.3 VAISALA TYPE RS90/92

The type RS90/92 radiosondes (figure 7) were designed to correct the major biases of the RS80-A series. RS90/92 is equipped with two H-type HUMICAPs heated alternately. One sensor measures while the other is heated to get rid of any condensed water or ice. This prevents the effect of sensor icing. According to Technical information: RS92-SGP radiosonde other parts of the device have been improved as well, e.g. the default data sampling rate is now 5 s. The data sheet also shows that resolution and accuracy are determined more carefully. The RS90/92's THERMOCAP measures over a range of 60 °C to −90 °C for pressures from 1080 hPa to 3 hPa with accuracies of 0.2 °C to 0.5 °C and 0.1 °C resolution. The BAROCAP has a resolution of 0.1 hPa. From 1080 hPa to 100 hPa its uncertainty is 1 hPa and in the range from 100 hPa to 3 hPa approximately 0.6 hPa. As for the HUMICAP, the average uncertainty is 5 % RH. Because its resolution is mostly effected by the sensor response time. The response time for surface conditions is < 0.5 s at surface pressure and 20 °C and just < 20 s at surface pressure and −40 °C. The data in Technical information: RS92-SGP radiosonde gives no information on the HUMICAPS temperature range.

Figure 7: Picture of RS92 radiosonde taken from Technical information: RS92-SGP radiosonde

2.3.1   *Errors and Corrections*

The errors have greatly been reduced from the RS80-A to the RS90/92 type. A better calibration procedure and a change to the H-type polymer allow neglecting the TD error. No contamination error is present due to better packaging and polymer improvements. The TL error is also reduced, because the H-polymer has a faster response time. However preventing sensor icing via heating made design chances necessary. The two HUMICAPs are not shielded against solar radiation anymore. So the incoming short-wave radiation can heat the sensors during daytime launches. The effect by night-time long-wave radiation can be neglected. The error is thereby referred to as day-time radiation dry bias (RB).

Radiation dry bias – Corrections to this error are difficult, because the radiation uptake depends on the ambient weather conditions. A sensor passing through a cloud is shaded by the cloud. The bias originates just like the TD bias for the RS80-A from the temperature calibration procedure. Only this time violating the assumption that the THERMOCAP temperature equals the HUMICAP temperature. Disregarding the different materials, the THERMOCAP's geometry is that of a wire, the HUMICAP resembles a sphere. Their thermal capacities are therefore different and so is their potential heating due to radiation. Now the error results from the fact, that there is no temperature measurement of the HUMICAP. The calibration model assumes both sensor temperature to be equal. Hence, the key for correcting this error estimating the heating of the HUMICAP while only knowing the error of the THERMOCAP. Several approaches can be found, e. g. the GRUAN correction procedure uses a radiation model to estimate the incoming solar irradiance and the assumption that the heating is a function of irradiance, ventilation speed, i. e. ascent speed and pressure as a height coordinate. Vaisala has established a correction method as well, which is included in the DigiCora version starting from 2011. Before that, a changes in the device were made, such as introducing a reflective cooling in late 2006, which weakens the RB error. The Vaisala humidity correction is proprietary information. But the producers website provides tables that relate the error in the temperature reading to the sun elevation. For the geographic position of Ny-Ålesund the table states a maximum temperature error of $\approx 0.5\,°C$ in the upper troposphere under polar daytime conditions. The full correction tables can be found in the data continuity section on the Vaisala website. As an example only the temperature corrections of the oldest sensor generation are given as a function of pressure for a sun elevation of 30° (table 1).

The maximum sun elevation at Ny-Ålesund is $\approx$ 30°. This also illustrates that a reasonable correction method using the given temperature biases should be a function of pressure. Kivi u. a. [2009] suggest an em-

Pressure level	Sea level	500 hPa	200 hPa	100 hPa	50 hPa
ΔT_{corr}	0.04 °C	0.12 °C	0.25 °C	0.36 °C	0.46 °C

Table 1: Excert from temperature correction table for sun elevation of 30°

pirical correction based on data acquired during a campaign in northern Finland during February to August 2009. For the correction method the RS92-humidity data is compared to simultaneous CFH (Cryogenic Frost-point Hygrometer) launches, all under the assumption that the frost-point hygrometer best represents the ambient RH profile. The study uses the relative difference between the two instruments to determine a pressure dependent correction factor. The coefficients of this correction function are determined by fitting the following polynomial, [Kivi u. a., 2009]:

$$\frac{U_m - U_{CFH}}{U_{CFH}} = R_0 + R_1 \cdot \ln(p) + R_2 \cdot (\ln(p))^2, \tag{16}$$

where p denotes the pressure, U_m the RS92 humidity and U_{CFH} the CFH humidity. The coefficients R_i are listed in tables 6 and 7 in the Appendix. There are two sets of coefficients, one for the sensor with additional reflective coding and one for the older type without the coding. If the right-hand sight of 16 is summarized as $y(p)$ and suppose if the CFH profile is the corrected one, the correction coefficient C_{Rad} can be written as

$$C_{Rad}(p) = \frac{1}{y(p) + 1}, \tag{17}$$

and hence the corrected humidity profile $U_{corr} = C_{Rad} \cdot U_m$. This correction however does include neither the change in sun elevation over the seasons nor the shading of clouds. It therefore gives only an average correction for polar day conditions. Note that other corrections, e. g. GRUAN, are using a radiative transfer model treating this error. But they are also doing an average correction for all sky conditions, because they cannot account for the cloud distribution present when the sounding was conducted. So their averaging has probably a smaller standard deviation. In order to improve the method by [Kivi u. a., 2009] it is fair to use the temperature corrections published on Vaisala's website. For this study the full radiation correction is therefore defined as the RB_{Kivi} referring to maximum sun elevation, tropopause pressure levels and maximum temperature error ΔT_{max}. Assuming that C_{Rad} is linearly proportional to ΔT, the sun elevation sensitive radiation correction can be expressed via

$$C'_{Rad}(p, h) = \frac{1}{\Delta T(p,h)/\Delta T_{max} \cdot y(p) + 1}, \tag{18}$$

where h denotes the sun elevation angle. So the corrected profile of a RS90/92 sounding reads

$$U_{corr} = C'_{Rad}(p, h) \cdot U_m. \tag{19}$$

This approach is probably not worse than the ones used in GRUAN or the DigiCora, but not as flexible as the latter ones. Because these corrections are empirical based and most effective in the upper troposphere and stratosphere, where the measurement principle of a capacitive humidity sensor is pushed to its limits, it can be concluded that the developed algorithms are only able to apply an average correction to the individual

profile. Some profiles will be over-corrected and other under-corrected. In order to avoid over correction only 90 % of the RB correction is applied to the profile. This implies that interpretations based on the individual profiles should be treated carefully. However making the statements about the average over an ensemble of soundings, such as monthly means should be possible without making a systematic error.

Time-lag error – the TL error is still present, but in the troposphere hardly noticeable because of the faster sensor response time. It is corrected according to 2.2.1 but with a different time constant τ, according to [Miloshevich u. a., 2004].

2.4 CORRECTION ALGORITHM

The corrections for RS80-A and RS90/92 can be combined into a correction procedure which corrects the biases described in the previous sections. This makes the meta data exceptionally important, because it includes the local time of a radiosonde launch and the calibration date. From other sources documented changes in the ground equipment are necessary as well. As mentioned, the DigiCora version released in 2011 includes an unknown error correction procedure somehow based on the cited work. Therefore no corrections are applied after the new DigiCora version was established. Additionally some errors cannot be corrected at all, because they are a result of the default data processing. The data is archived in an *.EDT-file* which uses integer values. This introduces an uncertainty of ± 0.5 %RH. Because the used data is entirely in this format, there is no chance in correcting for this error. Another important source of error is the GC. If the desiccant does not create a 0 %RH environment, the correction cannot be accurate. Because this correction affects the entire profile, it is also a source of error which cannot be accounted for. This is part of the reason for subtracting the GC correction in the RS80-A procedure. The schematic correction procedure used in this study in shown in figure 8.
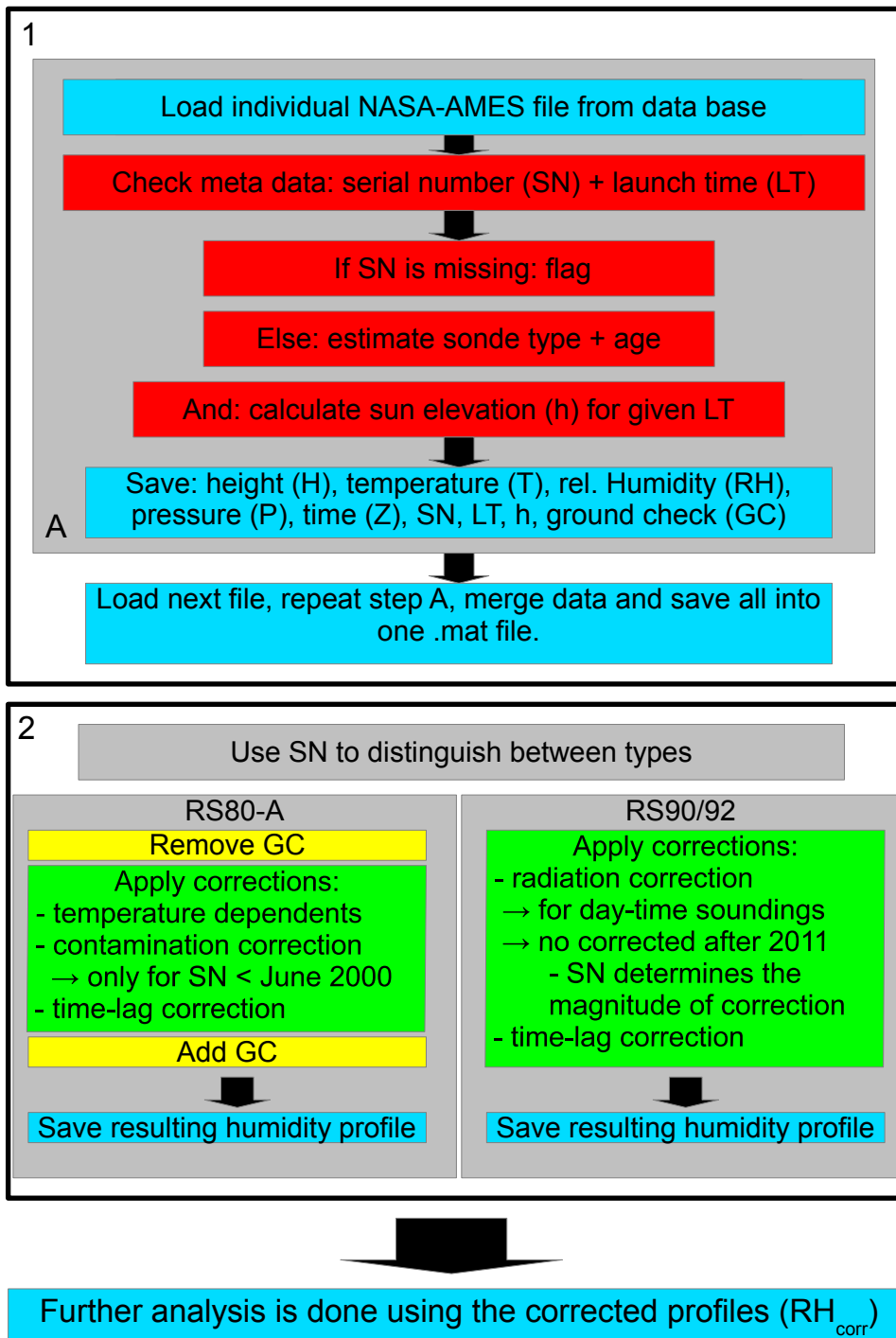
Correction procedure

Figure 8: Correction scheme

2.5   RESULTING HUMIDITY PROFILES

The aim of the corrections is to make the data more homogeneous in order to identify trends in parameters calculated based on the humidity measurements. This section compares the corrected and uncorrected data sets, qualitatively. First a change in monthly averaged humidity profiles is depicted in figure 9. The large change is seen in 2003 when the radiosonde type was switched from using RS80 to RS90/92. As expected, their is little change due to the corrections in the lower troposphere and only a small change during the RS90/92 period. The corrections become visible only at heights above 5000 m. In fact the upper troposphere measured by the RS80-A seems to be somewhat over-corrected. But the overall picture appears homogeneous. In order to have a better look at what happens to high RH values a look at a high percentile is suitable. Figure 10 shows the 90th-percentile for each month before and after corrections. Now the corrections appear clearly during both radiosonde periods. Even though the RS80-A humidity again appears over-corrected. One reason for that could be that the corrections are tuned to fit tropical and laboratory conditions, recalling their development subsequent to the TOGA COARE campaign. Another is the measurement principle, which works well for medium to high RH values but according the model only poorly for small RH under cold temperature. The Arctic troposphere might just be to extreme. Nevertheless, no further correction is applied to account for this. Regarding the other correction procedures, a reasonable approach would be to take the CFH sondes launched at Ny-Ålesund to derive an empirical Arctic correction factor. How does an individual sounding look before and after correction. Figure 11 illustrates the changes to a typical RS80-A sounding.

The black line is the measured profile, red resembles the corrected profile for RH over liquid water. The green profile shows RH over ice and the magenta line illustrates the maximum reachable RH over liquid water, wich is limited by the saturation over ice. The overshoot of the corrected profile near the tropopause could be an error due to correction, evidence of super cooled water or evidence that the limits of capacitive measurements are reached. However it illustrates that this region is dominated by ice saturation. Next looking at figure 12, one observes that the correction for a typical RS92 profile is small. Note that the overshoot in the upper troposphere is also present.

Monthly mean of measured RH

(a) uncorrected

Monthly mean of corrected RH

(b) corrected
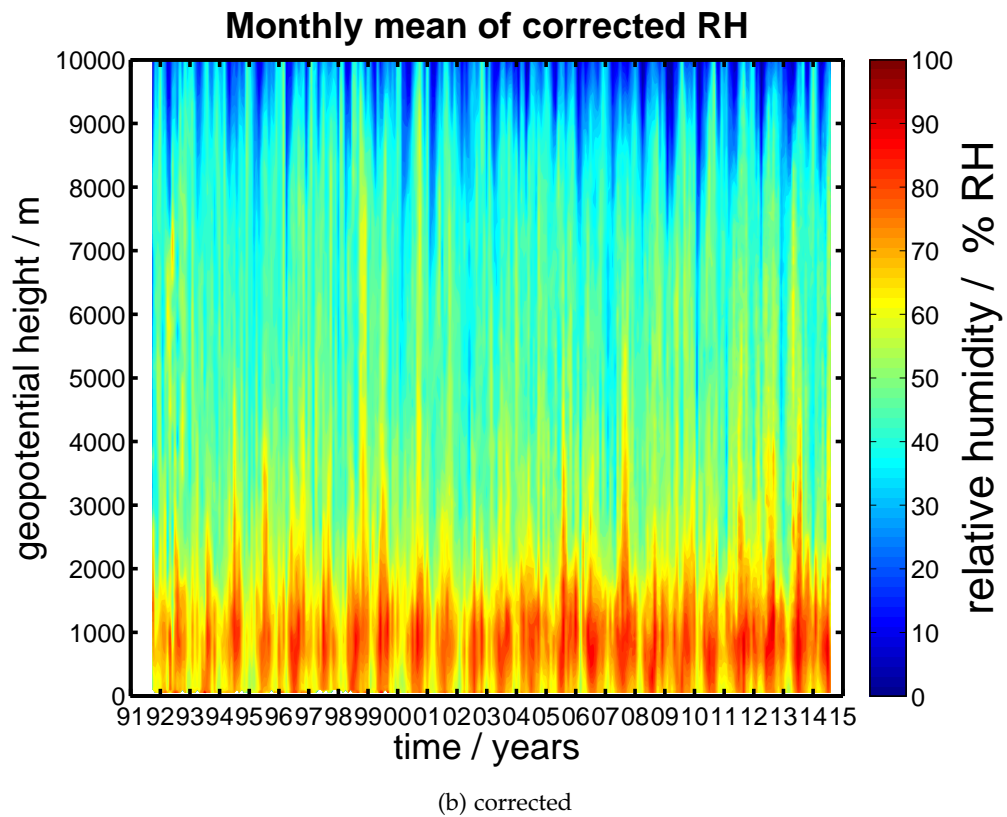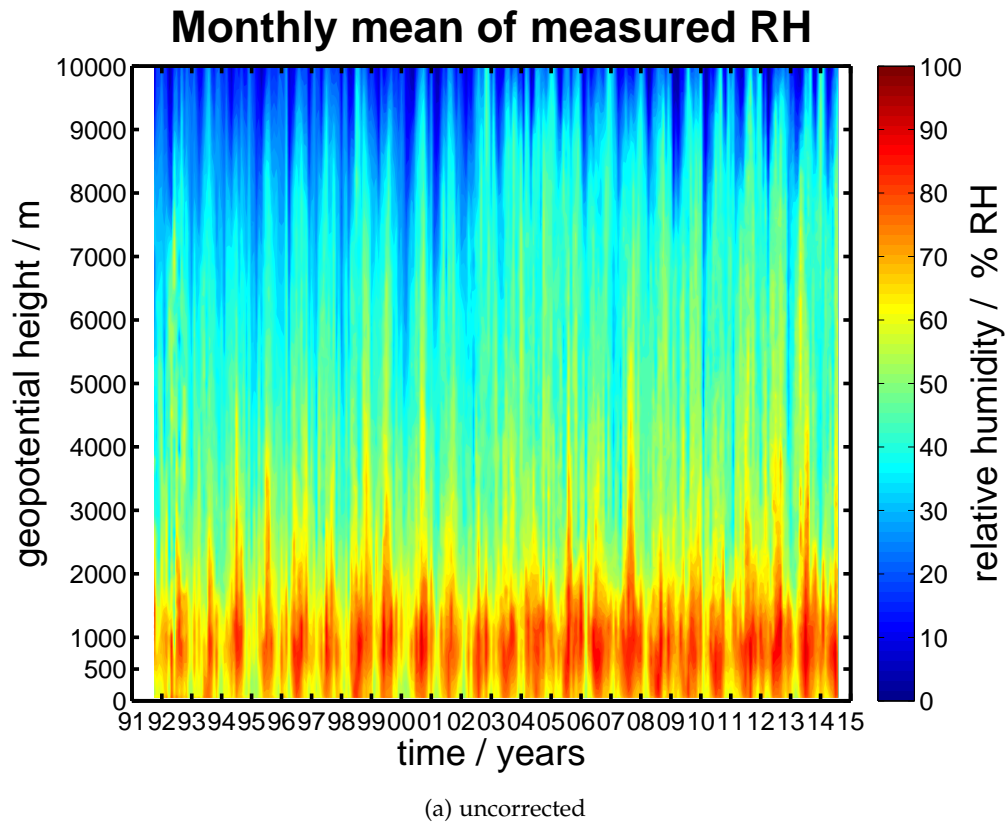
Figure 9: Comparison of monthly mean RH profiles obtained from radiosoundings (1992 to present).

90th percentile of monthly RH, measured

(a) uncorrected

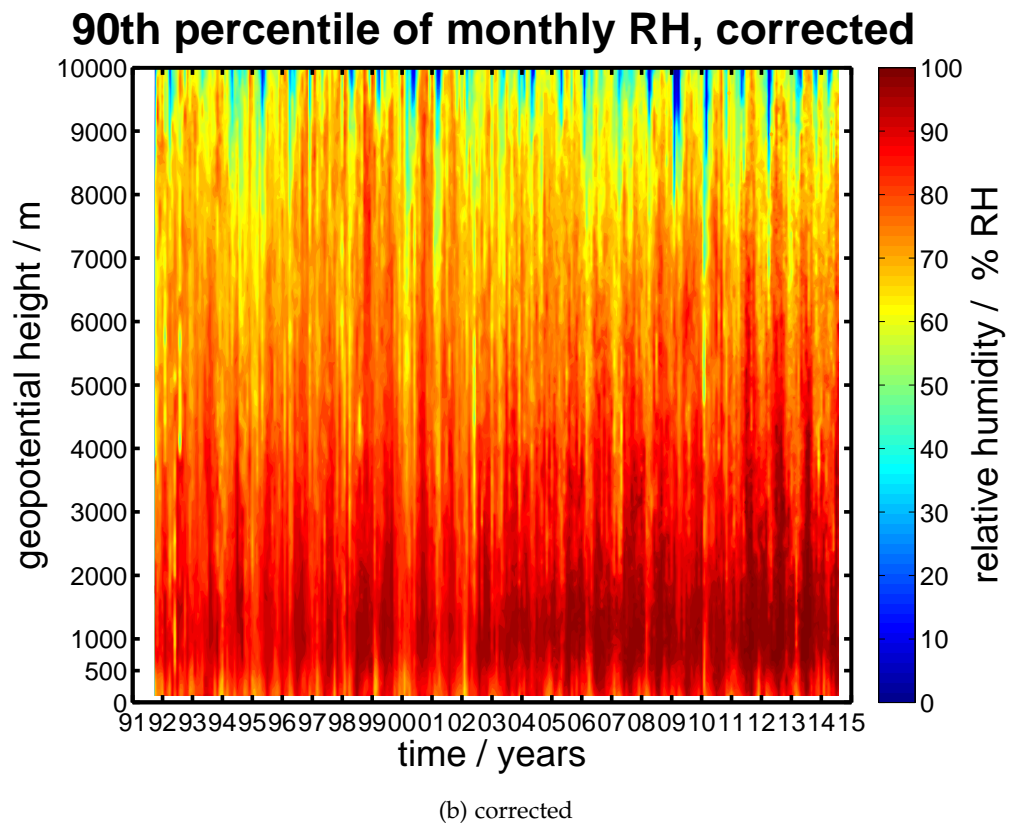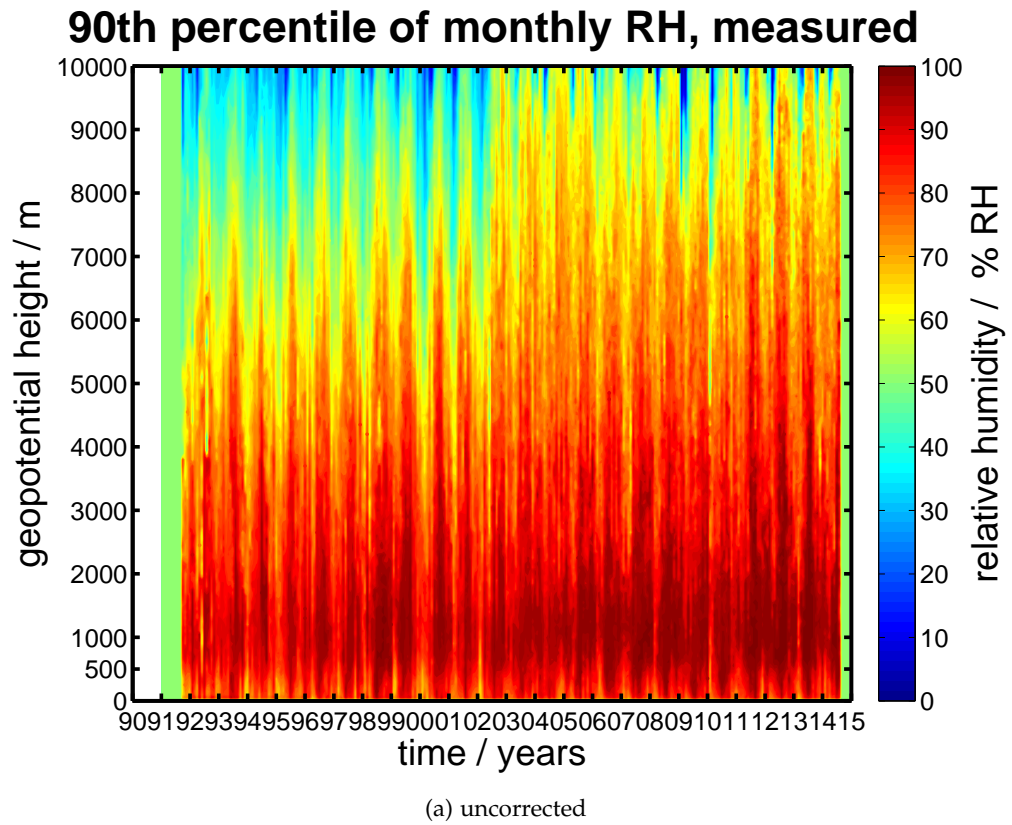## 90th percentile of monthly RH, corrected

(b) corrected

Figure 10: Comparison of monthly 90th-percentile RH obtained from radiosoundings (1992 to present).
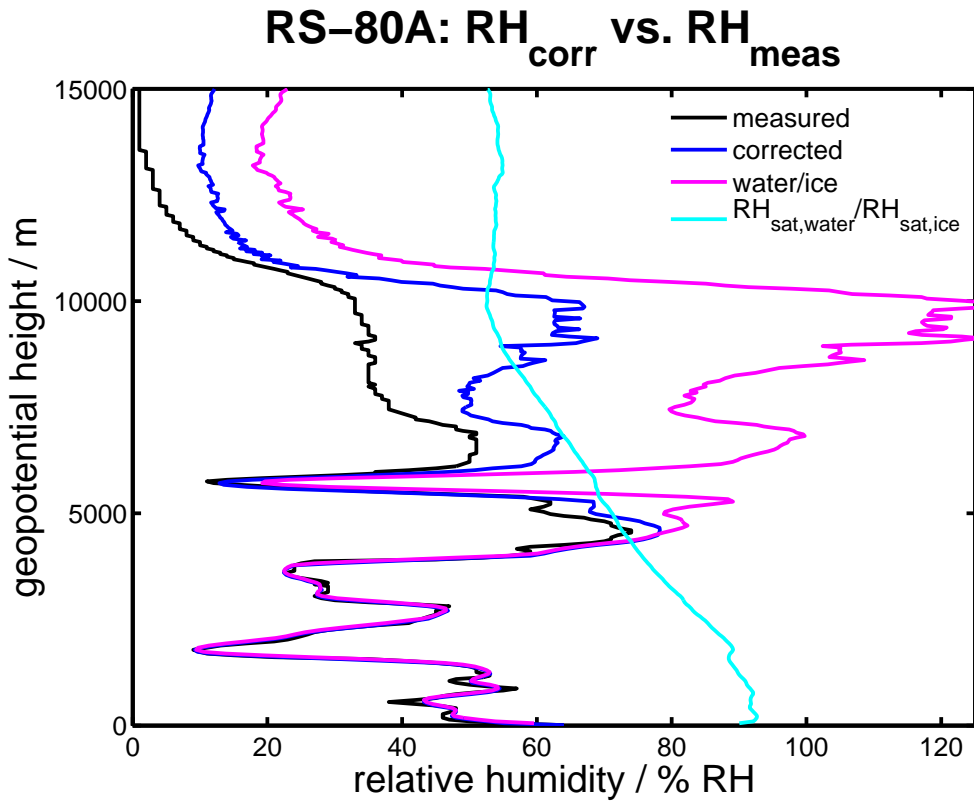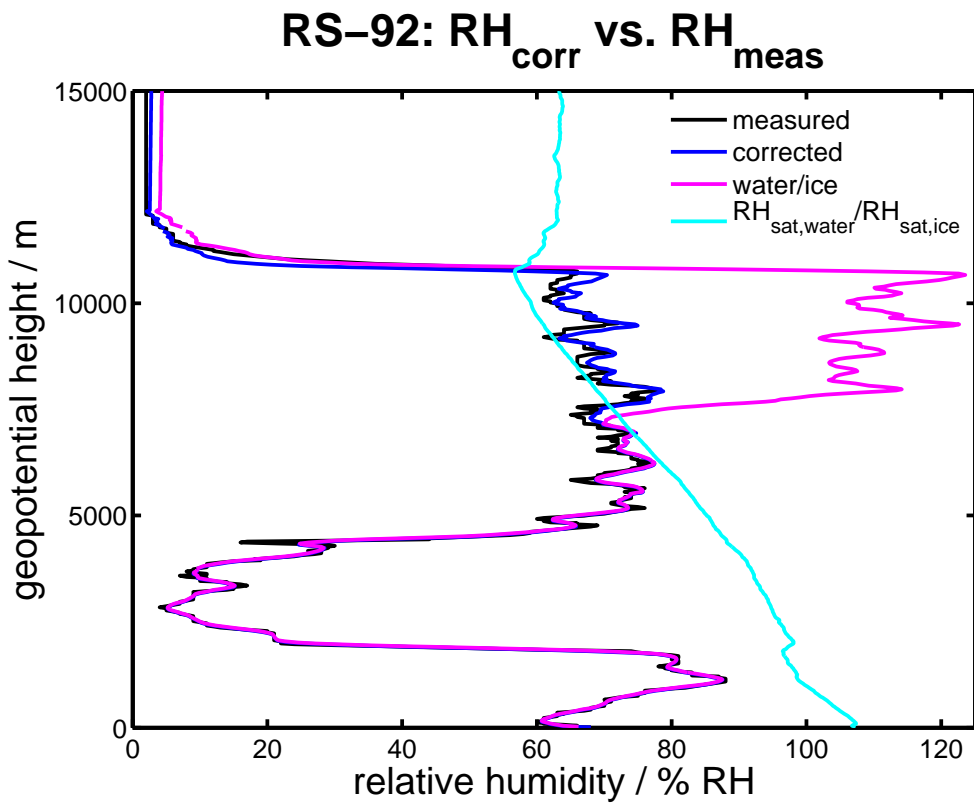
Figure 11: Correction applied to RS80-A sounding (1994/01/22).

Figure 12: Correction applied to RS92 sounding (2005/08/14).

A reasonable explanation for the markedly overshoot can be found in estimating the corrections uncertainties. Because the magnitude of the corrections changes as the sensor is improved, the uncertainties undergo a similar change. Another factor in determining uncertainties is seasonal change. The HUMICAP's performs poorly under very cold conditions. Even if the profile is corrected for known systematic errors, a deviation in measurement error remains. This intrinsic measurement error is not systematic and should vanish when means are calculated with the data. But the individual sounding is sensitive to such errors. However it should be expected, that magnitude of non-systematic error has changed when the polymer switched from A-type in the RS80 to H-type in the RS90/92. Additionally, the contamination and the radiation correction are examples for corrections which also show a random error component, due to their correction estimates. The correction functions for the contamination error were developed using a sample of differently contaminated sensors. The degree of contamination was measured as sensor response in a climate chamber and estimated to be a function of sensor age. Differences in sensor performance due to different badges and random are therefore included in the corrections and generate a random error component. Similar reason can be noted for the radiation correction. Looking at the paper, one notices the large scatter in the data values used for the fit, [Kivi u. a., 2009]. The correction is only an average correction. Some profiles could be over-corrected, some under-corrected. Other corrections, such as the TD correction have only a small random component mainly due to uncertainties in the fitting constants. When not corrected it applies a wrong temperature dependence calibration to the data. Correcting the error is merely a re-calibration than a correction.

For these reasons this study will not execute a lengthy uncertainty calculation, rather assuming that the current implied correction gives the best estimate of the ambient humidity profile so far. Hence, the corrected old profiles are compared to the newer non-corrected radiosonde measurements. For this purpose the normalized range $\mathrm{RANGE_N}$ and the variation coefficient VarC are calculated for RS80 and RS92 corrections. The estimators are defined as

$$\mathrm{range_N} = \frac{\max^{\mathtt{monthly}}(\mathrm{RH_i}) - \min^{\mathtt{monthly}}(\mathrm{RH_i})}{\mathrm{mean}^{\mathtt{monthly}}(\mathrm{RH_i})},$$

$$\mathrm{VarC} = \frac{\mathrm{STD}^{\mathtt{monthly}}(\mathrm{RH_i})}{\mathrm{mean}^{\mathtt{monthly}}(\mathrm{RH_i})},$$

$$(20)$$

where the subscript i denotes for the either algorithmic corrected profiles or corrected by the DigiCora. The index $\mathtt{monthly}$ indicates that the coefficients are are first calculated for every month and for all years. The resulting profiles are than determined from the average over all monthly values. These coefficient are all measures of variability. If the corrections have a coefficient similar to that of the DigiCora corrections, they are capable of recovering the ambient humidity profile sufficiently for the following analysis. The coefficients are shown in figures 13 and 14. The black solid line resembles the desired Digi-

Normalized range for corrected and uncorrected data

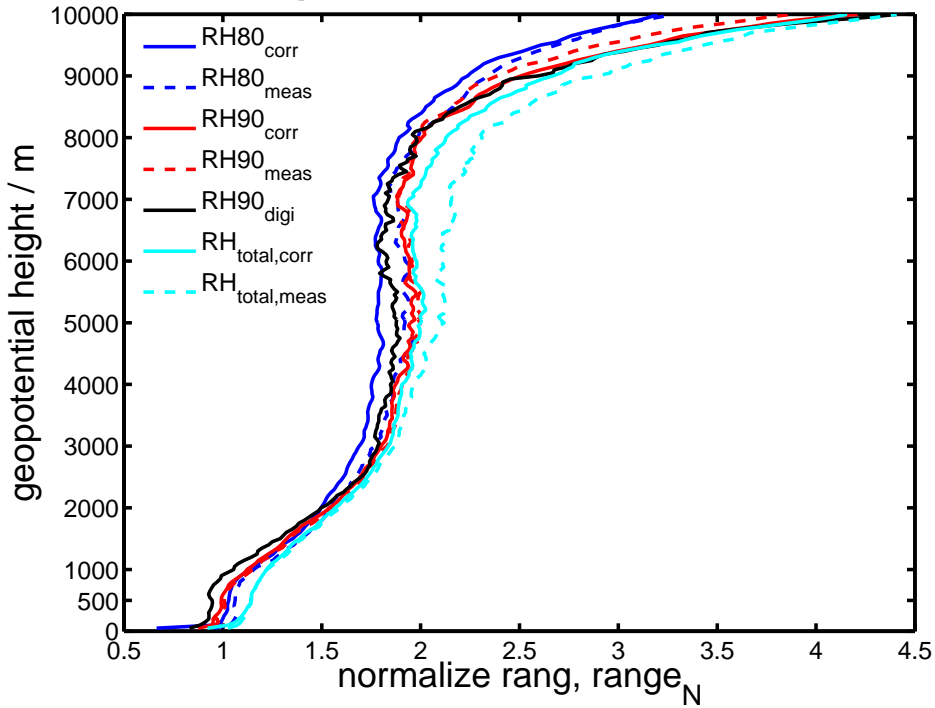Figure 13: Mean of normalized rang of different corrected and measured humidities.

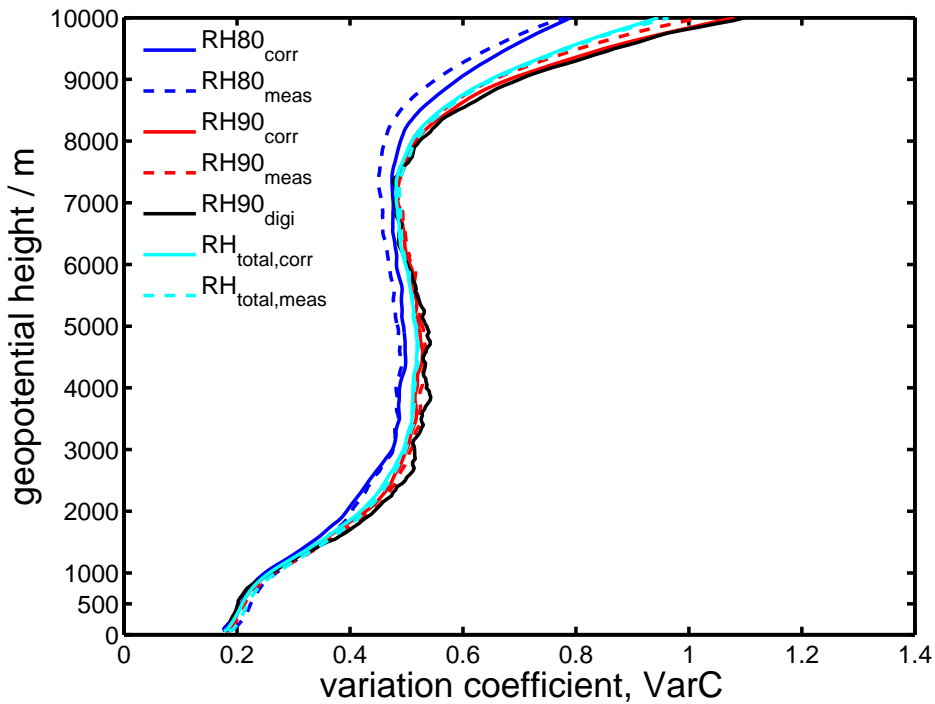**Variation coefficient for corrected and uncorrected data**

Figure 14: Mean of variation coefficient of different corrected and measured humidities.

Cora correction. Looking at the ensemble of measured profiles one sees that the range shows the greatest discrepancy to the desired curve. The RS90 corrections

are small in magnitude and differ therefore little from the implicit correction. The RS80 corrections show smaller range which can probably be attributed to slower sensor response time. The total picture from the range estimate appears to be good. The correction algorithm does not change the range, it is actually slidely improved. The variation coefficient in figure 14 offers a similar picture. The RS90 data looks quite alike. Only the RS80 profiles differ significantly from the DigiCora correction. This difference is reduced through the applied corrections. Hence, this coefficient also shows an improvement and states that the RS80 data is now better comparable to RS90/92 data. However the two estimators give inside in another aspect which lowers the sensors credibility. The enormous increase of both coefficients is probably associated with the beginning of the tropopause, i.e. cold ambient air and very low RH. The sensor is exposed to its limiting conditions. Therefore for follow up studies the idea of a cutoff altitude for humidity profiles around 8 km should be considered due to the great decrease in data quality.

As a second estimate of the corrections quality and the homogeneity of the corrected data consider the following. The sensor has problems measuring in cold and dry ambient conditions. Hence, the worst conditions are probably encountered during the winter time. Now a threshold temperature T_{th} is defined to classify exceptional cold soundings, here $T_{th} = -30\,°C$. Next a threshold altitude, here $H_{th} = 4\,km$. Select only those winter humidity profile where the corresponding temperature profile read a temperature below or equal T_{th} at height H_{th}. Now distinguish among these selected profiles between DigiCora corrected and others. The next step is creating histograms of the selected data set and comparing them. It is hoped, that the corrected histogram is close to the DigiCora corrected. Figure 15 shows the resulting histogram for the winter period. It is noticed that the correction decreases the dry bias, because the count of high humidity (green) has increased compared to the measured profile (red). However comparing it to the DigiCora correction it seems that the high count values are too high, suggesting a slight over-correction. Next the procedure is done for all seasons, figure 16. Again the corrections reduce the dry bias. Also, now that all seasons are included, the former wet bias is reduced. DigiCora correction and the own correction look alike. This means, that the corrected data should be homogeneous enough to conduct an analysis. However, because the most interesting season for this study is the winter, a more robust moisture quantity should probably be put in the focus. Such a quantity would be the column integrated water vapor. Because most of the water mass is located in the lower troposphere during the Arctic winters, the influence of the sensor dry bias is small and therefore the influence of an over-correction as well.

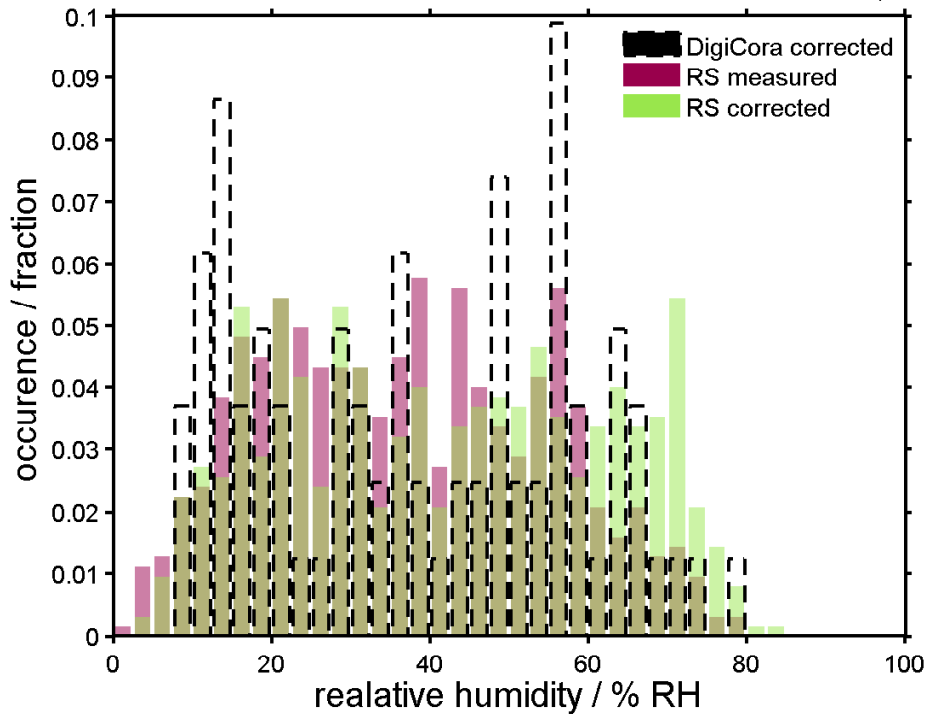## Mean RH values in 4000 to 7000m altitude, DJF

Figure 15: Humidity correction under cold conditions, DJF.

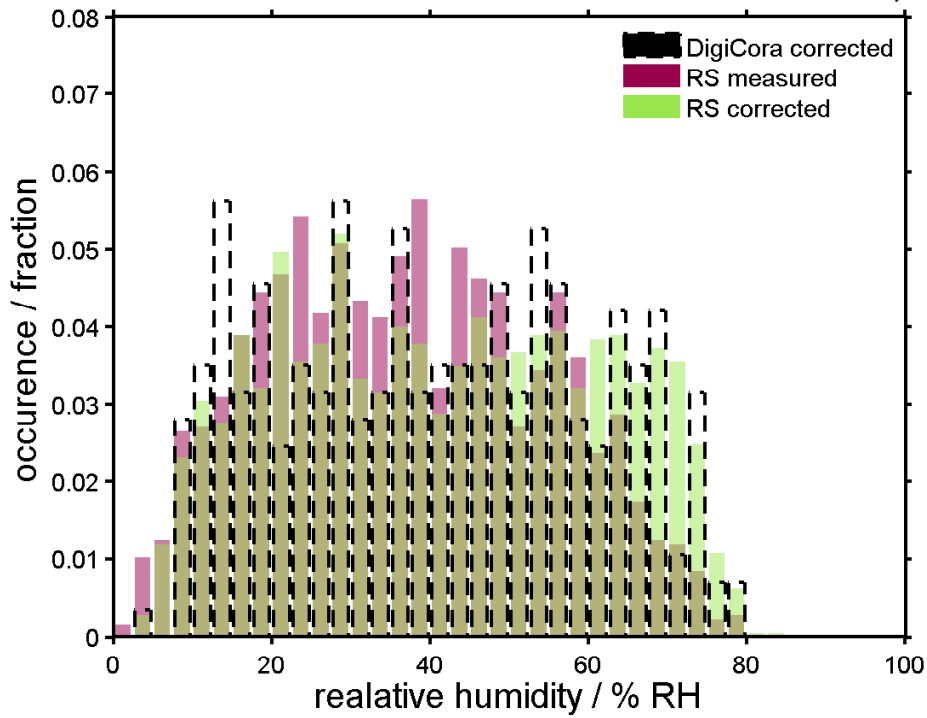## Mean RH values in 4000 to 7000m altitude, all

Figure 16: Humidity correction under cold conditions, all seasons.

CLIMATOLOGY OF VERTICAL HUMIDITY-PROFILES

This section aims to point out characteristics of the measurement location Ny-Ålesund. Because the settlement is located next to a fjord surrounded by mountains, all meteorological recordings will be affected by this orographic influence. This emphasizes the need to characterize local influences via a brief climatology first before investigating the influence of other factors.

3.1 23 YEARS NY-ÅLESUND RADIOSONDE PROFILES

3.1.1 *Seasonal cycle*

The site is a unique observation point right at the border between sub-polar and high-polar zone, i. e. the atmospheric weather conditions are markedly dominated by ice saturation RH_{ice} during the cold half of year. Especially the upper troposphere should be dominated by ice saturation year round. But humidity is usually recorded in RH_{water}. This study utilizes therefore the formulas for ice and water saturation given in [Hyland und Wexler, 1983] to give a combined relative humidity RH_{merged}. The merging point is set to $-35\,°C$ as recommended by [Anderson, 1995], even though ice nucleation in the lower atmosphere has already been observed to start at temperatures lower than $-15\,°C$ according to [Curry u. a., 1995]. The merged monthly mean relative humidity over the entire measurement period (figure 17) as determined with the corrected radiosonde
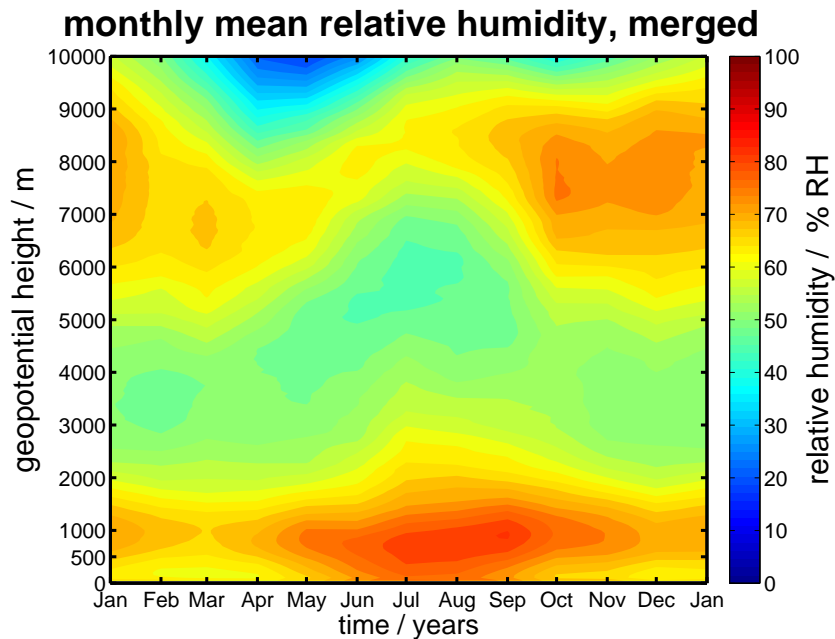

Figure 17: Monthly mean of RH_{ice} & RH_{water} merged at $-35\,°C$ calculated from radiosonde data (1991 to present)

profiles looks somewhat unusual. The vertical humidity distribution is divided into three parts during the year. A high humidity, water dominated section extends from the surface up to roughly 2 km during the cold months and up to 3 km in the summer. The mean RH values in this lowest section extend from about 70 % in winter and in the transitions seasons with a minimum in March to a maximum of approximately 80 % in summer.

Above this humid layer extends an under-saturated section up to 5.5 km in fall and in winter with relative humidity around 50 %. This section's top height with the onset of spring from 5 km in March to a maximum 8 km in July and is back at the winter altitudes in October.

The third vertical section is dominated by ice saturation with RH values from 65 % to 80 %. It extends from 5.5 km to 9 km, but shrinks during the months May, June and July to a thickness of less than 1 km compared to roughly 3 km in the other months. Another markedly feature is the strong decrease in humidity in the upper troposphere during spring. Here the mean tropopause height, defined via humidity readings, seems to be low with a minimum of 9 km in April.

The monthly mean temperatures for the said period are displayed in figure 18. The temperature contours at different altitudes share the same features. The maximum temperatures occur during summer with approximately 5 °C at the surface, −20 °C in 5 km and −50 °C around 9 km. The temperature minimum occurs during winter with −15 °C at the surface, −35 °C in 5 km and roughly −60 °C in the upper troposphere. Thus the imprint of polar day and polar night conditions is clearly visible in the warm and cold half of the year.

 Another interesting quantity besides temperature and relative humidity is the absolute amount of water vapor present in the air. For this purpose figure 19
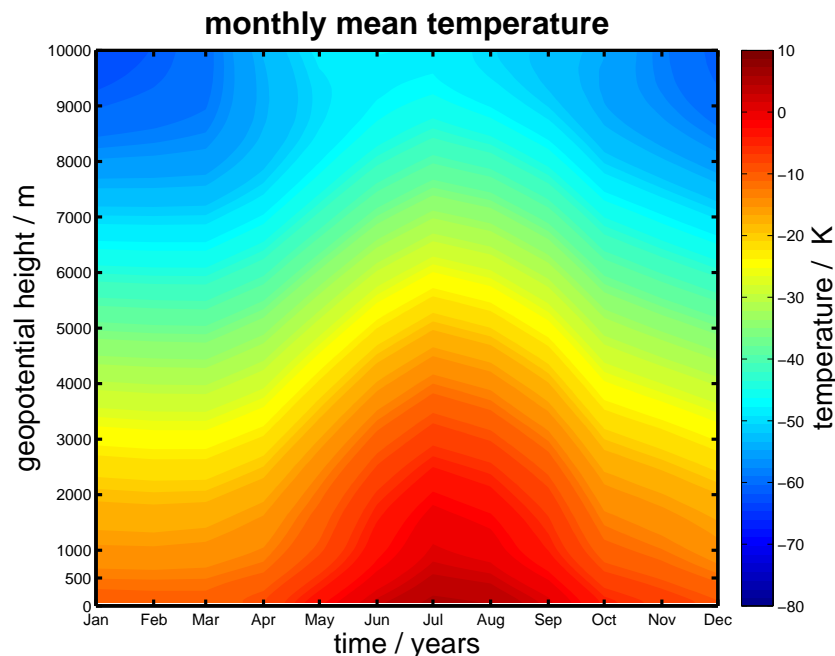

Figure 18: Monthly mean of temperature profiles obtained by radiosoundings (1991 to present)
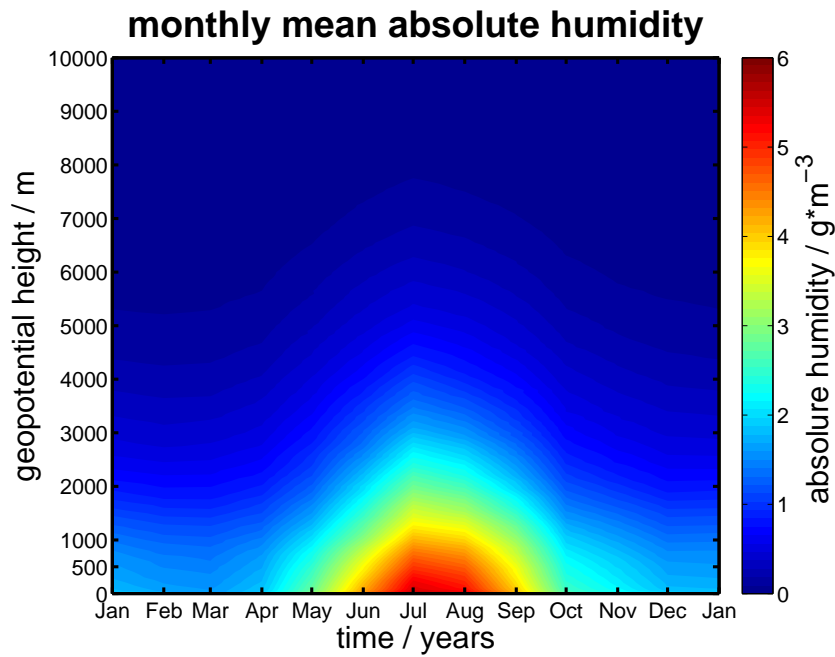
Figure 19: Monthly mean of absolute humidity calculated from radiasonde data (1991 to present)

displays the average contours of absolute humidity determined from the radiosoundings. The observations show that the absolute humidity AH resembles the temperature characteristics with a surface maximum of $5.5\,\mathrm{g\,m^{-3}}$ occurring in July and surface minimum of $2\,\mathrm{g\,m^{-3}}$ in February and March. The AH decreases fast with increasing altitude, roughly halving its value every $2000\,\mathrm{m}$, so that at altitudes above $6\,\mathrm{km}$ $AH \ll 1\,\mathrm{g\,m^{-3}}$.

3.1.2 *Monthly characteristics*

In order to provide a closer look on the monthly differences in temperature, relative and absolute humidity the same data used for the contours above is now displayed in the following line plots (figures 20;21;22).

The temperature plot (figure 20) resembles the on and off switching of short-wave radiation. Starting at the coldest month during polar night, February (blue dashed), the next month, March (green solid), already shows a slight increase in temperatures near the tropopause, because short-wave radiation has been switched on. Now temperatures rise during spring. The increase slows down with the beginning of summer in June but continues until the maximum temperatures are reached in July. August is the first month with decreasing temperatures. In the September profile the temperature decrease is more rapid, as seen by the curvature of the profile in the upper troposphere. With the vanishing sunlight the temperatures decrease throughout the troposphere until reaching their minimum again. The temperature range of approximately $20\,^{\circ}\mathrm{C}$ is constant throughout the vertical profile. One can therefore state that the temperature cycle is driven by the solar cycle.

characteristic temperature profiles, monthly
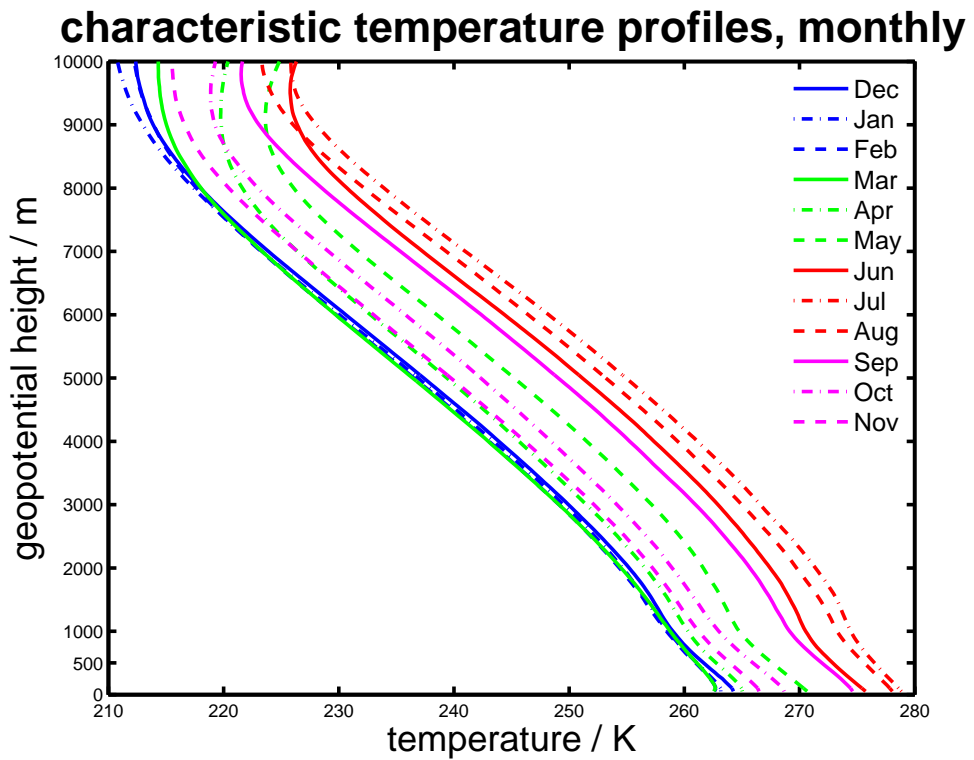
Figure 20: Monthly mean temperature profiles derived from the radiosonde data (1991 to present)
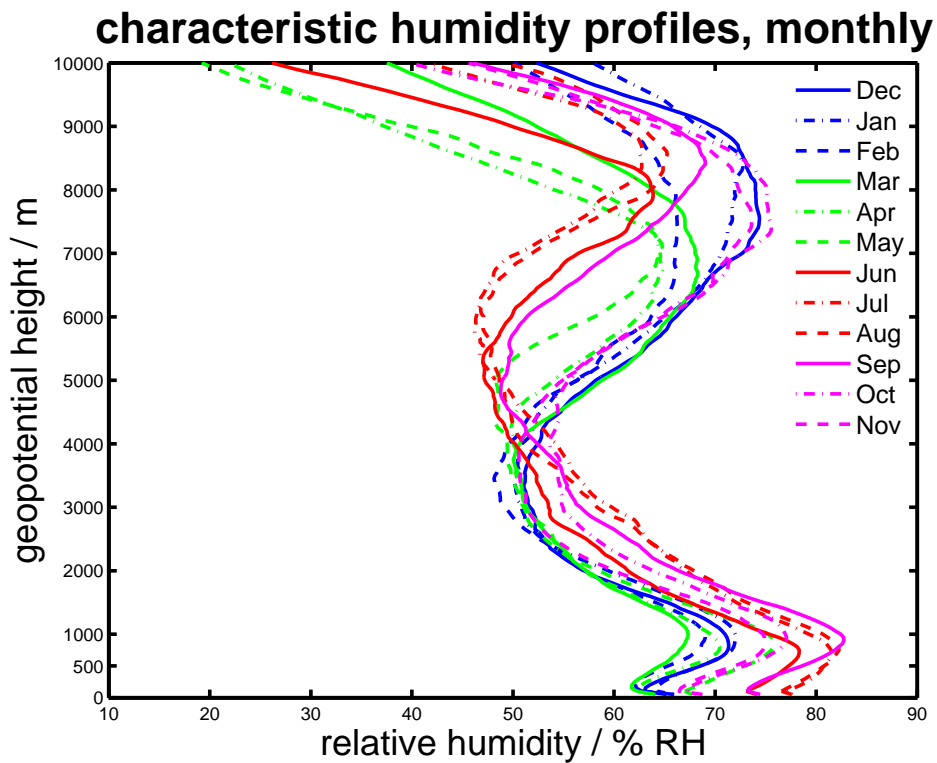
characteristic humidity profiles, monthly

Figure 21: Monthly mean RH profiles for every month derived from the radiosonde data (1991 to present)

The relative humidity figure 21 shows characteristics as follows. The lower part shows a cycle similar to that of the temperature profiles, with the surface minimum around 60 %RH in March and the maximum around 73 %RH in August. Note that the RH inversion between 800 m and 1200 m is present throughout the year. This inversion is an orographic feature. Air masses are lifted upwards at the mountains, forcing condensation. The lifting process effectively dries rising air parcels which can be seen at the minimum RH in the transition zone. Its value differs only little over the year with a maximum of 50 %RH in winter and a minimum of 47 %RH in summer. The position however shifts from 3 km in December to 6.5 km in July. The shift must be temperature driven, because it experiences the same cycle as the temperature. In the third ice dominated part of the profiles change must be driven by several factors, the temperature being only one of them. Here, the first thing one notices is that maximum and minimum RH have roughly the same magnitude as the lower parts. However the maximum belongs to the winter season and the minimum to the summer. Another aspect is the markedly decrease in RH from winter to spring with the onset of solar radiation and the increase in fall with the beginning of polar night.

Finally the annual cycle of absolute humidity AH (figure 22) shows as expected from figure 19 a the same seasonal cycle as the temperature profiles. The minimum of $1.7\,\mathrm{g\,m^{-3}}$ is reached in February and March and the maximum of $5.5\,\mathrm{g\,m^{-3}}$ in the warmest months July and August. All profiles show a rapid decrease in AH with height. At 2000 m all profiles show only half the amount of moisture compared to surface, which underlines the characteristic already
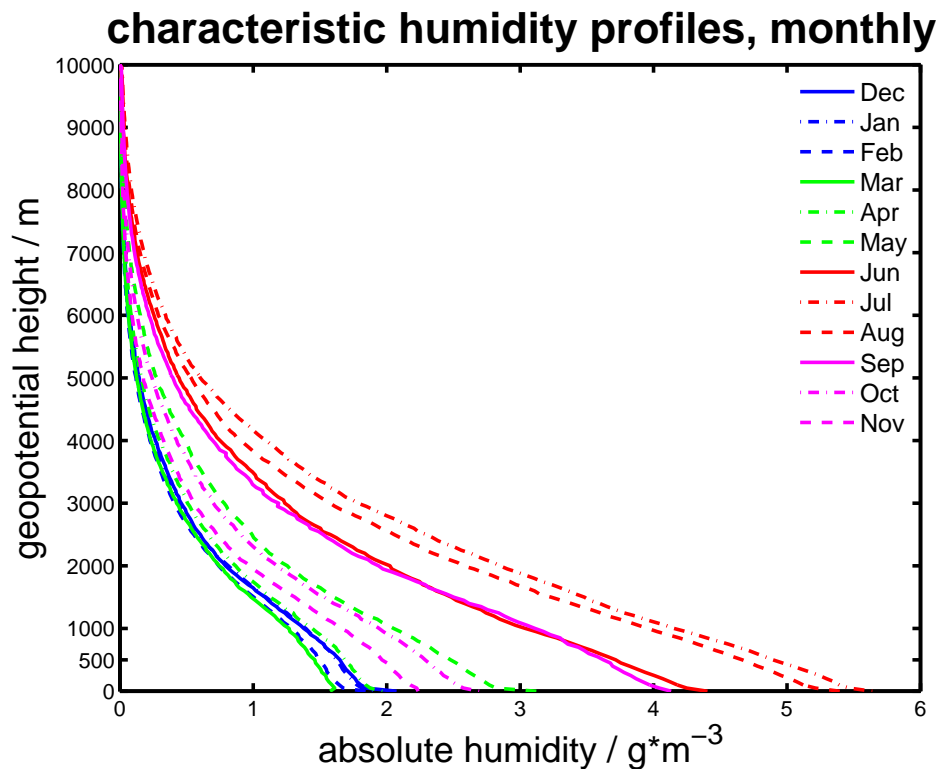

Figure 22: Mean absolute humidity profiles for every month derived from the radiosonde data

illustrated by figure 19. So the decrease is more rapid for higher initial values of AH and for higher temperatures.

3.1.3 *Relation of relative humidity, absolute humidity and temperature*

Looking at the monthly change in RH the question arises why its value drops in the upper troposphere so dramatically in the transitions from winter to spring with increasing temperatures. Note that the absolute humidity content changes little during the transition period, so the water content is approximately constant. Using this basic assumption and starting with the ideal gas law for the partial pressure of water vapor e_w:

$$e_w V_w = n_w RT, \tag{21}$$

where V_w is the volume of water, R the ideal gas constant, T the temperature and n_w the amount of water in mol. Solving for e_w and replacing n_w by the ratio of mass and molar mass m_w/M_w gives:

$$e_w = \frac{m_w RT}{V_w M_w}. \tag{22}$$

Defining the specific gas constant for water $R_w = 461.525\,\mathrm{K}^{-1}\mathrm{kg}^{-1}$ and absolute humidity as the density of water vapor $= \rho_w = m_w/V_w$ this can written as:

$$e_w = \rho_w R_w T. \tag{23}$$

The partial pressure can be calculated using RH and the saturation vapor pressure $E_s(T)$ this gives an expression for RH as a function of temperature and water content.

$$RH = \frac{\rho_w R_w T}{E_s}. \tag{24}$$

Equation 24 is valid for every T and ρ_w. In order to estimate the change of RH to an increase in T it seem convenient to calculate the difference in relative humidity $\Delta RH = RH - RH'$ normalized with the initial RH.s

$$\frac{\Delta RH}{RH} = \frac{\rho_w R_w T/E_s - \rho'_w R_w T'/E'_s}{\rho_w R_w T/E_s}. \tag{25}$$

Now using $\rho'_w \approx \rho_w$ simplifies the term on the right hand sight.

$$\frac{\Delta RH}{RH} = 1 - \frac{T' \cdot E_s}{E'_s \cdot T}. \tag{26}$$

Replacing T' by $T + \Delta T$ yields after some simplification.

$$\frac{\Delta RH}{RH} = 1 - \frac{E_s(T)}{E_s(T + \Delta T)} \left(1 - \frac{\Delta T}{T}\right). \tag{27}$$

Because ΔT is positive and smaller than T and because the saturation vapor pressure increases exponentially with temperature, the second term on the right hand is always positive and < 1. Therefore defining

$$x(\Delta T, T) = \frac{E_s(T)}{E_s(T + \Delta T)} \left(1 - \frac{\Delta T}{T}\right). \tag{28}$$

With this definition the relative humidity after an increase in temperature can finally be estimated as

$$RH' = x(\Delta T, T) \cdot RH. \tag{29}$$

Since $x(\Delta T, T) < 1$ RH' will be smaller than RH. This relation works also for temperature decrease. Thus this simple calculation explains the response of relative humidity to temperature changes under the assumption that the ambient absolute humidity remains approximately constant $\rho_w \approx \rho'_w$.

3.1.4 *Orographic characteristics*

A persistent and already mentioned orographic feature in all humidity plots is the markedly increase in RH around the mountains. The question remains, if there is any horizontal characteristic associated with measurement site. This is done by utilizing the wind directions recorded by the radiosonde. Because the sonde can drift significantly even in the troposphere, only the lowest layers up to the mountain tops are considered. Neglecting the wind speed, the focus is on the direction. Thus a reasonable approach is a polar plot similar to a wind rose but with the quantities temperature, relative humidity and absolute humidity. These plots are created for two different height slabs, one from 0 m to 400 m and the other from 800 m to 1200 m. Here only the winter is presented, corresponding plots for the summer season can be found in the Appendix.
The temperature rose plots seen in figure 23 state that the near surface temperatures (a) are maximal in the South, where mountains are close by. When looking at the next height level (b) this southern maximum becomes more distinct. Mainly because the air mass coming from Northeast is more likely to have passed the land mass and the glaciers. The higher temperature in South and Southwest is not necessarily a consequence of the vertical mountain structure. The higher temperatures may also originate from the warmer open water which towards the Southwest, such as the West Spitsbergen Current.
Next, looking at the relative humidity, figure 24, the markedly features in the lowest part (a) are the high RH values towards Southwest, in direction where the mountains are closest. As expected from the humidity profiles, the highest readings are in level (b) around the mountain top. Here the maximum is located towards Southwest away from the glacier side and towards the open water.
 Investigating the absolute humidity (figure 53), one observes the same features as for temperature and relative humidity. Higher values of AH are associated with directions towards the open water and the nearest mountain top and small values are detected towards the landmass.
Summarizing, the orography of Ny-Ålesund affects the lower troposphere by creating high RH values through the lifting of air masses and enhances condensation at the mountains, i.e. for cloud formation above the mountains is only little moisture available. This may explain why the previously defined intermediate sector (figure 17) is constantly under-saturated. It also shows that the orography's influence extends to higher altitudes in summer, because the humid sector extends upwards in the summer months, see figure 17.
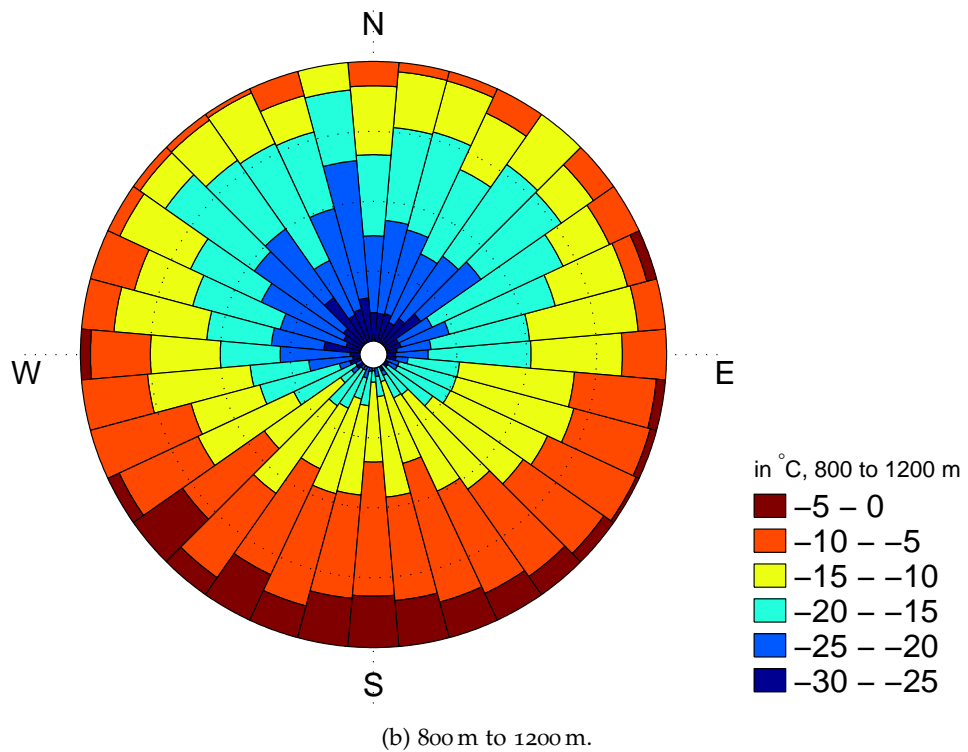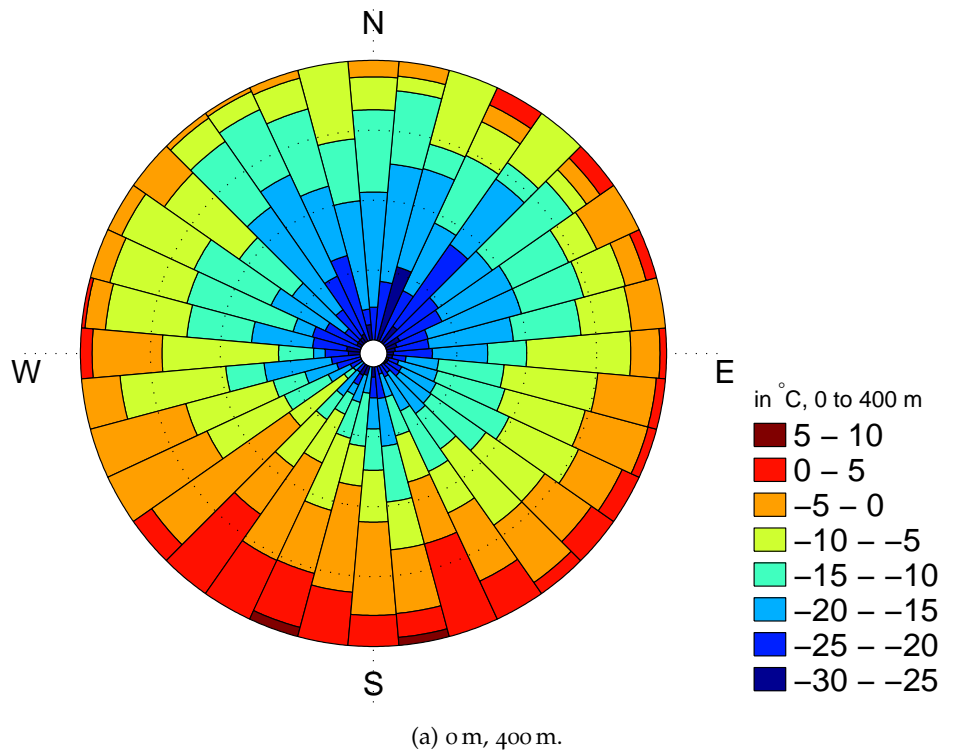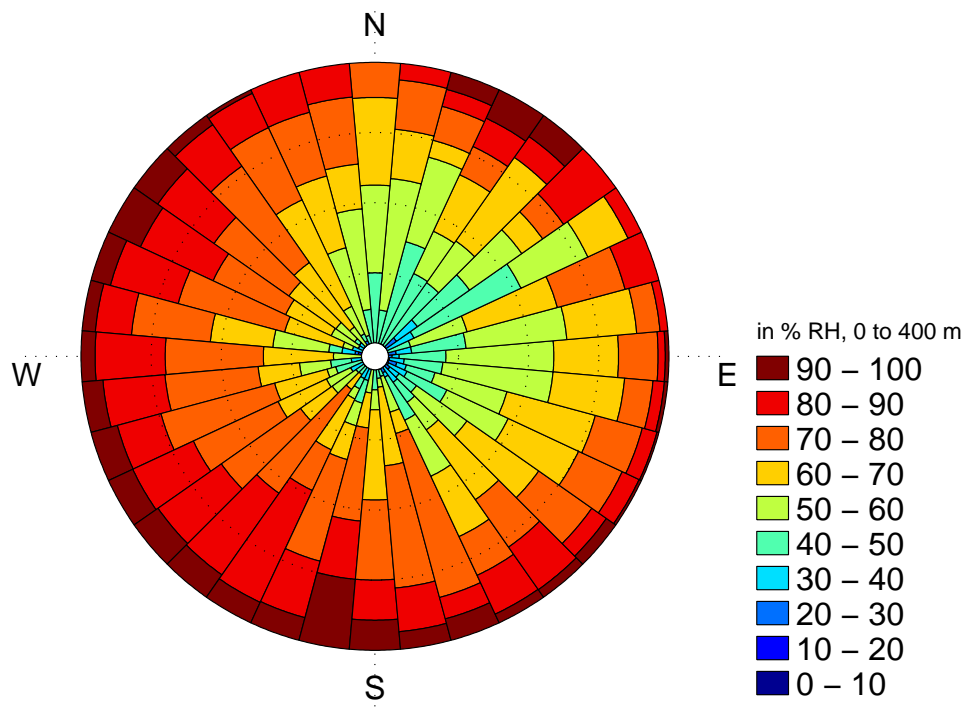
(a) 0 m, 400 m.
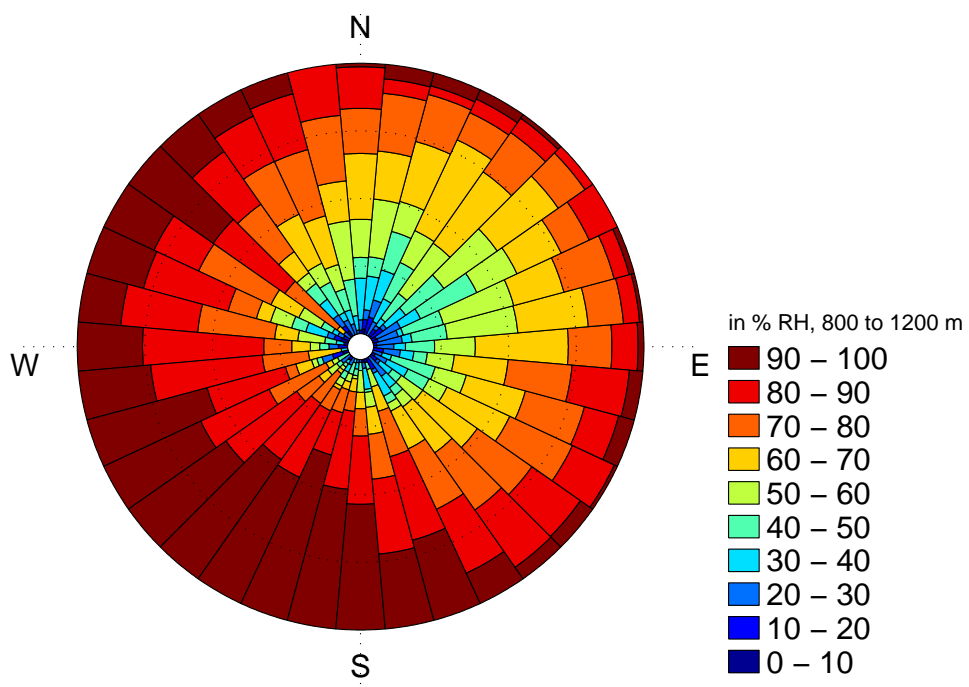

(b) 800 m to 1200 m.

Figure 23: Temperature rose for the winter obtained from radiosoundings (1991 to present).
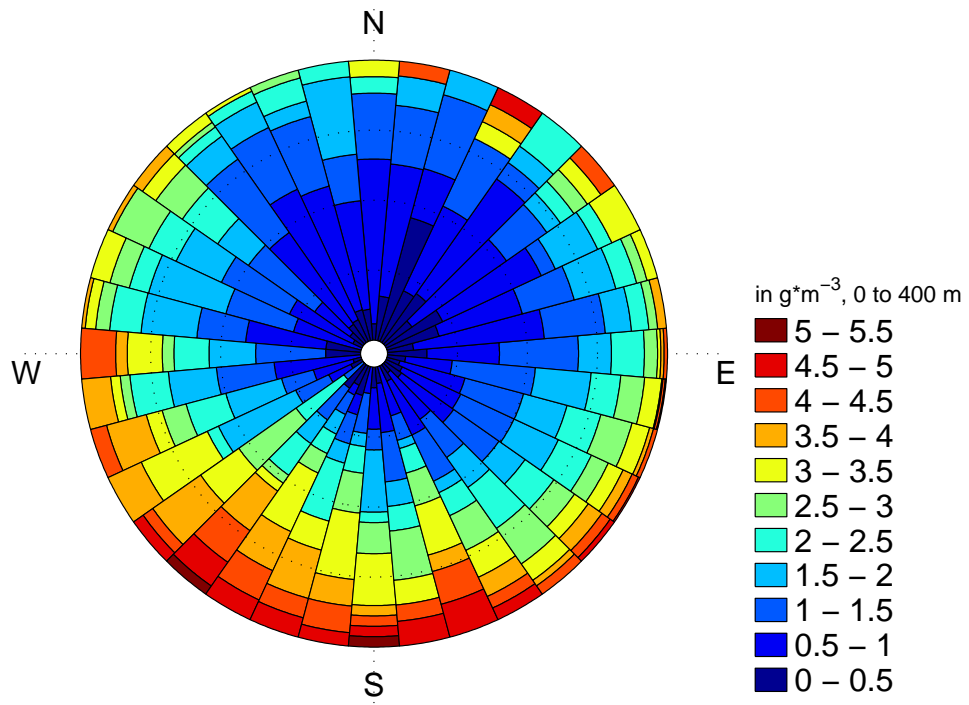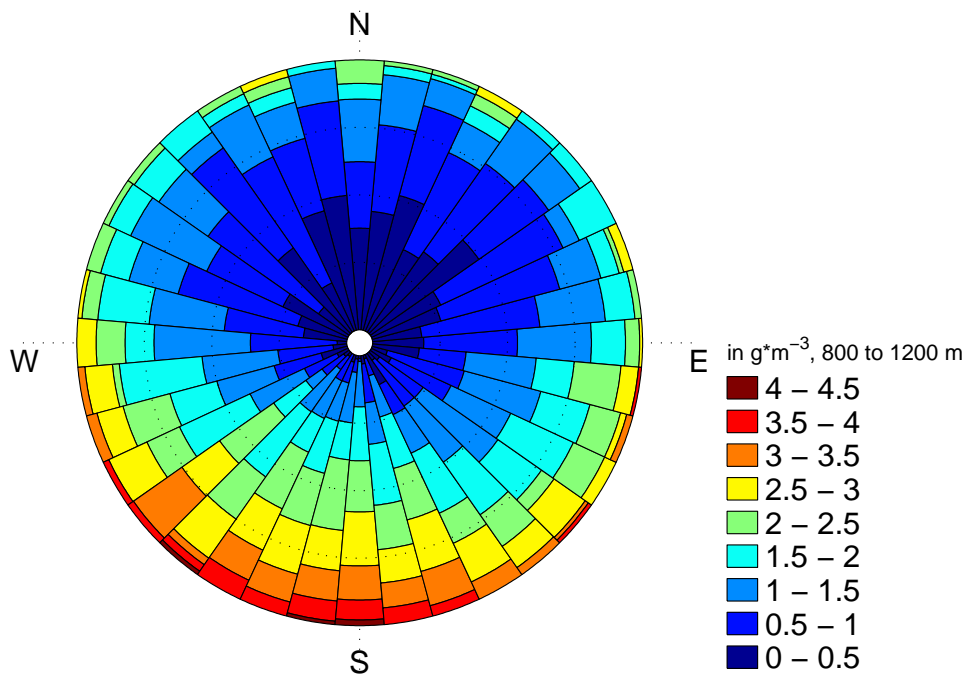
(a) 0 m, 400 m.

(b) 800 m to 1200 m.

Figure 24: Relative humidity roses for the winter obtained from radiosoundings (1991 to present).

(a) 0 m, 400 m.

(b) 800 m to 1200 m.

Figure 25: Absolute humidity roses for the winter (1991 to present).

CHANGES IN THE TROPOSPHERIC WATER CONTENT

This chapter is concerned with identifying changes in the vertical humidity structure over the measurement period from 1991 to present, therefor using the corrected humidity record as well the radiosonde temperature as a basis.

4.1 CHANGES IN TEMPERATURE AND HUMIDITY

A quick look at the monthly mean temperature profiles shows that more warm winters have occurred during the last decade than the earlier one (figure 26), e. g. in 2006, 2012 and 2014. But RH should stay the same when the temperature increases, because partial pressure and saturation vapor pressure should increase at the same rate. However a rise in temperature during the cold season could influence RH for example in changing the open water surface surrounding the measurement site. The amount of open water presents determines the maximum of water vapor that can evaporate. If this vapor is advected towards Ny-Ålesund the radiosonde would see a potential increase in RH now that the condensable vapor content is increased. Another explanation for rising humidity may be is the influence of temperature on ice saturation. As mentioned earlier the moisture during the yearly cold period is dominated by ice saturation. This limits the maximum RH_{water} detectable. Increasing temperature effectively increases the maximum RH_{water}. The monthly mean of absolute humidity as a measure of total water vapor content supports the last argument,
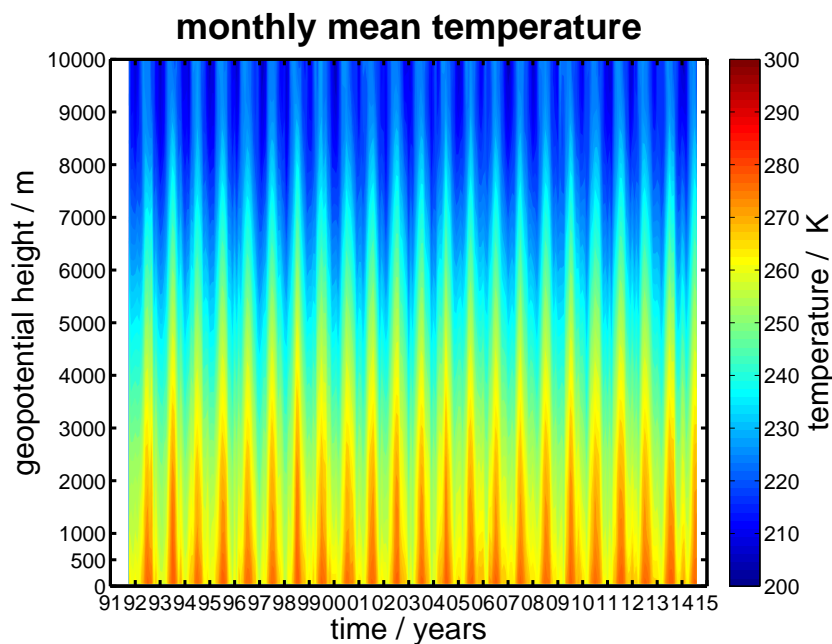

Figure 26: Monthly mean temperature derived from the radiosonde data (1991 to present)
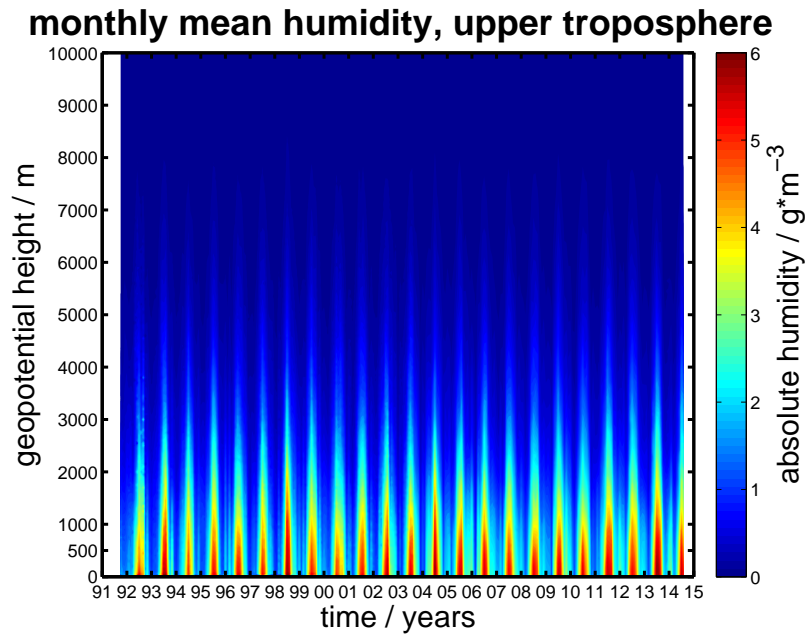
monthly mean humidity, upper troposphere

Figure 27: Absolute humidity derived from the radiosonde data (1991 to present)

figure 27. Even though the contour plot can be misleading, the total water content in the upper troposphere changes little from winter to winter. A closer look on the monthly changes is necessary to characterize changes.

Because previous studies [Maturilli u. a., 2014] show the greatest temperature increase in winter and to shorten the discussion on seasonal changes, only the winter period is considered in this section. A winter for a given year is defined as the December of the previous year plus the months January and February of the year of interest. The winter mean RH values are shown in figure 28. Again the three tropospheric humidity sections are seen. The upper humid layer decreases in thickness and amplitude over the measurement period. This decrease is accompanied by an increase in the lower level humidity. One might argue, that this change has no climatological origin, but is caused by switching radiosonde types. In favor of the climatological change is the onset of the strong decrease in the upper RH layer during the winter of 2005, more than one year after the switch from RS80 to RS90. Against climatological reasons speaks the lower level increase in RH, whose onset starts in the winter period of 2003. In order to clarify this aspect the corresponding winter temperatures are investigated (figure 29).

The temperature underlines the climatological cause. The RH increase in the lower troposphere appears to coincide with the temperature increases in 2005 and the minimum temperatures in 2003 coincide with a humidity decrease. The temperature increases is observed in the entire atmospheric column. Recalling the previous chapter, where an increase in temperature in the upper troposphere was proofed (equation 29)to reduce RH values as long as the moisture content change is small, the decrease in the 2005 winter RH values can be explained by looking at figure 30.

Even though the moisture content increases, the increase in small compared to the previous years. Therefore one can conclude that the decrease in RH in the upper section can be explained with the temperature increase.

monthly mean relative humidity, DJF
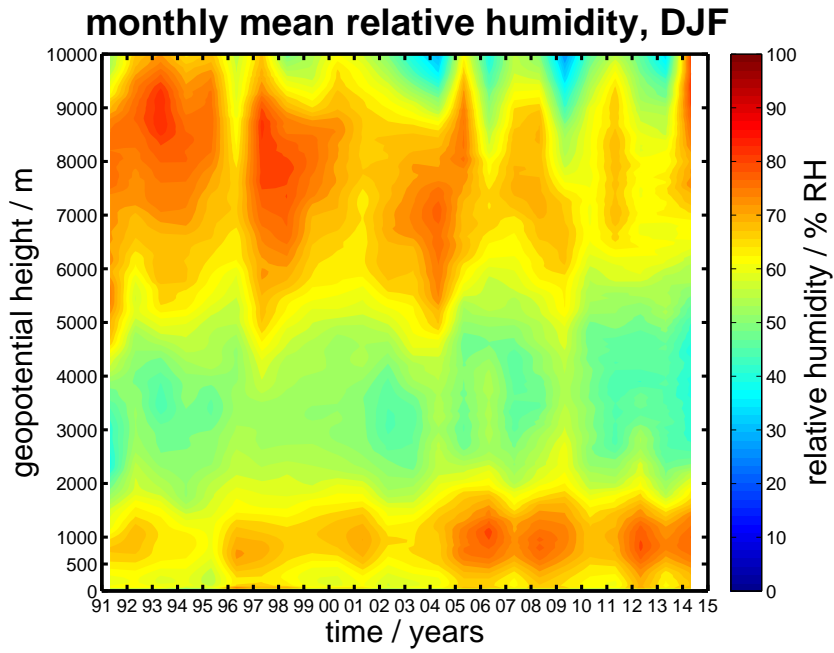
Figure 28: Merged RH contour for the winter periods derived from the radiosonde data (1991 to present)
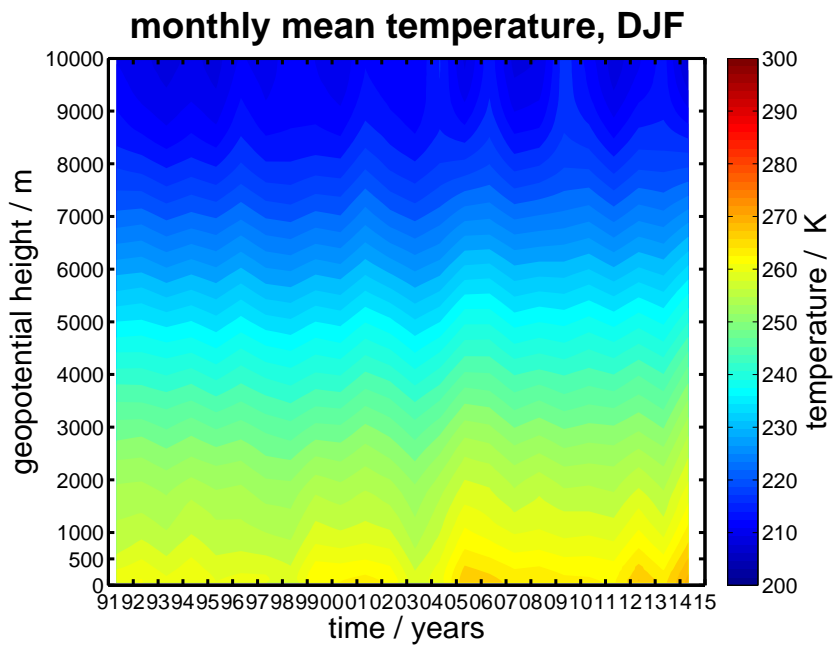
monthly mean temperature, DJF

Figure 29: Temperature contour for the winter periods derived from the radiosonde data (1991 to present)
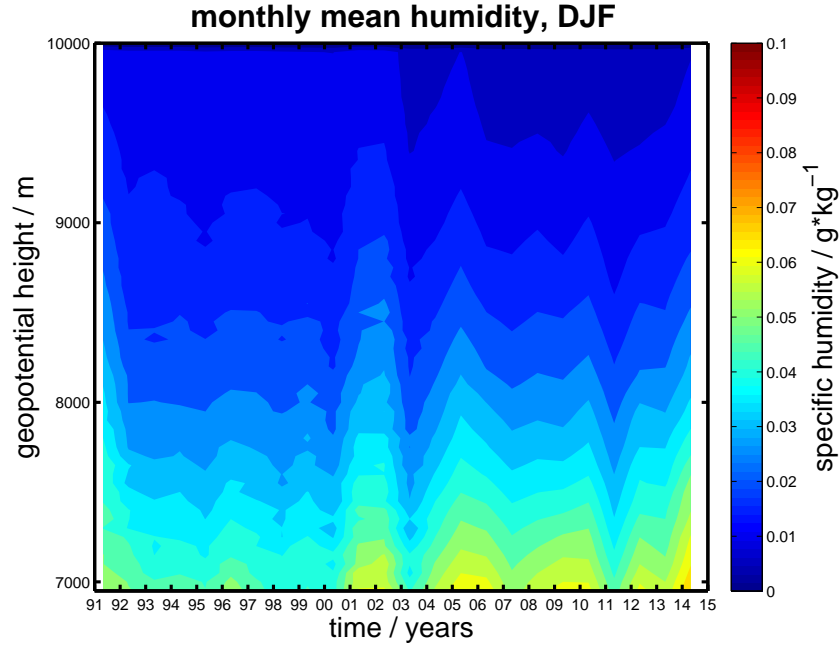
Figure 30: Specific humidity contour for winter period derived from the radiosonde data (1991 to present)

4.2 ANALYSIS OF INTEGRATED WATER VAPOR

The first step in estimating the effect of water vapor and clouds on the radiation and temperature budgets is quantifying the total amount of water vapor in the atmosphere. If no change in water content is observed, its role in Arctic Amplification could be neglected. This section is concerned with estimating the change in tropospheric water content through a time-series analysis. The analysis focuses on pointing out long-term changes in seasonal percentiles.

4.2.1 *Calculating integrated water vapor*

The water vapor content, here expressed as integrated water vapor IWV in $kg\,m^{-2}$, is determined with the help of the recorded profiles of temperature, height and corrected humidity according to [Liu u. a., 2000] from basic equations. The total amount of tropospheric water vapor in a column is calculated by integrating the absolute humidity from zero to the tropopause height. Because the absolute humidity in the upper troposhere is very low, a column is defined from the surface to 10 km. Starting with the ideal gas law written in form 24 and solved for ρ_w

$$\rho_w = \frac{RH \cdot E_s}{R_w \cdot T} \tag{30}$$

the integral must be expressed numerically

$$IWV = \int_{surface}^{10\,km} \rho_w(h) \cdot dh = \sum_{i}^{N-1} \frac{\rho_w^i + \rho_w^{i+1}}{2} \cdot \left(h^{i+1} - h^i\right). \tag{31}$$

Here N denotes the number of height bins, each identified via the index i. With the help of equation 31 the amount of water vapor in a column is estimated.

Note the the column looks more like a tube, because the radiosonde experiences wind drift while ascending.

4.2.2 *Time-series analysis*

Calculating the IWV for each sounding it is possible to characterize the change in water vapor content over the period from 1991 to present. The data is then fitted to determine the tendency of change. Technically this change cannot be called a trend because the period is smaller than 30 years. The tendency is estimated via first calculating the IWV anomalies by subtracting the the monthly average for all years from the individual month. The seasonality is calculated via a Loess-running mean, because the data is not evenly spaced. The result is presented in figure 31.The analysis shows a shockingly large trend of $0.41\,\mathrm{kg\,m^{-2}}$. However the uncertainty is very large. The seasonal characteristic illustrates that most this increase originates from the winter months, seen at the high minimum values especially during the recent years.
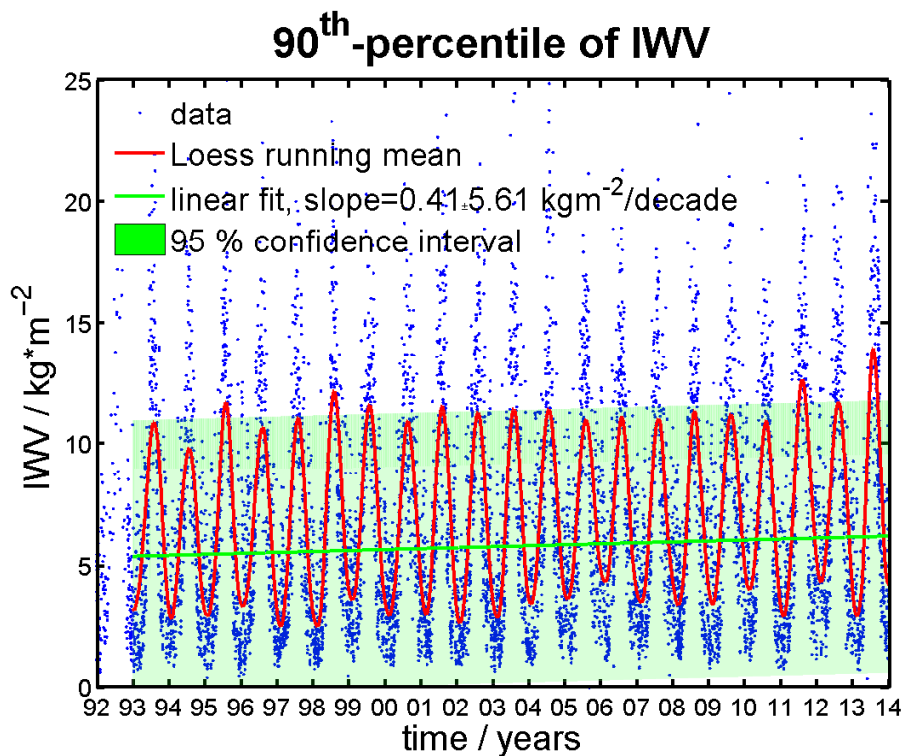

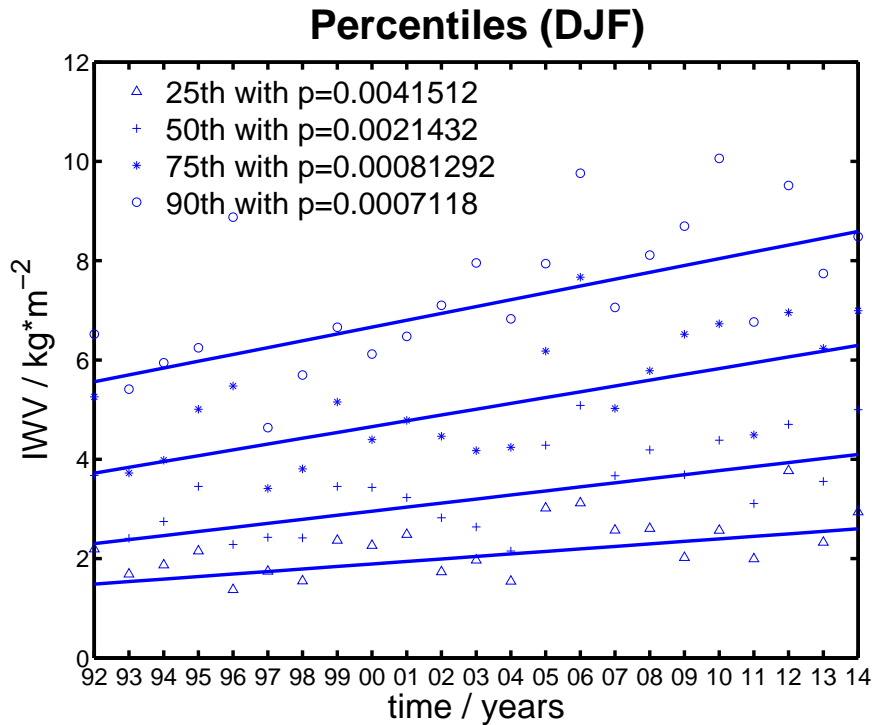Figure 31: Time-series of integrated water vapor.

Figure 32: Percentiles for winter derived from the radiosonde data (1991 to present).

4.2.3 *Seasonality of changes in percentiles*

In order to investigate this change further this study chooses a percentile analysis. This approach attempts to identify weather the overall moisture has increased or just the number of days with high water content. The percentiles of interest are the 25th, 50th, 75th and the 90th. As before the data is fitted with a linear model and the p-value of the trend is calculated through a standard student t-test. The result are presented in figures 32, 34, 35 and 36. During winter all the percentiles show a significant increase, indicated by the small p-values. The increase in all percentiles illustrates a rise in total I*WV*. Higher percentiles have a larger increase, e. g. the 90th percentile has increased almost $1\,kg\,m^{-2}$ per decade. A detailed fit for the 90th-percentile is shown in figure 33. Even though the uncertainty is large, the increaseof $1.3\,kg\,m^{-2}$ per decade is markedly high. Assuming the average winter I*WV* at $8\,kg\,m^{-2}$ this means an increase of 11 % every 10 years. In the spring time no significant change is observed. The data shows a large scatter. The same can be said about the summer. No significant changes are observable. Note that the summer I*WV* is roughly double of the winter values. The fall looks more like the winter. Again the greater percentile show a larger increase. The tendencies are all significant except for the lowest percentile.

What can be inferred from the observed increase. First, Arctic Amplification can also be observed in the moisture content. Second the increase in I*WV* is enhanced during the winter time and in fall. If water vapor feedback plays an important role in Arctic Amplification it can best be observed these seasons.
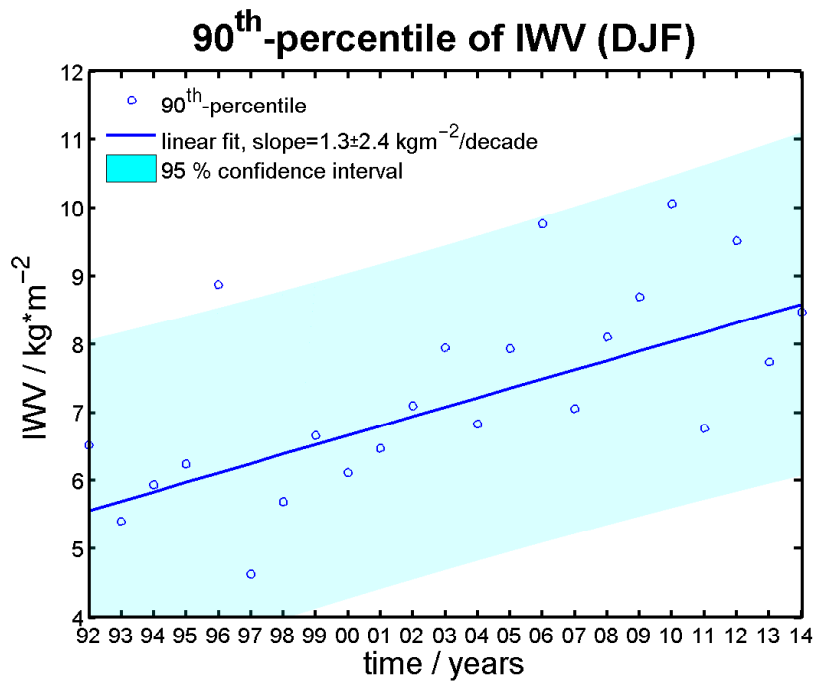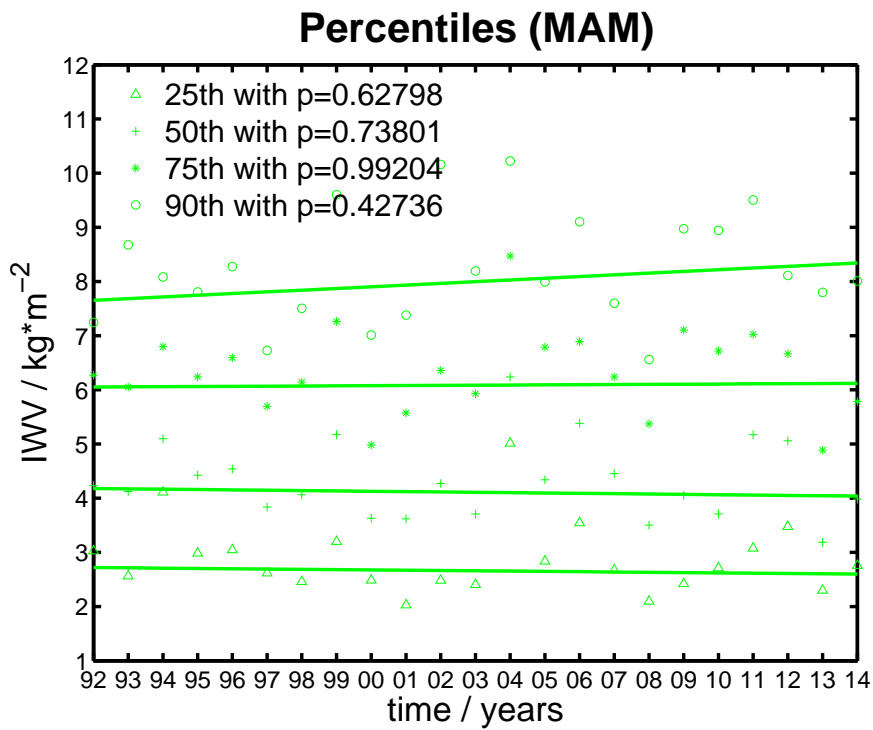
Figure 33: Fit of 90th-percentile.
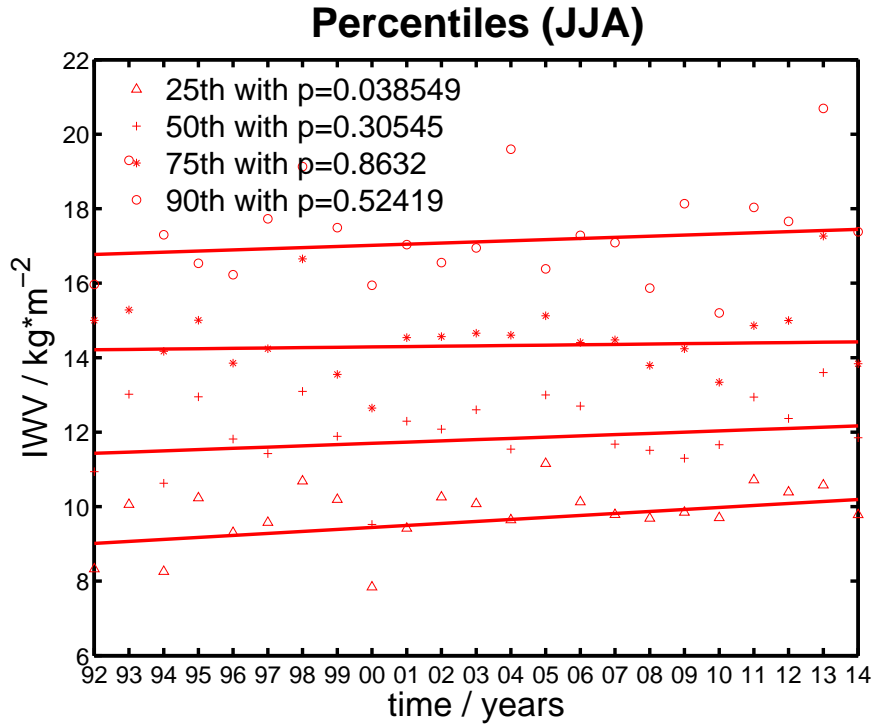

Figure 34: Percentiles for spring.

Figure 35: Percentiles for summer.
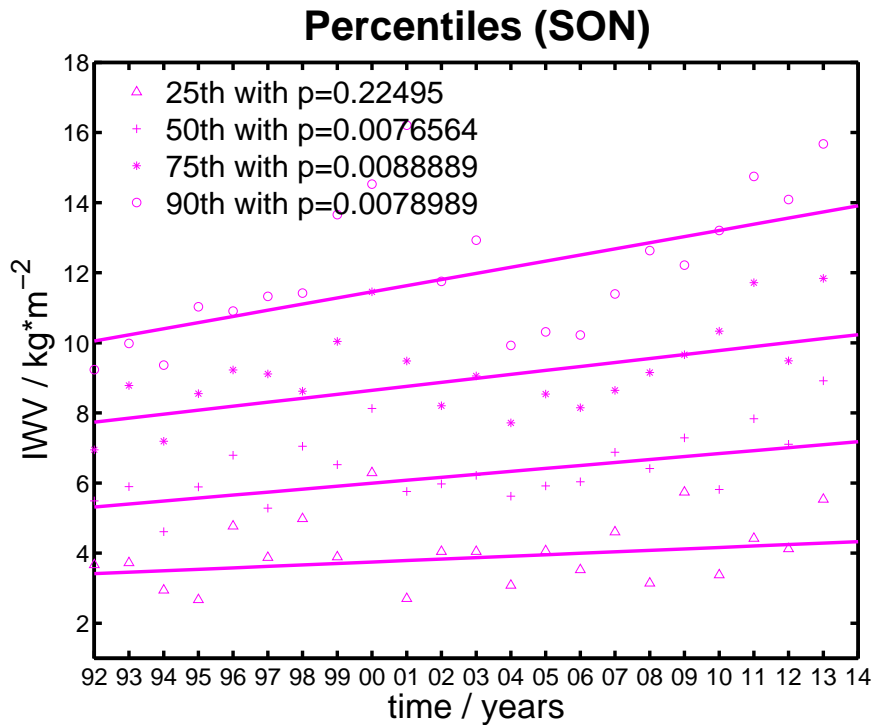
Figure 36: Percentiles for fall.

Ending this chapter the study investigates the correlation of surface temperature, obtained from the BSRN field, and the atmospheric water content. For this purpose the monthly anomalies of the 2 m-temperature and the IWV are calculated. The results are presented as contour plots, showing years and months on the axis. Figures 37 and 38 illustrate the results. The two contours share the same characteristics. A suitable approach to quantify the correlation is calculating the correlation coefficient r_r for every month. The results are presented in table 2.

The correlation during the winter, spring and fall is remarkable. As long as the temperatures are cold enough and solar radiation is not near its peak, the water content follows the surface 2 m-temperature. The question remains whether the increase in IWV is an epiphenomenon of temperature increase or if feedbacks associated with water vapor are strong enough to increase the temperatures further. This leads over to the next chapter, where the cloud distribution over new Ny-Ålesund is characterized.

Month	JAN	FEB	MAR	APR	MAY	JUN	JUL	AUG	SEP	OCT	NOV	DEC
r_c	0.84	0.83	0.92	0.92	0.66	0.64	0.22	0.72	0.87	0.91	0.92	0.91

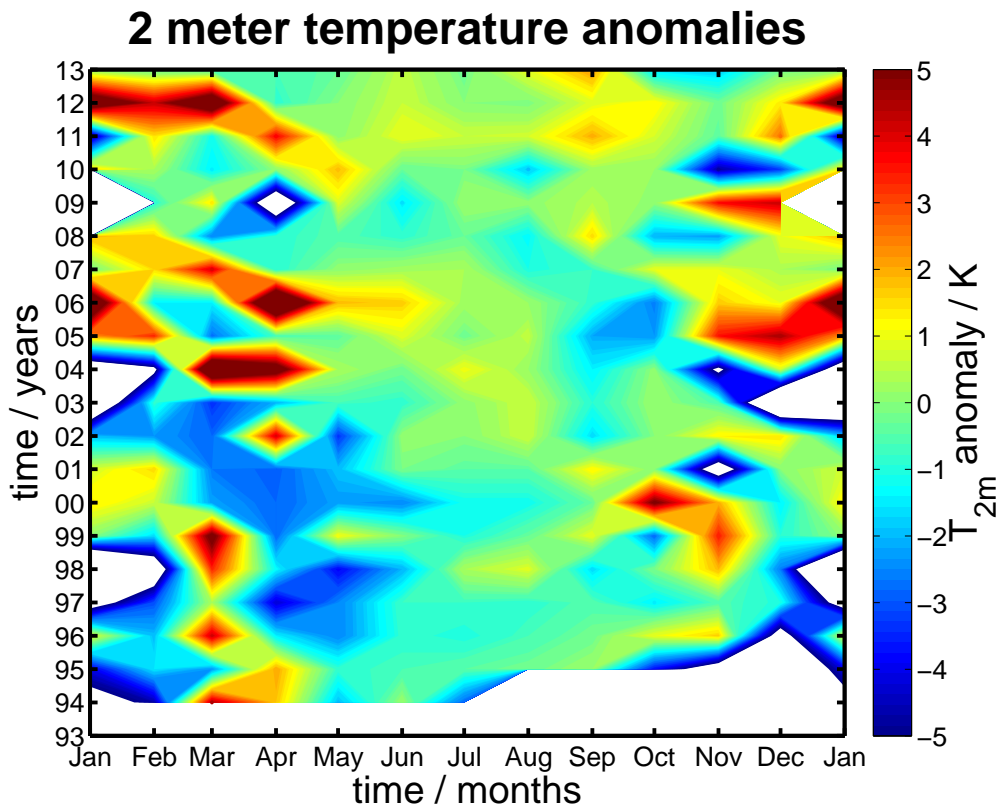Table 2: Correlations between IWV and T_{2m} derived using radisonde and BSRN data.

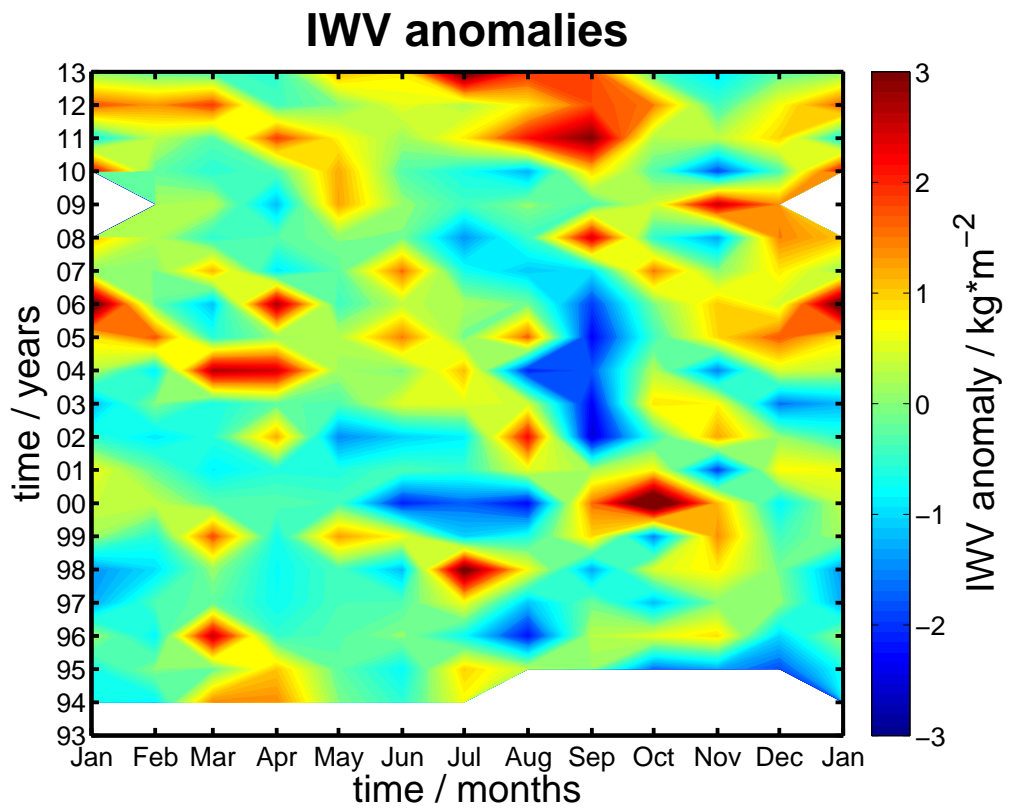Figure 37: Monthly 2 m-temperature anomalies.

Figure 38: Monthly IWV anomalies.

CLOUDS AND RADIATION

This section deals with the vertical and temporal distribution of clouds at the measurement site. The previous section showed that the water vapor content is closely related to the temperature increase. In order to investigate the possible effect of clouds on temperature, any change in cloud characteristics should be quantified first.

5.1 MEASUREMENT INSTRUMENTS

At the AWIPEV station clouds are observed with a ceilometer. This instrument uses the LIDAR (LIght Detection And Ranging) principle to detect the cloud base height (CBH). The current ceilometer is able to detect up to three cloud base heights and their thickness as long as the lowest registered cloud is thin. The measurement principle introduces a bias in cloud occurrence in favor of low cloud base heights. Due to instrumental changes in 1998 and again 2011 (current instrument Vaisala CL51) the individual instrument performance introduces additional bias due to different altitude resolution and retrieval algorithms. This introduces visible inhomogeneities in the data series. Corrections for these biases are not possible. Thus for this study only the lowest cloud base height is used, which is recorded in the BSRN data.
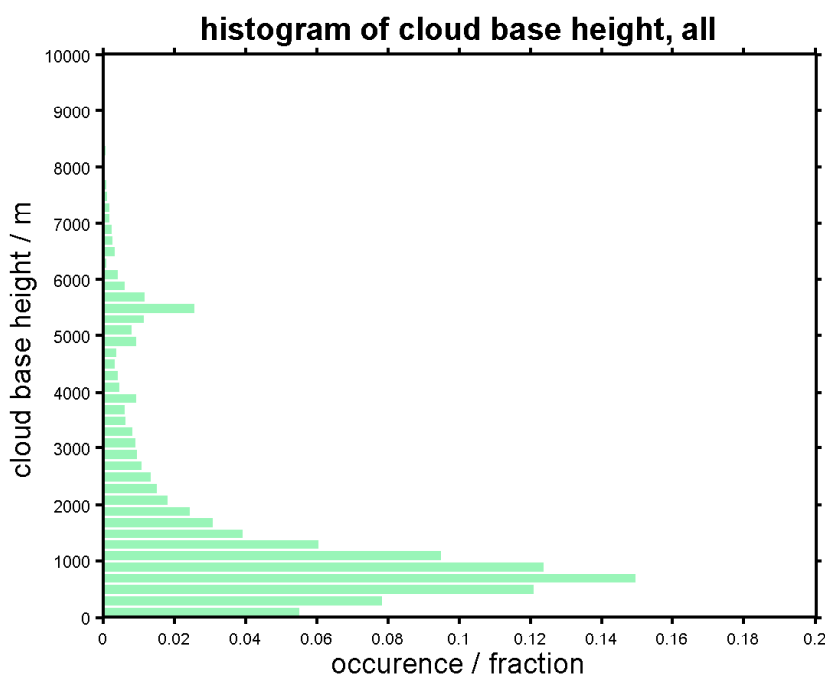

Figure 39: Vertical distribution of clouds in the troposphere obtained from ceilometer (1994 to present).

5.2   CLOUD CHARACTERISTICS

5.2.1   *Vertical distribution of cloud base height*

The overall vertical distribution of cloud base height throughout the year is illustrated by figure 39. Two pronounced peaks are visible. The first is located at 1 km above ground, right at the mountain top (14 % occurrence). Thus the peak in the humidity profiles is also present in the cloud distribution. These clouds are probably liquid clouds. The other peak is located at 5.5 km (3 % occurrence). At this altitude the humidity rises above ice saturation and these clouds rather consist of ice particles than liquid water. Probably clouds at this altitude occur more often, but this information is lost due to the stated bias in measurement principle. A third minute peak located at 4 km is probably just noise. In total a little over one third of detected clouds appears at or below the mountain top. the The vertical cloud distribution for the individual seasons differs little from figure 39 and can be found in the appendix.

5.2.2   *Seasonal changes from 1994–present*

The vertical distribution suggest dividing the occurrence count in 5 sections. The first, covering all low clouds up to 500 m, the second around the mountain peak, 500 m to 1300 m, a third just barely covering the small, 1300 m to 4700 m, mid troposphere, one for the second peak, 4700 m to 7300 m, a region for high clouds > 7300 m and one count for the occurrence of clear sky conditions. Investigating the temporal of the vertical distribution over the years is then split into individual season. The winter period is displayed in figure 40. At first, one notices the large change in 1998 introduced by switching instruments Hence, the focus is on the occurrence after 1998. Additionally in 2000 some error must have occurred during this winter. Going from top to bottom, the overall occurrence of clear sky conditions changes little over time and is on average roughly 20 %. The maximum winter clear sky occurrence is found in 2011 with 32 %. This maximum could also be a result of the change of instrument in 2010. Clouds at intermediate and high altitudes occur at the rate from 2001 to 2013. The disappearance of clouds around the second peak in the last to years could be attributed to the new ceilometer. The most interesting in this plot are the low clouds and the clouds around mountain top. They are detected on average with 45 % occurrence. However, their variability in occurrence seems to resemble that of winter humidity and temperature change. Characteristic which are also found in the humidity contour (28) and temperature contour (29)are the minima in 2010 and 2011, and the maxima in 2006, 2007 and in last two years. The question remains who influences whom. Is the cloud distribution just evidence of higher humidity levels or do the clouds influence humidity and temperature.
Next, the same plot is shown for the spring time, figure 41. The spring seems to have a fairly constant distribution of clouds. Low clouds occur approximately 30 % of the time, high clouds with 15 to 20 % and clear sky is detected at a constant rate little over 25 %. The intermediate make up the smallest portion.

change in the occurrence of low and mountain level clouds can be observed. No visible change in the distribution is observed.

 Figure 42 reveals that during the summer months almost 70 % of the detected clouds are located beneath the mountains. Clear sky counts occur with a con-
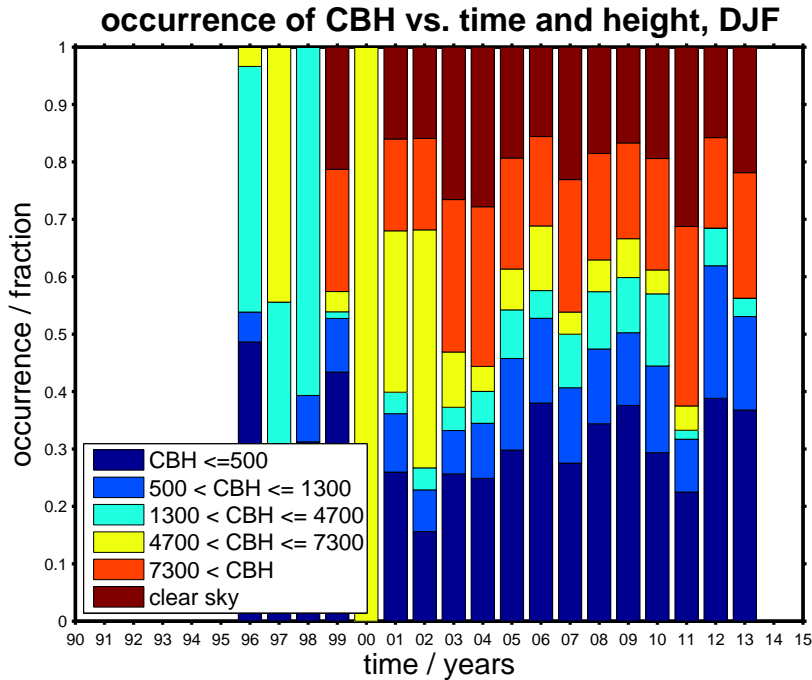

Figure 40: Seasonal vertical cloud distribution in the troposphere from ceilometer, winter (1996 to present).
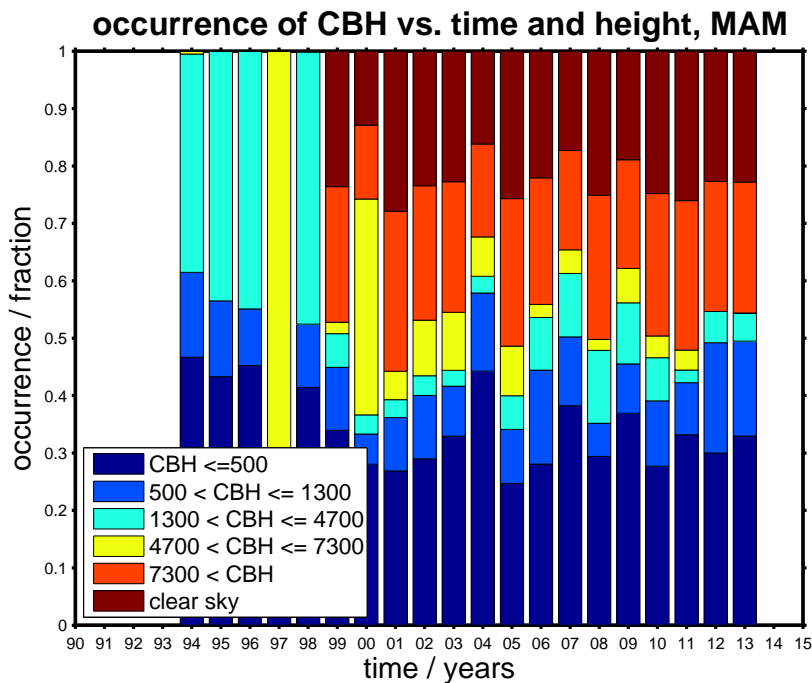

Figure 41: Seasonal vertical cloud distribution in the troposphere from ceilometer, spring (1996 to present).
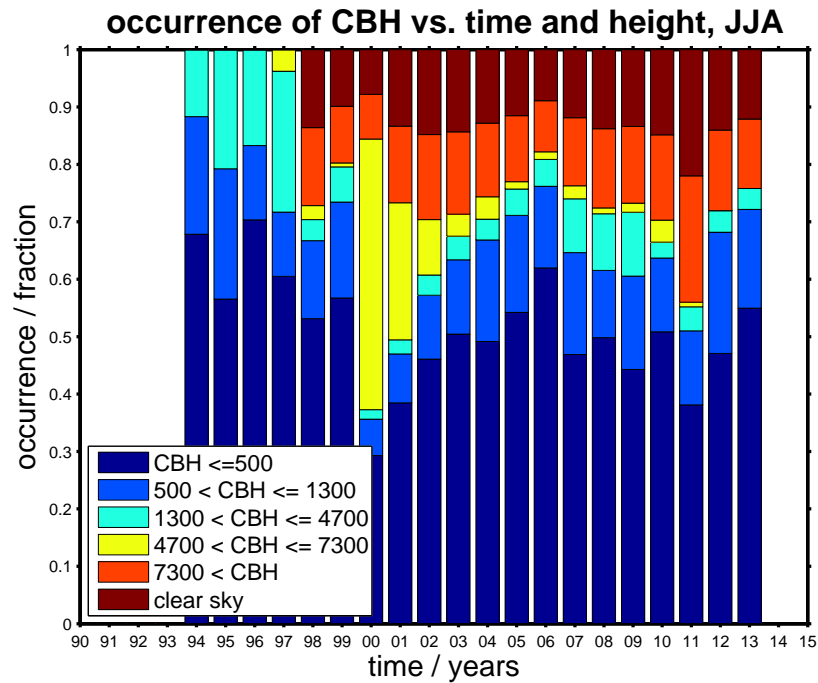
Figure 42: Seasonal vertical cloud distribution in the troposphere from ceilometer, summer (1996 to present).

stant probability of about 10 % which is only half as often as in winter or in spring. The same can be said for high clouds. The only observable change in cloud occurrence takes place from 2000 to 2006. Here the low count cloud starts out at a minimum of only 30 %, but increases rapidly to a maximum of 60 % in 2006. At the same time the occurrence of clouds around the second peak diminishes rapidly from over 40 % to only 2 %. After that their occurrence remains small and are not detected in recent years.

At last the seasonal distribution for fall is observed using figure 43. Fall and spring look quiet alike. Clouds at high altitudes including clear sky counts occur at almost constant rates. Only during the early years 2000 and 2001 is a change from these averages observed. In 2001 the second peak clouds are detected in 40 % of the time. Their occurrence vanishes almost completely up to now. When comparing spring and fall a difference in the detection probability of low clouds and clear sky counts is observed. In fall low clouds occur in little over 30 % of the cases, whereas in spring with little under 30 %. The difference seems to correspond with clear sky occurrence which is higher in spring than in fall. Other than that, no markedly features are observed during the fall time.
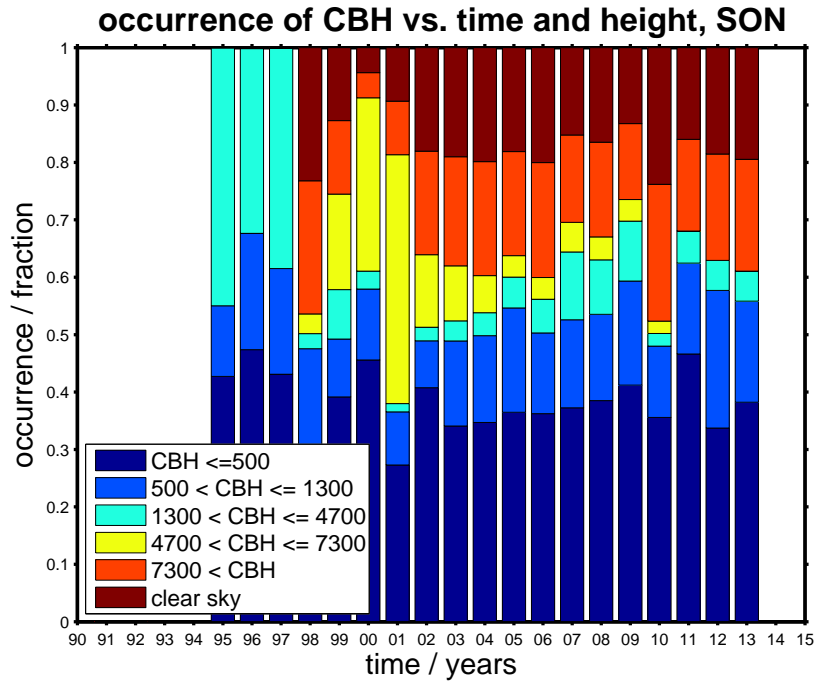
Figure 43: Seasonal vertical cloud distribution in the troposphere from ceilometer, fall (1996 to present)l.

5.3 CLOUDS AND RADIATION

During the polar night clouds play an important role in the radiation surface budget. Here low clouds have the most effect, because they radiate back at higher temperatures. Due to the rapid temperature decrease with increasing height the effect of mid and high clouds is probably weak compared to low clouds. But they will still have an impact, since during polar night all clouds will have warming effect. This suggests focusing on the occurrence of clouds at all altitudes. If one looks at the overall clouds occurrence, one could likewise investigate only clear sky counts. If the number of clear sky days in winter were to decrease, this would imply that less radiation can escape from the planet. Thus effectively warming the Arctic through less cooling.

As a first step figure 44 shows the percentage of occurrence of clear sky counts within a season for every recorded year. The plot shows that the occurrence does not change for most season. The scatter is especially large in the winter time. The summer on the other hand is the most steady season with little change. The transition month spring experience a decrease in clear sky counts, but looking at the large scatter this is probably not significant. The fall looks like spring but with smaller mean occurrence but similar scatter. A distinct feature is that in the last 5 years a high occurrence in winter also meant a high occurrence in spring. Remembering the winter humidity low in 2011 the high clear sky count during this year fits into the picture. But in total no recognizable change is seen. If only peaks or likewise dips in cloud distribution can be attributed to changes in other quantities, the increase in IWV is probably not associated with more clouds, since it shows a steady increase over the stud-
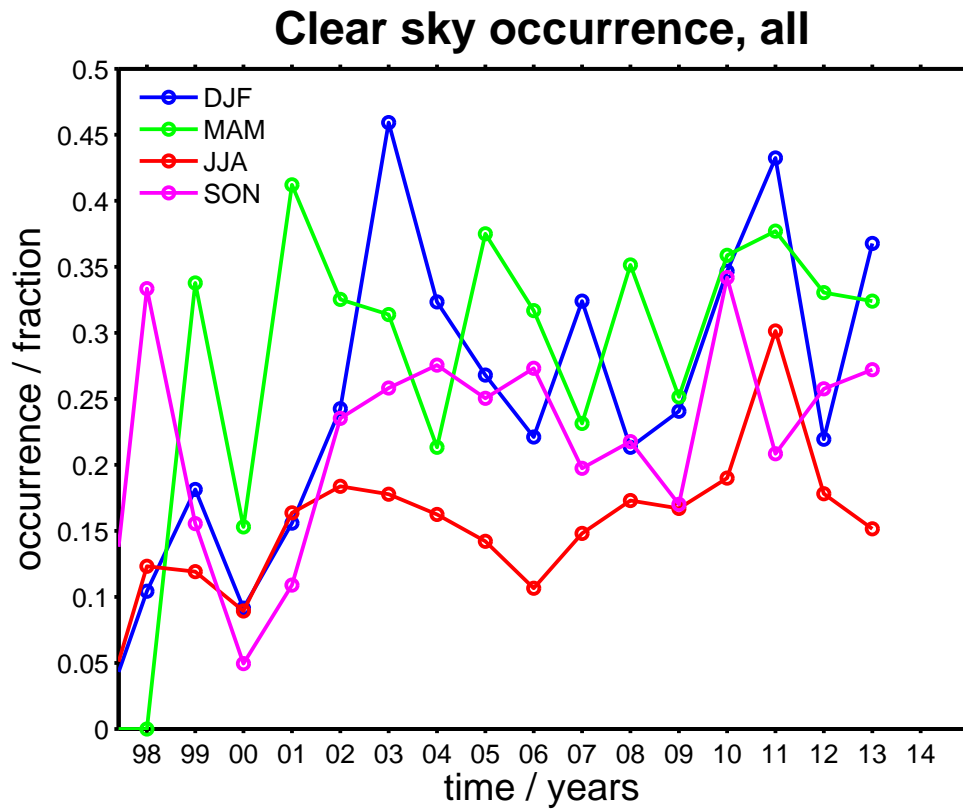
Figure 44: Seasonal occurrence of clear sky conditions.

ied period. The question remains, how the water content effects the radiation budget and also the temperature.

INFLUENCE OF WATER VAPOR ON WINTER TEMPERATURES

Picking up the idea of the previous section of investigating clear sky days is promising when dealing with the effect of water vapor on radiation flux. Water vapor is a strong green house gas, i. e. it absorbs long-wave radiation thereby reducing the outgoing long-wave radiation. The absorption takes place in several regions of the spectrum. Globally most important is the continuum absorption which increases strongly for temperatures above 320 K. This effect probably helped in the sudden onset of the runaway greenhouse on Venus [Pierrehumbert, 2010]. The other important absorption takes place in the window region of water vapor via thin absorption bands. Their absorption peaks decay exponentially with wavenumber space, i. e. changing the opacity of the atmosphere by lowering the water vapor content can have the same effect as increasing it [Pierrehumbert, 2010]. However this absorption is very ineffective for temperatures below 250 K and can therefore be neglected in the Arctic. Here the rotation band absorption becomes important, see Staley und Jurica [1970]. This effect is also sensitive to small changes in IWV. Hence this section tries to estimate the effect of clear sky conditions during winter on the radiation budget, therefor combining surface air temperature (2 m), the net long-wave radiation and the calculated IWV.

6.1 METHOD

The approach is based on a parameterization developed to estimate the long-wave cooling rate from the parameters T_{2m}, IWV and its division into height bins $iWV(h)$ under clear sky conditions according to Kondo und Matsushima [1992]. The rest of the parameterization is neglected in the method presented here. The idea is to calculate a quantity that includes cloud data, such as clear sky days, radiosonde profiles and temperature readings from the BSRN field. This quantity can than be compared to long-wave radiation data from the BSRN field. The approach given here makes only use of the radiation parameterization for the net long-wave flux. According to the above mentioned literature the following equation is based on a comparable study of radiosoundings obtained in the East of China:

$$F_{model}(r_i) = \left(F_{eq}(r_i) + 4\sigma T_s^3 (T_a(h_i) - T_s) f_{an}(r_i) \right) \cdot u_{inf}^m, \tag{32}$$

where $F_{model}(r_i)$ denotes the modeled net long-wave radiation flux with positive outgoing radiation influenced by the constituent water vapor, r_i is the water content in a slab of air with thickness δh_i located at height h_i normalized by the total water content in the integration column, namely $u_\infty^m = IWV$. F_{eq} is defined as the net flux when the ambient air temperature T_a at 1.5 m equals the surface temperature T_s. f_{an} is a non-dimensional anomaly in net flux

at normalized coordinate r_i. σ is the Stefan-Boltzmann constant. The equality flux F_{eq} and the non-dimensional anomaly f_{an} are the actual parameterization functions given via

$$F_{eq}(r_i) \quad = \sum_{j=1}^{4} a_j \cdot r_i, \tag{33}$$

$$f_{an}(r_i) \quad = b_1 r_i^{c_1} + b_2 r_i^{c_2}, \tag{34}$$

with coefficients $a_1 = 8.368$, $a_2 = 101.3$, $a_3 = -199.5$ and $a_4 = 134.5$ for the equality flux and $b_1 = 0.9447$, $c_1 = 0.3001$, $b_2 = -0.6711$ and $c_2 = 0.3512$ for the anomaly, [Kondo und Matsushima, 1992]. The ambient air temperature T_a is obtained from the radiosonde profile, the surface temperature is approximated through the 2 m-temperature T_{2m} and the normalized coordinate as well as the total water content is calculated using eq. 31. A remark is necessary that this model includes not only a dependence on water vapor content but also on temperature. Thus, the lapse rate feedback is also included.

After calculating the net flux in each height slab the net flux at the surface is obtained by numerical integration over all slabs from 10 km to the surface. The next step is validating if this simple model shows the same response to a a change in IWV under clear sky condition compared to the measured radiation budget. If this comparison is positive, it proofs at least that the Arctic winter radiation budget is sensitive to changes in IWV. A follow up study could further investigate this dependency with a full radiation model. A scheme for this method is shown in figure 45. The reason for doing this analysis with the change in net radiation flux instead of the net flux is that ΔF shows higher sensitivity to day to day changes in IWV. This is not surprising assuming that F_{net} is some arbitrary function of IWV and T. A first order Taylor-series estimate yields:

$$F(IWV, T) \approx F(IWV_0, T_0) + \frac{\partial F}{\partial IWV}(IWV_{0,T_0}) \cdot (IWV - IWV_0)$$
$$+ \frac{\partial F}{\partial T}(IWV_0, T_0) \cdot (T - T_0). \tag{35}$$
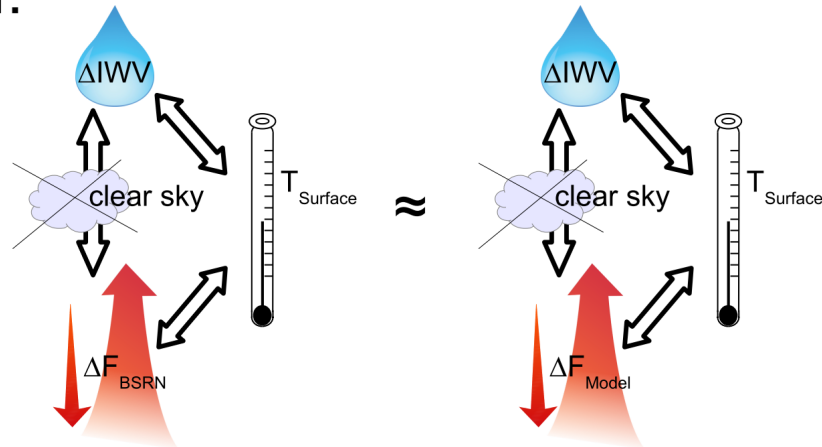
Figure 45: Schematic description of investigation method.

Replacing the values indicated by 0-index by the $i + 1$ and rearranging the above equation gives for the difference in net long-wave flux:

$$F(IWV_i, T_i) - F(IWV_{i+1}, T_{i+1}) \approx \frac{\partial F}{\partial IWV}(IWV_{i+1}, T_{i+1}) \cdot (IWV_i - IWV_{i+1}) +$$
$$+ \frac{\partial F}{\partial T}(IWV_{i+1}, T_{i+1}) \cdot (T_i - T_{i+1}). \quad (36)$$

Hence the change in net flux from one instant to another can be approximated by

$$\Delta F \approx \frac{\partial F}{\partial IWV}(IWV, T) \cdot \Delta IWV + \frac{\partial F}{\partial T}(IWV, T) \cdot \Delta T. \quad (37)$$

Using the BSRN data for calculating the change in net flux of a clear sky sounding relative to the next sounding is determined as follows

$$\Delta Fs = F - F' \quad = \left(L_\uparrow - L_\downarrow\right) - \left(L'_\uparrow - L'_\downarrow\right), \quad (38)$$

where the $'$ indicates the net flux observed for a later observation. A sounding is defined as clear sky whenever the ceilometer did not detect clouds within the first half hour after a radiosonde launch. Note that the next sounding is not necessarily a clear sky sounding. This is done, because the time differences between two clear sky soundings can be large. During this time atmospheric changes can diminish the IWV sensitivity, e.g. by front passages. By just subtracting the data of the next available day the influence of clouds and synoptic changes on integrated water vapor is assumed to be minimal.

The IWV and T dependence of equation 37 shows that the method needs additional classification of the selected clear sky days. They will be grouped in two main classes. The first makes up for the temperature dependence. Only dates with decreases in the 2 m-temperature are included, exclude rising temperatures from contributing to an increase in net radiation. The remaining day which are then subdivided in three bins according to their temperature. The first bin for very cold temperature $-20\,°C <= T < -10\,°C$, the second for intermediate temperatures $-10\,°C <= T < 0\,°C$ and the third for warm winter temperatures $0\,°C <= T$. The second main class groups the data into IWV bins by defining three sub-classes. The first for low column integrated water vapor $IWV < 3.5\,kg\,m^{-3}$, the second for medium amount $3.5\,kg\,m^{-3} < IWV < 5.5\,kg\,m^{-3}$ and last class for $IWV > 5.5\,kg\,m^{-3}$. With these two classifications it is possible to separate the influence of different temperatures and moisture contents.

6.2 COMBINED ANALYSIS OF HUMIDITY, CLOUDS AND RADIATIONS

Using the parameterization and the measured data alone the modeled daily difference for all sky conditions can be found in figure 46. As expected, ΔF_{net} is proportional to ΔIWV, the greater the decrease in water content, the greater the increase in radiation flux. This result is plausible, because the atmosphere gets thinner with smaller water content. The proportionality appears linear for small changes. The distribution of symbols underlines that for small water content (circles) the change in net flux is linear. A linear fit only for circles passing
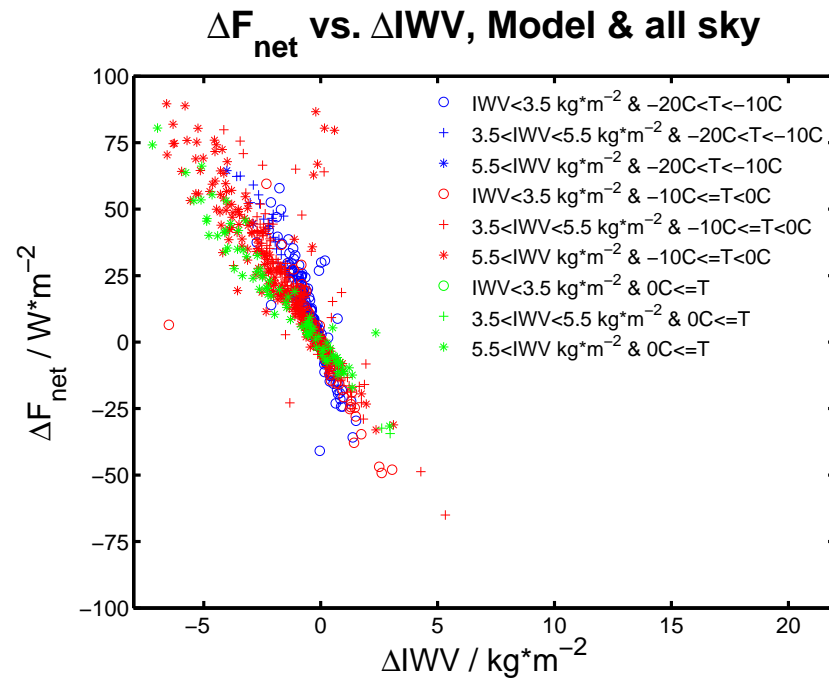
Figure 46: Daily difference in net radiation flux for all sky.

through the origin implies that the model responses to small changes especially sensitive when the ambient IWV classified as minimal, i. e. that the water content is already low in the first place. Hence, this fit presents an upper limit for net flux change. Interestingly the most sensitive response coincides with the coldest temperatures (blue).

The sensitivity decreases with increasing moisture content as indicated by the points of higher moisture content, (asterisk) and (plus) symbols and with increasing temperatures (red and green). The larger moisture values show also a larger scatter. Regarding the temperature influence, one notices that the temperatures are distributed evenly around the origin and separate markedly at ΔF_{net} around $24\,W\,m^{-2}$. The higher the temperature the more nonlinear the behavior, indicated by a large scatter. The clustering of high moisture in the nonlinear regions suggest also that at greater surface temperatures also greater moisture decreases occur. This could indicate the passage of fronts and therefore an exchange of air masses. The linear fit through this cluster region fixed to the origin represents therefore a minimum sensitivity towards changes in IWV. Figure 47 is plotted for the same data ΔIWV values but with the measured net flux. The first observation is the large scatter compared to the model. But the plot still shares the same characteristic regarding the sensitivity to small changes and the clustering of points, even though the cluster is located at approximately $20\,Wm^{-2}$ smaller values. Because the plot includes all sky conditions and the model is defined only for clear sky conditions filtering for clear sky conditions should yield a more similar picture. The clear sky model output is presented in figure 48. Here the linearity is even more pronounced, mainly through the clear separation of blue points from the rest. This is also plausible remembering the Stefan-Boltzmann law, because at very cold temperatures the same increase in outgoing radiation would require a greater warming. This makes the net
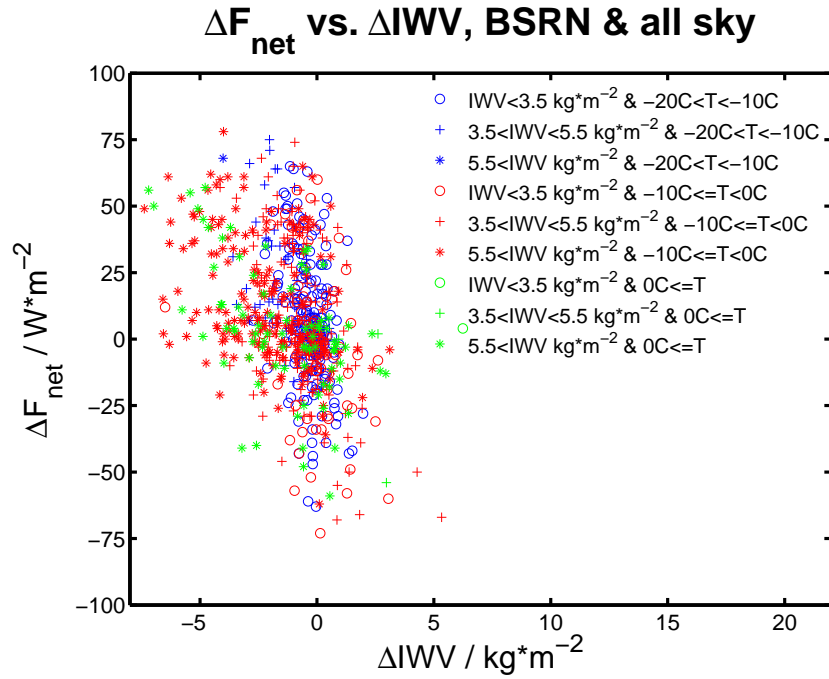
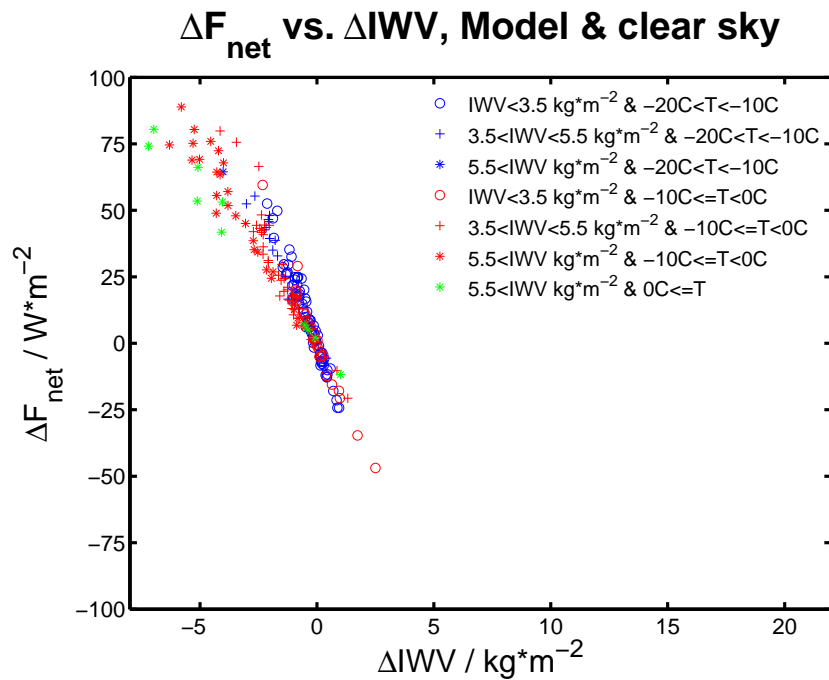Figure 47: Daily difference in net radiation flux for all sky.

Figure 48: Daily difference in net radiation flux for clear sky.

flux change more sensitive to changes in water vapor content. In other words the net flux change on temperature is weaker with decreasing temperatures. But it does not imply that the influence of water vapor should be estimated from this region, because the IWV increase is coupled to the temperature increase. Hence, interesting is the plot of clear sky BSRN measurements, figure 49. Compared to the full measured data this plot looks a lot more similar to the model, figure 48. Within the upper limit, now mostly cold (blue) and inter-
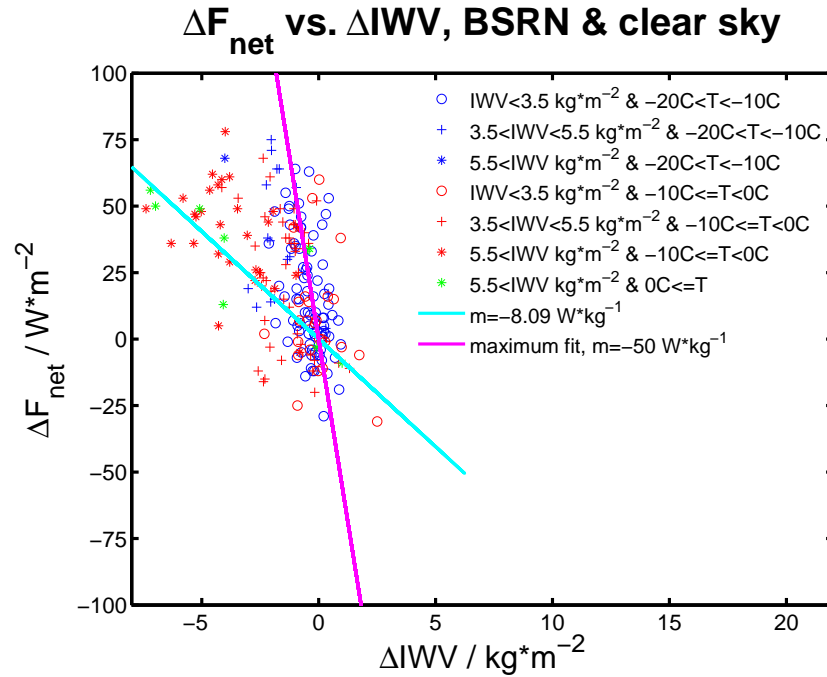
Figure 49: Daily difference in net radiation flux.

mediate (red) temperatures are found accompanied by low moisture levels and moisture changes. One could argue from this plot that the upper limit is not well suited for identifying the influence of higher IWV, because the response of ΔF_{net} to small changes in ΔIWV is dominated by small IWV (circles) . This region is better suited for identifying how the radiation budget at higher altitudes reacts, where only little water is present.

Now regarding the high IWV cluster region: In order to have the same increase in net radiation via increasing upward radiation, the influence of higher water content has to be overcome. That means the water content must decrease more. Thus requiring a bigger ΔIWV. This can be seen at the clustering of high IWV values around small ΔIWV near the origin. So the influence of high amounts of IWV on the radiation budget can be identified in the clustered (asterisk) region. Therefore this is the region of interest. It actually allows a sensitivity estimate in IWV and T. Hence, a fit (cyan) through clustered region, temperatures of $-10\,°C$ and higher, and through the origin yields a sensitivity $S_{\Delta IWV} \approx -8.09\,W\,kg^{-1}$. The fit is presented without any confidence interval, because the p-value is far to great and because it should just serve illustrative purposes. For complementary reasons the fit through the high sensitivity region is also included. This therefore gives an upper and a lower limit of the observed sensitivity towards changes in vapor content. The true sensitivity is probably somewhere in between.

In general this short analysis shows that the sensitivity of changes in net radiation flux can be analyzed with the help of the Ny-Ålesund data archive. A finer investigation could be conducted using a full radiative transfer model that can account for different weather conditions and even parameterize clouds. At a last remark comparing this result to the $3.9\,W\,m^{-2}$ increase per decade found by [Maturilli u. a., 2014] reveals a surprisingly good estimate of $3.3\,W\,m^{-2}$ per

decade, when the lower sensitivity estimated here is multiplied by the earlier stated increase in IWV of roughly $0.41\,\mathrm{kg\,m^{-2}}$.

SUMMARY AND OUTLOOK

7.1 SUMMARY

There are two separate conclusions to this study. At first the study points out that the used radiosonde record can be made sufficiently homogeneous via empirical corrections and that without the proper meta data a correction attempt should not be made. Calculating fairly RH-bias independent quantities seems here the best approach. On the contrary, the radiosonde analysis shows that trusting the radiosonde humidity at heights above 8 km is risky, because at such altitudes the sensor's functional principle reaches it limits. Hence, humidity readings from the upper troposphere and stratosphere should be excluded from future studies.

Secondly, the work presented here shows that the water content in the Arctic atmosphere has increased $0.41\,\mathrm{kg\,m^{-2}}$ per decade over time span of 24 years. This is an enormous increase of roughly 5 % of the summer maximum moisture every decade. The increase is even more pronounced during the winter time. A look at the 90th-percentile reveals that days with high column water vapor rise at an even faster pace of $1.4 \pm 2.4\,\mathrm{kg\,m^{-2}}$. Even though this increase has a great uncertainty, a sudden decrease is not expected. The uncertainty will probably become smaller as the time series continues. Further a strong correlation between anomalies in surface temperature and in water content is found for the all months except the summer months figure 2. Adding to that is the fact that clouds up to a height of 1300 m occur more often during winters with stronger warming at the surface while clear sky days occurrence did not change significantly. During spring and fall these occurrence change little over time. Note that the cloud analysis should be treated with a certain amount of distrust, because changes in the measurement instrument have altered the data record. The inhomogeneous ceilometer data is also the reason for only investigating clear sky conditions. Further the inter-comparison of a simple radiation model and the measured radiation data is used to quantify the influence of water vapor alone. This analysis shows that the long-wave depends on the change in water content, but is less sensitive for bigger than for small changes. A minimum estimate gives a sensitivity of $-8.09\,\mathrm{W\,kg^{-1}}$ for winter temperatures ranging from $-10\,°\mathrm{C}$ and rising. Given the increase in IWV per decade stated above calculating the estimate influence of water vapor on the net radiation flux results in a decrease of $-3.3\,\mathrm{W\,m^{-2}}$ per decade. Note that the model defines outgoing radiation as positive this really means an increase in net radiation flux at the surface. This number is surprisingly close to the increase of $3.9\,\mathrm{W\,m^{-2}}$ found by [Maturilli u. a., 2014] given the fact that the previous analysis was done with only a parameterization which was not developed for the Arctic. But it should be pointed out that the estimation made here would not withstand a significance test due to the poor fit. Also, the estimate does not show that the increase in radiation can be attributed to water vapor alone. It merely points

out, that water vapor increase is likely to add to the already present increase in temperature and radiation.

7.2   OUTLOOK

For the future this thesis points out several fields that could be investigated further. Starting with the radiosoundings first. Because of the known disabilities of capacitance sensors for measuring low RH values under cold conditions comparing the current radiosonde to one that uses a hydrophilic polymer base should be interesting. Such a polymer should perform better under said conditions, because it is more sensitive to low RH values. Currently such a comparison is done occasionally with frost-point hygrometers. This method is the most exact for measuring humidity but also a very tedious one. A second type of radiosondes that performs better under cold conditions and is launched more often than the frost-point hygrometer could introduce new inside in processes concerning the upper troposphere and the stratosphere especially in the winter period.

Regarding clouds, a closer look into the ceilometer data could be done, performing a similar study as presented in the previous chapter but for different cloud base height. Through this one could gain more inside in the effect of clouds on the radiation budget. The ceilometer could also help in reconstructing the past vertical cloud distribution. Imagine a study that uses the present ceilometer, which is able to resolve several cloud base heights and their corresponding thickness, whenever the clouds are not too thick. Together with the simultaneous radiosonde humidity and temperature record it should be possible to construct a working cloud detection algorithm by comparing the two. This algorithm could than be used to infer past cloud distributions with the help of the corrected humidity data.

Regrading the water content and its influence on the radiation budget, one should be careful in making assumptions for the entire Arctic on the basis of data recorded at only a few sites. In the case of Ny-Ålesund the orography could substantially influence the radiation readings through the creation of clouds around the mountains and in the fjord valley. One could therefore suggests a research project with the IASOA-radiation working group which has the goal of characterizing different measurement site in order to identify common influences that are present throughout the Arctic.

At last the study method described in the previous chapter should be conducted with a full radiation model in order to have a better estimate of the the sensitivity. With the knowledge of the local characteristics one can hope to exclude their influence and give an estimate that holds for a larger part of the Arctic. Maybe such an estimate can be used to improve parameterization and thus improve the climate models.

APPENDIX

A.1 HUMIDITY CORRECTION TABLES

k_0	k_1	k_2	p_0	p_1	p_2	p
0.066704	0.39114	-0.04026	0.6678	0.0854	0.0004	-1.0013×10^{-5}

Table 3: Table to correct contamination bias [Wang u. a., 2009].

H_0	H_1	H_2	H_3	H_4
0.0143	-0.3677	0.019	-0.00029791	num1.4298e − 6

Table 4: Constants required for temepature dependent correction, RH sensitive part [Wang u. a., 2009].

T_0	T_1	T_2	T_3	T_4	T_5
0.3475	0.0283	4.2090×10^{-4}	-1.4894×10^{-4}	6.4325×10^{-7}	2.1677×10^{-8}

Table 5: Constants required for humidity correction [Wang u. a., 2009].

R_0	R_1	R_2
-446.5	122.83	-8.489

Table 6: Correction coefficients of radiation dry bias for the earlier RS90/92 generation according to [Kivi u. a., 2009].
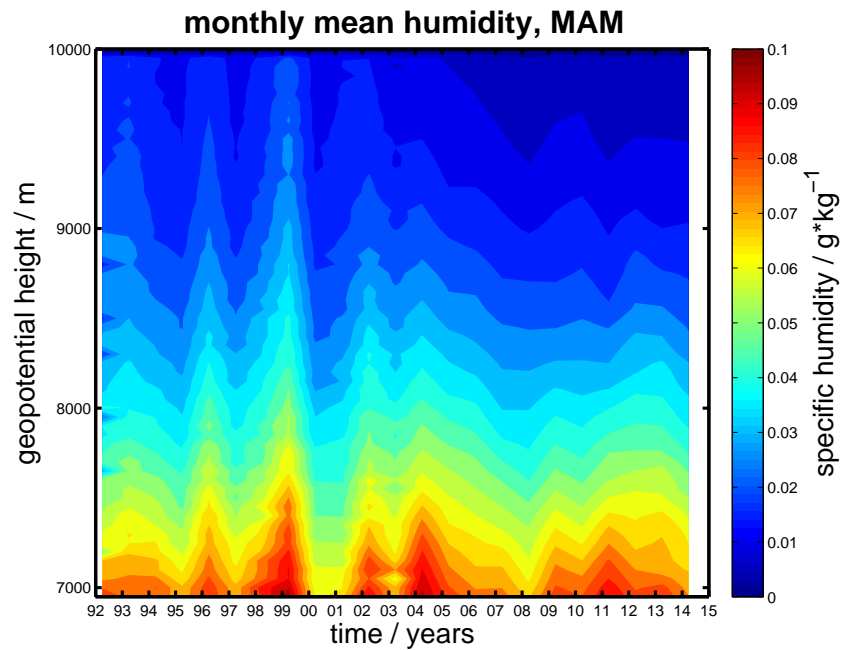
R_0	R_1	R_2
-144.5	30.18	-1.367

Table 7: Correction coefficients of radiation dry bias for the later RS90/92 generation according to [Kivi u. a., 2009].

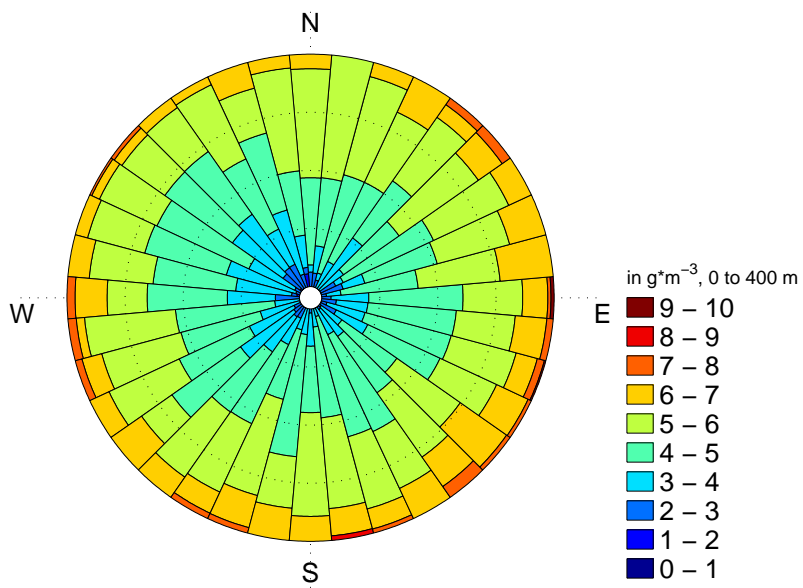A.2   ADDITIONAL PLOTS

A.2.1   *Additional humidity contours*

Monthly mean of corrected RH
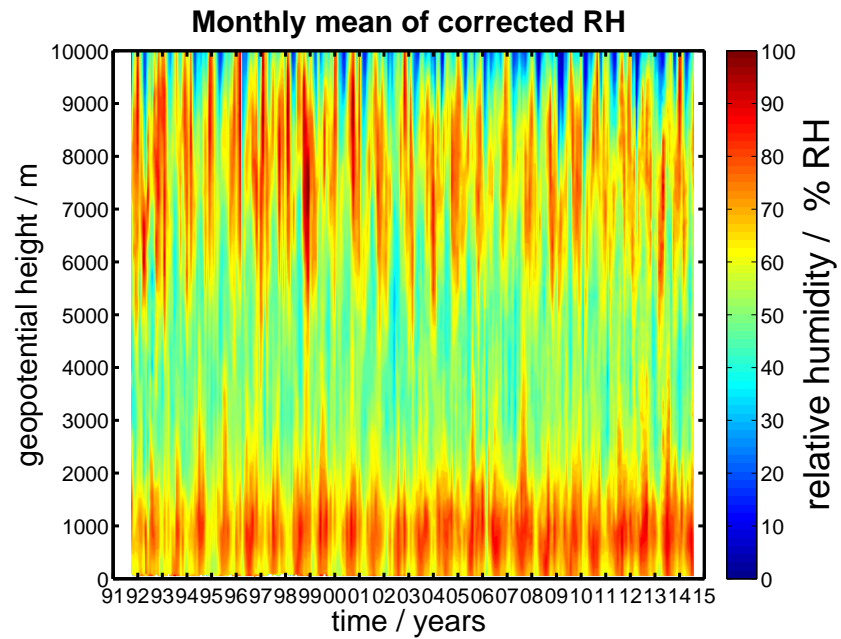
(a) RH merged for all seasons.
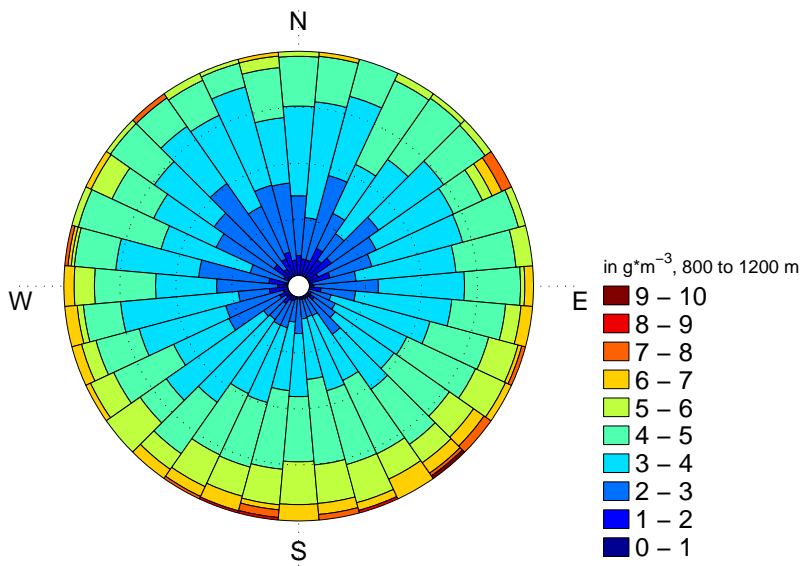
monthly mean humidity, MAM

(b) Monthly mean specific humidity in the upper troposphere.

Figure 50: Additional humidity contours for spring and year round (1991 to present).
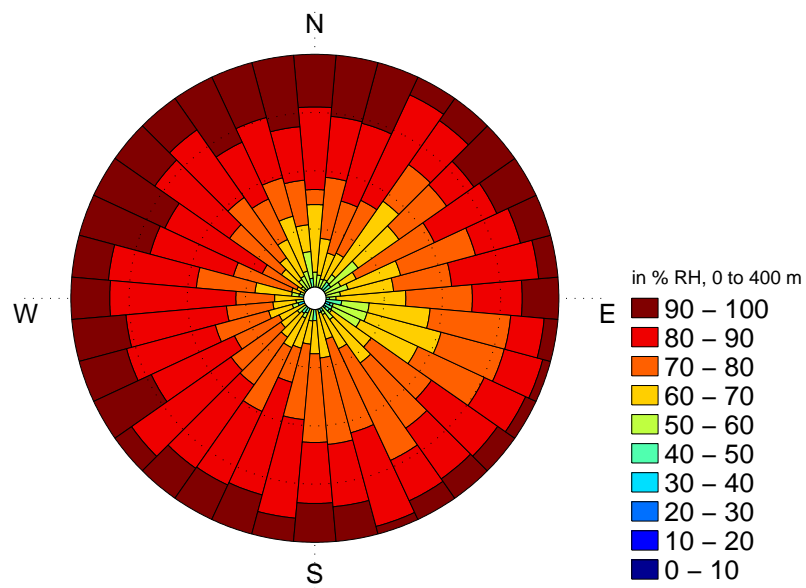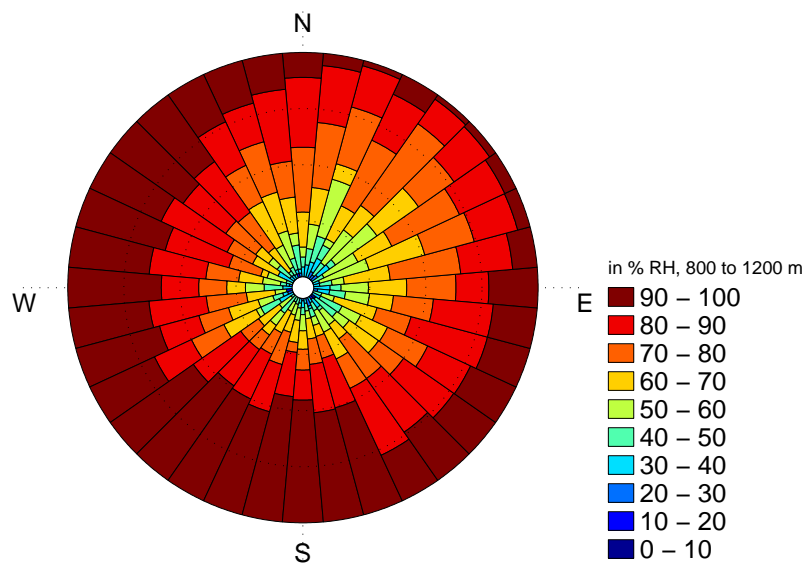
A.2.2 *Orographic characteristics*

(a) 0 m, 400 m.

(b) 800 m to 1200 m.

Figure 51: Absolute humidity rose for summer (1991 to present).

A.2.3   *Fits of 90th-percentile*

(a) 0 m, 400 m.

(b) 800 m to 1200 m.

Figure 52: Relative humidity roses for summer (1991 to present).
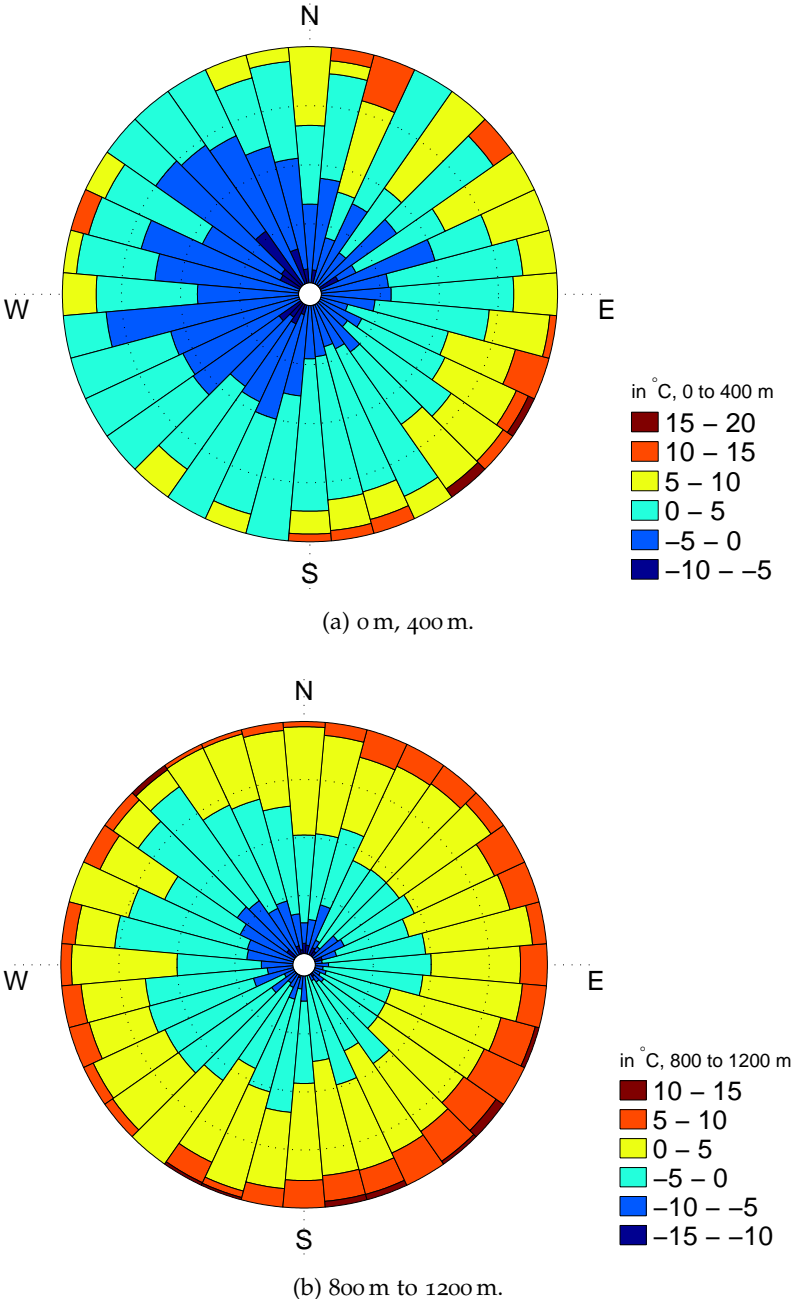
A.2.4 *Vertical cloud distribution*

(a) 0 m, 400 m.

(b) 800 m to 1200 m.

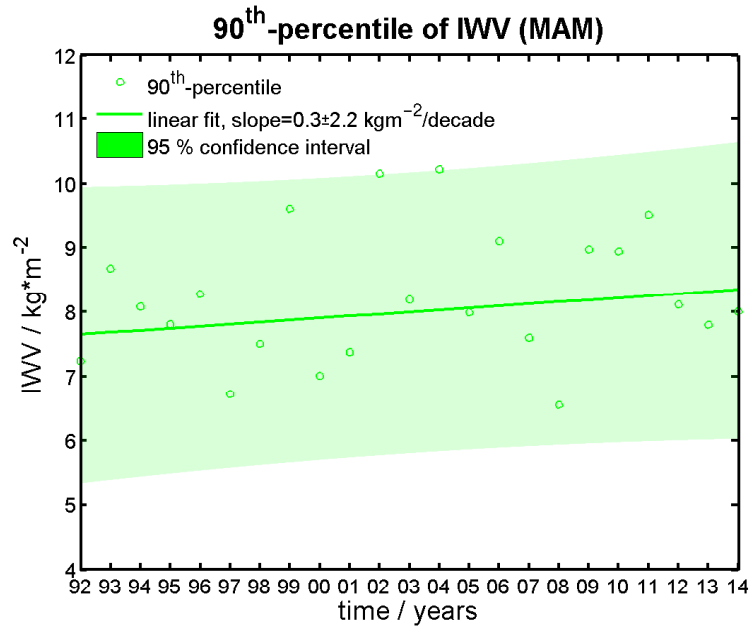Figure 53: Temperature roses for summer (1991 to present).

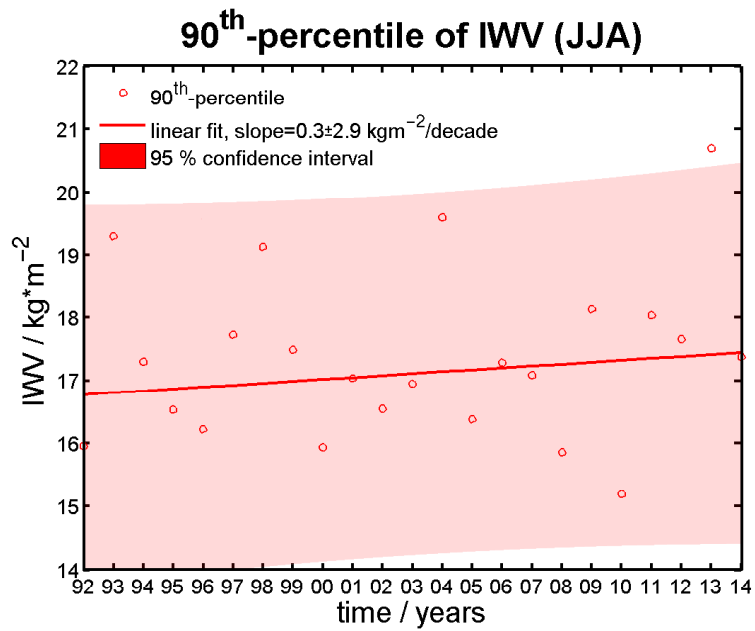Figure 54: Fit for 90th-percentile, spring (1991 to present).

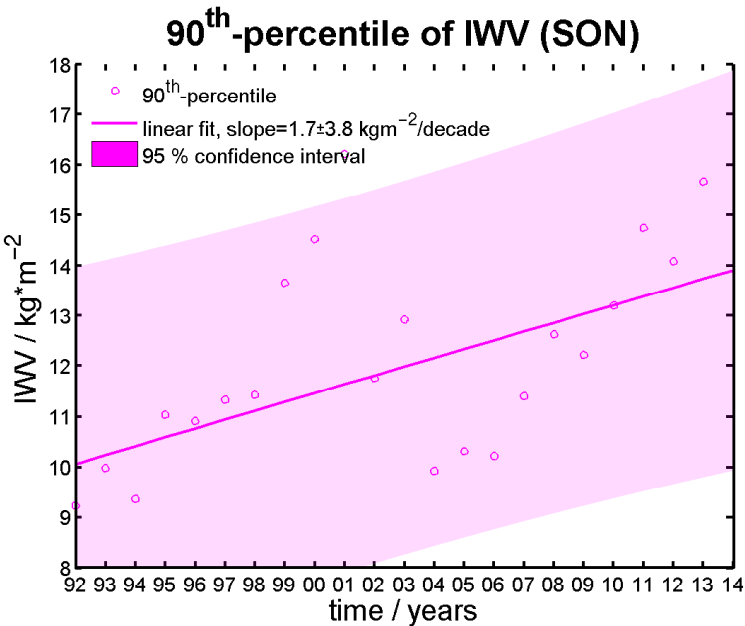Figure 55: Fit for 90th-percentile, summer (1991 to present).

Figure 56: Fit for 90th-percentile, fall (1991 to present).
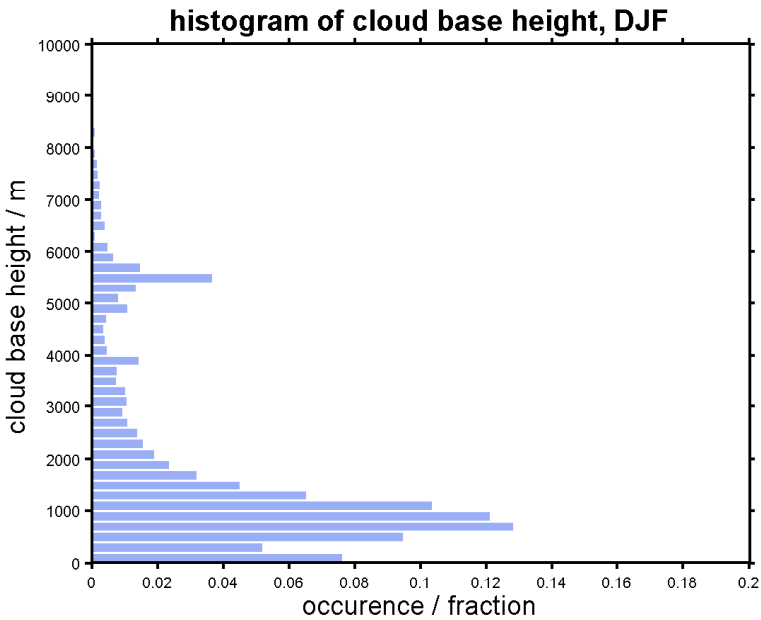

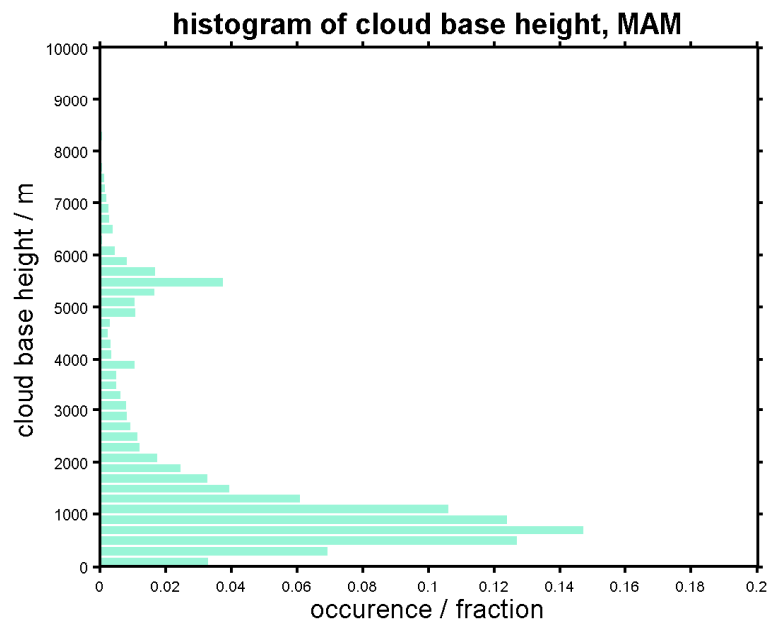Figure 57: Vertical cloud distribution derived from ceilometer counts, winter (1994 to present).

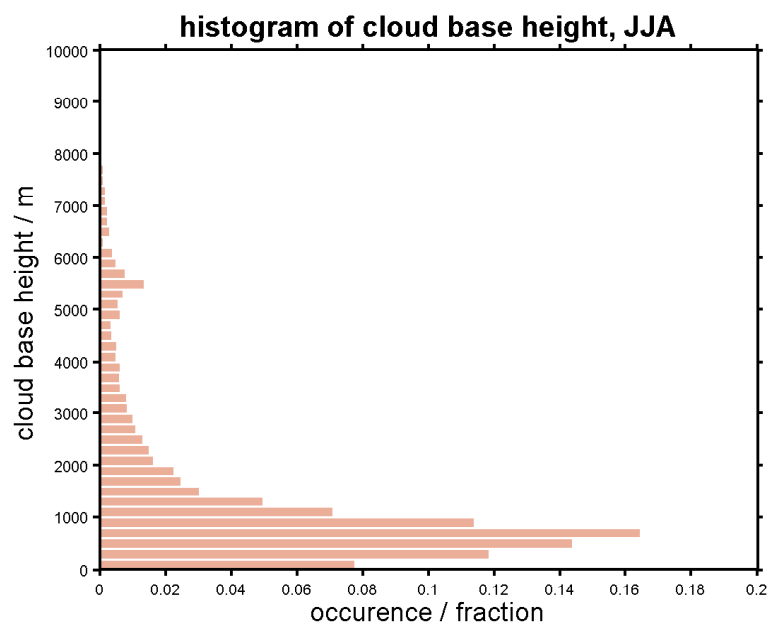Figure 58: Vertical cloud distribution derived from ceilometer counts, spring (1994 to present).

Figure 59: Vertical cloud distribution derived from ceilometer counts, summer (1994 to present).
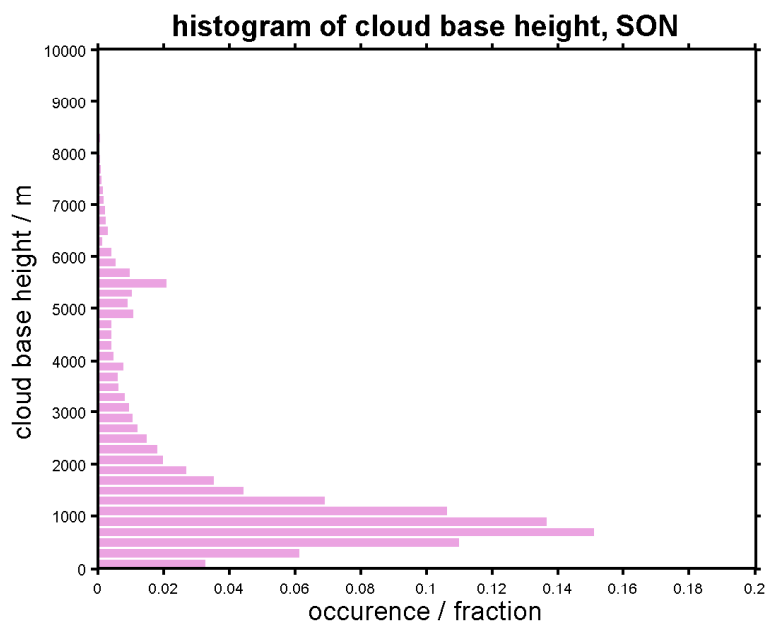
Figure 60: Vertical cloud distribution derived from ceilometer counts, fall (1994 to present).

[Anderson 1995]   ANDERSON, P. S.: Mechanism for the behaviour of hydroactive materials used in humidity sensors. In: *Journal of atmospheric and oceanic technology* 12 (1995), Nr. 3, S. 662–667. – ISSN 0739-0572

[Chen und Lu 2005]   CHEN, Zhi ; LU, Chi: Humidity Sensors: A Review of Materials and Mechanisms. In: *Sensor Letters* 3 (2005), Nr. 4, S. 274–295. – URL http://www.ingentaconnect.com/content/asp/senlet/2005/00000003/00000004/art00002

[Curry u. a. 1995]   CURRY, J. A. ; SCHRAMM, J. L. ; SERREZE, M. C. ; EBERT, E. E.: Water vapor feedback over the Arctic Ocean. In: *Journal of Geophysical Research: Atmospheres* 100 (1995), Nr. D7, S. 14223–14229. – URL http://dx.doi.org/10.1029/95JD00824. – ISSN 2156-2202

[Friedman 1984]   FRIEDMAN, J. H.: A Variable Span Smoother / Laboratory for Computational Statistics, Dept. of Statistics, Stanford. 1984 (5). – Tech. Rep. No.

[Geiger 1954]   GEIGER, R.: *Klassifikation der Klimate nach W. Köppen.* 1954. – URL http://link.springer.com/article/10.1007/BF00708964

[Hansen u. a. 2010]   HANSEN, J. ; RUEDY, R. ; SATO, M. ; LO, K.: GLOBAL SURFACE TEMPERATURE CHANGE. In: *Reviews of Geophysics* 48 (2010), Nr. 4, S. n/a–n/a. – URL http://dx.doi.org/10.1029/2010RG000345. – ISSN 1944-9208

[Hyland und Wexler 1983]   HYLAND, R. W. ; WEXLER, A.: Formulations for the thermodynamic properties of the saturated phases of H2O from 173.15 K to 473.15 K. In: *American Society of Heating, Refrigerating and Air-conditioning Engineers* 89 (1983), Nr. 4, S. 500–519. – URL http://www.ingentaconnect.com/content/asp/senlet/2005/00000003/00000004/art00002

[Kivi u. a. 2009]   KIVI, R. ; KUJANPÄÄ, J. ; AULAMO, O. ; HEIKKINEN, P. ; HASSINEN, S. ; CALBET, X. ; MONTAGNER, F. ; VÖMEL, H.: Observations of water vapor profiles over Northern Finland by satellite and balloon borne instruments. In: *EUMETSAT Meteorological Satellite Conference*, 2009

[Kondo und Matsushima 1992]   KONDO, J. ; MATSUSHIMA, D.: *A simple parameterization of longwave radiative cooling with application to the atmospheric boundary layer for clear sky conditions.* 1992. – URL http://link.springer.com/article/10.1007/BF00708964

[Kupfer u. a. 2006]   KUPFER, H. ; HERBER, A. ; KÖNIG-LANGLO, G.: *Radiation Measurements and Synoptic Observations at Ny-Ålesund, Svalbard.* Alfred-Wegener-Institut für Polar- und Meeresforschung, 2006 (Berichte zur Polar- und Meeresforschung). – URL http://books.google.de/books?id=8Ck1kgAACAAJ

[Liu u. a. 2000]   LIU, Y. ; CHEN, Y. ; BAKI, H.: Precision of precipitable water vapor from radiosonde data for GPS solutions. In: *Geomatica* 54 (2000), Nr. 2, S. 171–175

[Maturilli u. a. 2014]   MATURILLI, Marion ; HERBER, Andreas ; KÖNIG-LANGLO, Gert: Surface radiation climatology for Ny-Ålesund, Svalbard (78.9° N), basic observations for trend detection. In: *Theoretical and Applied Climatology* (2014), May. – URL http://link.springer.com/article/10.1007%2Fs00704-014-1173-4

[Miloshevich u. a. 2004]   MILOSHEVICH, L.M. ; PAUKKUNEN, A. ; VÖMEL, H. ; OLTMANS, S. J.: Development and validation of a time-lag correction for Vaisala radiosonde humidity measurements. In: *J. Atmos. Oceanic Technol.* (2004), Nr. 21, S. 1305–1327

[Pierrehumbert 2010]   PIERREHUMBERT, Raymond T.: *Principles of Planetary Climate*. Cambridge University Press, 2010. – URL http://dx.doi.org/10.1017/CBO9780511780783. – Cambridge Books Online. – ISBN 9780511780783

[data continuity section]

[Staley und Jurica 1970]   STALEY, D. O. ; JURICA, G. M.: Flux Emissivity Tables for Water Vapor, Carbon Dioxide and Ozone. In: *Journal of Applied Meteorology* 9 (1970), Nr. 3, S. 365–372. – URL http://dx.doi.org/10.1175/1520-0450(1970)009<0365:FETFWV>2.0.CO;2

[Stocker u. a. 2013]   STOCKER, Thomas F. ; DAHE, Q ; PLATTNER, Gian-Kasper: Climate Change 2013: The Physical Science Basis. 2013. – Forschungsbericht

[Stormbom und Lyyra 1995]   STORMBOM, L. ; LYYRA, M.: *Sensing humidity and prediction of icing*. UK Patent GB 2323928 A. March 1995

[Treffeisen u. a. 2007]   TREFFEISEN, R. ; KREJCI, R. ; STRÖM, J. ; ENGVALL, A. C. ; HERBER, A. ; THOMASON, L.: Humidity observations in the Arctic troposphere over Ny-Ålesund, Svalbard based on 15 years of radiosonde data. In: *Atmos. Chem. Phys., 7(10). {www.atmos-chem-phys.net/7/2721/2007/}* 2721 (2007)

[Vaisala a]   VAISALA: *Technical information: RS80 radiosonde*. Ref. A571en 1997-08. – URL http://www.vaisala.com

[Vaisala b]   VAISALA: *Technical information: RS92-SGP radiosonde*. Ref. B210358en-f. – URL http://www.vaisala.com

[Wang u. a. 2009]   WANG, J. ; COLE, H. ; CARLSON, D. J. ; MILLER, E. R. ; BEIERLE, K. ; PAUKKUNNEN, A. ; LAINE, T. K.: Corrections of humidity measurement errors from the Vaisala RS80 radiosonde – Applications to TOGA COARE data. In: *J. Atmos. Oceanic Technol.* (2009), Nr. 19, S. 981–1002

[WMO 2000]   WMO: General meteorological standards and recommended practices. 2000 (49). – Forschungsbericht. Appendix A, WMO Technical Regulations

DECLARATION

Der Verfasser erklärt an Eides statt, dass er die vorliegende Arbeit selbstädig, ohne fremde Hilfe und ohne Benutzung anderer als die angegebenen Hilfmittel angefertigt hat. Die aus fremdem Quellen (einschliešlich elektronischer Quellen) direkt oder indirekt übernommen Gedanken sind ausnahmslos als solche kenntlich gemacht. Die Arbeit ist in gleicher oder ähnlicher Form oder auszugsweise im Rahmen anderer Prüfungen nocht nicht vorgelegt worden.

Potsdam, September 30, 2014

_____

Markus Kayser,